Azimuthal Correlation and Conditional Yield Measurements at $\sqrt{s_{NN}}$=200GeV in Au+Au, d+Au and p+p Collisions at RHIC

A Dissertation Presented

by

Anne Marie Sickles

to

The Graduate School

in Partial Fulfillment of the

Requirements

for the Degree of

Doctor of Philosophy

in

Physics

Stony Brook University

December 2005

Stony Brook University

The Graduate School

Anne Marie Sickles

We, the dissertation committee for the above candidate for the Doctor of Philosophy degree, hereby recommend acceptance of this dissertation.

Barbara Jacak
Relativistic Heavy Ion Group, Stony Brook University
Dissertation Director

George Sterman
C.N. Yang Institute for Theoretical Physics, Stony Brook University
Chairman of Dissertation

Abhay Deshpande
Department of Physics, Stony Brook University

David Morrison
Department of Physics, Brookhaven National Laboratory
Outside Member

This dissertation is accepted by the Graduate School.

Dean of the Graduate School

Abstract of the Dissertation

Azimuthal Correlation and Conditional Yield Measurements at $\sqrt{s_{NN}}$=200GeV in Au+Au, d+Au and p+p Collisions at RHIC

by

Anne Marie Sickles

Doctor of Philosophy

in

Physics

Stony Brook University

2005

Advisor: Barbara Jacak

One of the most interesting results from the first year of Relativistic Heavy Ion Collider (RHIC) running was the increase in the ratio of protons and anti-proton to pions at intermediate p_T ($2< p_T <4.0\text{GeV}/c$) by a factor of ≈ 3 from p+p collisions to central Au+Au collisions. There has been much interest in determining whether the source of these extra protons and anti-protons was primarily due to jets, a collection of correlated particles re-

sulting from large momentum transfer parton collisions, or soft, low momentum transfer, particle production. Soft production scenarios that could explain the baryon excess include recombination models which predict intermediate p_T particle production to be dominated by hadrons formed by low p_T quarks recombining into final state hadrons due to the high phase space density in head on Au+Au collisions.

Yields of hadrons associated with intermediate p_T trigger hadrons measured in 200 GeV Au+Au, d+Au and p+p collisions at midrapidity as a function of the trigger and associated hadron species, associated hadron p_T and centrality in Au+Au collisions are studied in the PHENIX Experiment at RHIC.

Associated yield for the near side is independent of trigger hadron type except for the most central Au+Au collisions. Associated yields for trigger mesons are higher in Au+Au than in d+Au and p+p. Identified associated means exhibit the same trend as when the associated particle is not identified. Identified associated baryons show no dependence on trigger type or centrality. Associated yields for proton triggers with anti-proton partners are in agreement with yields for anti-proton triggers and proton partners and the associated yield for proton triggers with proton partners and anti-proton triggers and anti-proton partners are both consistent with zero. There is no trigger particle dependence on the away side.

These results are inconsistent with a soft baryon source. The increase in the near side associated yields from p+p to Au+Au collisions suggests the medium created in Au+Au collisions modifies the jets strongly as they pass through the medium. Further study is necessary to understand why the associated yields are modified and the interaction with the medium results in baryon rich jets at intermediate p_T .

Dedication

AMDG

Contents

List of Figures

List of Tables

Acknowledgements

First, I would like to thank my advisor, Barbara Jacak for her advise, encouragement and friendship over the last four years. Barbara has always encouraged me to do better and to always concentrate on the physics. I have benefitted from her creativity, enthusiasm and amazing energy.

I would also like to thank all my other Stony Brook and PHENIX collaborators for their excellent ideas, discussions and help. I would like to thank Tom Hemmick, Ralf Averbeck and Axel Drees for help and insight. In particular, I would also like to thank my fellow Stony Brook graduate students, past and present especially Matt Nguyen, Felix Matathias, Jiangyong Jia, Sean Leckey, Sarah Campbell, Torsten Dahms and Mike McCumber. I thank Mike Reuter for his help in getting this analysis started. I would also like to thank the members of the PHENIX Hard Scattering working group for their good ideas in the development of this analysis especially Mike Tannenbaum, Nathan Grau, Jamie Nagle and Paul Stankus.

I would also like to thank my thesis committee for their many helpful comments.

Lastly, I would like to thank my husband Alex Withers for all the extra work he did keeping our lives together while I was working on this. I would

also like to thank Sylvia for being such a wonderful baby, enabling me to get this written.

Chapter 1

Introduction

1.1 Quark Gluon Plasma and RHIC

The goal of the Relativistic Heavy Ion Collider (RHIC) at Brookhaven National Laboratory is to recreate a phase of matter not seen since a few micro-seconds after the Big Bang. At this time the the temperature of the universe was so large that quarks and gluons were not bound inside nucleons (protons and neutrons), but existed as a quark-gluon plasma (QGP). As the universe cooled quarks and gluons became confined in nucleons by the strong force. As the universe cooled further, atomic matter, which dominates the visible universe today, formed.

The strong force, in contrast to the electromagnetic and gravitational forces which decrease as the inverse square of the distance between the particles, gets stronger as the distance between the particles increases. Because of this, bare quarks and gluons (collectively, partons) are not observed in nature today. As the distance between two strongly interacting particles grows, more energy is

required to further separate them. Eventually, the potential energy between the quarks or gluons becomes great enough to create a new quark-anti-quark out of the vacuum, preventing bare partons from existing in normal conditions. Attempts to create the QGP at RHIC involve raising the temperature beyond that at which normal nuclear matter can exist.

At RHIC two counter circulating beams of gold nuclei are collided into each other with a center of mass energy of $\sqrt{s_{NN}}$ =200GeV. At this high energy the partons from the two nuclei interact as the nuclei pass through each other. A fireball is created with a large temperature and energy density. Due to high collision rates of partons within the fireball, the created system is expected to be quickly thermalized, ≈2 fm/c, with a high temperature, approximately 175MeV (≈2 trillion degrees Kelvin). At these high temperatures the long distance behavior of the strong force is predicted to be greatly weakened [1].

The initial energy density of the collision region can be estimated by the Bjorken energy density [2], ϵ_{Bj},

$$\epsilon_{Bj} = \frac{1}{\tau_{form}} \frac{dE_T(\tau_{form})}{dy} \tag{1.1}$$

where τ_{form} is a proper time after which the produced particles can be considered formed. A realistic value of τ_{form} is 0.35 fm/c [3], which is greater than the crossing time of the nuclei through each other $2R/\gamma$ (about 0.13 fm/c for Au nuclei at $\sqrt{s_{NN}}$=200GeV). $\frac{dE_T}{dy}$ is the transverse energy per unit rapidity (rapidity is defined in Section 1.3). PHENIX has measured $\frac{dE_T}{d\eta}$=600GeV [4] (in the limit where the particle masses are small $\eta = y$). This leads to an energy density of 15 GeV/fm^3.

The hot dense matter created in the collisions does not last long enough to be directly measured. The lifetime of the system is on the order of 10fm/c; even with most of the particles leaving the collision region at nearly the speed of light, the spatial extent of the system is on the order of 10^{-14}m. The properties of the system must be inferred from the remnants of the collision which reach detectors a few meters away from the collision region. The non-interacting pieces of the Au nuclei continue forward in the beam direction after the collision, but in the collision region energy is scattered perpendicular to the beam direction. These particles which are the remains of inelastic parton and nucleon scattering of the collision are what is of interest to us in the present analysis. Properties of the medium can be measured from the interactions between the particles as they leave the interaction region.

The collisions are measured by four detectors constructed around the ring: PHENIX, STAR, BRAHMS, and PHOBOS. PHENIX and STAR are large detectors designed to measure as much about the collisions as possible. BRAHMS is a small acceptance detector designed to measure particles as a function of the scattering angle with respect to the initial beam direction and PHOBOS is a small detector with large acceptance designed to count the charged particle multiplicity. The data presented here were measured with the PHENIX detector.

1.2 Control Systems: d+Au and p+p Collisions

Due to the complexity of Au+Au collisions (in a head on collision a few thousand particles are created) it is necessary to compare the measurements with simpler systems. At RHIC collisions between two protons (p+p collisions) and between a deuteron and a gold nucleus (d+Au collisions) at the same energy per nucleon are also measured. Both collisions do not create the large hot medium expected in Au+Au collisions, but there should still be many similarities in the pre- and post- collision times. As the QGP expands and cools the phase space density decreases thus the formation processes for the final observed hadrons should be similar in all three collision systems. d+Au collisions also provide information about nuclear effects coming from the initial state of the large nuclei. Without this control system it would be harder to determine whether changes in the final state of Au+Au collisions were due to the medium produced by the collision or to conditions in the initial nuclei. Deuterons are used instead of protons in the asymmetric collisions because of the charge to mass ratio is of the deuteron is closer to that of gold; no significant nuclear effects are expected from the addition of a single neutron.

1.3 Definitions and Kinematic Quantities

Here we define some quantities which will be used throughout this work.

Center of Mass Energy The center of mass energy is expressed via the Lorentz scalar s. The collision energy per nucleon pair is $\sqrt{s_{NN}}$. The collisions studied here all have $\sqrt{s_{NN}}$ =200GeV; each beam momentum is 100GeV/nucleon: 100GeV for proton beams, 200GeV for deuteron beams and 19.7TeV for Au beams.

Momentum and Energy In this analysis particles are primarily classified according to their transverse momentum, p_T which is the projection of the particle's 3-momentum onto the plane perpendicular to the beam axis

$$p_T = |p| \sin\theta \tag{1.2}$$

where θ is the angle of the particle's direction with respect to the beam axis. Rapidity, y, is related to the particle's momentum along the beam axis:

$$y = \frac{1}{2} \log \frac{E + p_z}{E - p_z}$$

where E is the particle's energy and p_z is the particle's momentum along the beam axis. Pseudo-rapidity η is also useful as a measure of the particle's angle with respect to the beam axis:

$$\eta = -\log \tan \frac{\theta}{2}$$

In the limit of massless particles $y = \eta$.

Scattering Each parton carries a fraction x of its parent nucleon's total initial momentum. Parton-parton scattering is characterized by the momentum transfer between the partons the square of the momentum transfer, Q^2.

1.3.1 Centrality

The nucleon distribution inside nuclei can be described by the Woods-Saxon density profile:

$$\rho(r) = \frac{\rho_0}{1 + e^{\frac{r-R}{a}}}$$

with

$$R = (1.12A^{1/3} - 0.86A^{-1/3})fm \quad (1.3)$$

$$\rho_0 = 0.169fm^3 \quad (1.4)$$

$$a = 0.54fm \quad (1.5)$$

$\rho(r)$ is the density of nucleons per cubic fm as a function of the distance from the nuclear center, which is shown in Figure 1.1 for Au nuclei. The radius of a Au nuclei (Equation 1.4 is approximately $6.4fm$. The impact parameter for a Au+Au collision can be greater than $15fm$ (as seen in Figure 1.1 there is a non-zero nucleon density for radii up to approximately $8fm$).

Glauber Model The Glauber model [5] is a geometrical model that uses information about the size and shape of the nuclei to model the number of nucleons involved in the collision, participating nucleons, and the number of binary nucleon-nucleon collisions which occur. The collision is modeled in

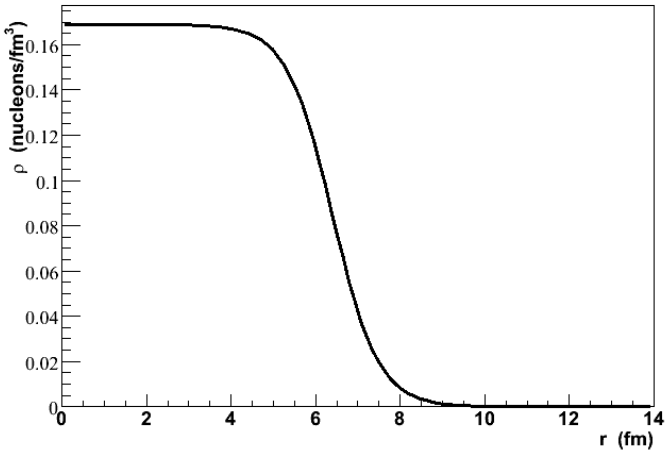

Figure 1.1: Wood-Saxon density distribution as a function of the distance from the nuclear center for a Au nuclei using the parameters described in the text.

terms of nucleons. The nucleon-nucleon cross section is assumed to stay constant and the nucleon trajectory remains a straight line for all binary collisions an individual nucleon undergoes. The PHENIX Glauber calculation uses a nucleon-nucleon cross section, σ of 42mb. A collision is said to occur if

$$b < \sqrt{\frac{\sigma}{\pi}}. \tag{1.6}$$

There are equations for the various parameters in the Glauber model, but PHENIX uses a Monte Carlo in order to map the Glauber parameters to experimental observables [6]. Experimentally, the number of collision participants can be measured from the spectator nucleons (those nucleons from the Au nucleus which do not interact) measured downstream from the collision region. The number of binary collisions is not a directly measurable quantity and must rely on models about how the nucleons interact with each other.

Centrality is a measure of the percentage of the total cross section with

a smaller impact parameter; a collision with 5% centrality has an impact parameter such that 95% of collisions have a larger impact parameter. Impact parameter cannot be directly measured, but there are many methods to infer the impact parameter from the remains of the nuclei. Two other commonly used parameters related to the collision centrality are the number of binary collisions, N_{coll}, and the number of participating nucleons, N_{part}. The number of binary collisions is the number of collisions between pairs of nucleons in the initial stages of the collisions. If there are no nuclear effects and heavy ion collisions are just a collection of independent nucleon-nucleon collisions than particle yields should be the p+p values scaled by N_{coll}. Deviations from this scaling are a measure of the medium effects. The number of participating nucleons is just the number of nucleons that interacted in the collision. For large impact parameters this number is small and for small impact parameters this number approaches 394, the total number of nucleons in the two Au nuclei. The details of the PHENIX centrality measurement will be discussed in Section 2.2.3.

1.4 Hard Scattering as a Probe of the QGP

Quantum Chromodynamics Quantum chromodynamics (QCD) is the theoretical description of the strong force–the force between particles carrying color charge. Quarks carry color and electric charge and gluons, the strong force mediators, also carry color charge. QCD also has the property of asymptotic freedom [7] where the strength of the interaction between colored particles is small when the particles are close together and grows as the particles move

apart. One important consequence of this is *confinement*, colored objects are not observed in normal situations. As two colored objects are moved apart in vacuum the energy required to further separate them increases until it is energetically favorable to produce a quark-anti-quark ($q\bar{q}$) pair between the quarks that were being separated.

One way to probe the created medium in heavy ion collisions is through a study of hard scattering, the scattering of two partons with large momentum transfer, Q^2. Hard scattering processes are a powerful tool for studying the medium in Au+Au collisions because unlike small Q^2 processes, hard scattering cross sections are directly calculable in perturbative QCD (pQCD); because of the small length scale the coupling is small. Figure 1.2 shows the jet cross sections from five experiments at five collision energies compared to a next to leading order (NLO) pQCD calculation. Good agreement is observed between the theory and the data.

Fragmentation The outgoing partons *fragment* into the final state hadrons, collectively *jets*, as they leave the collision region. Fragmentation is the non-perturbative process by which single partons become hadrons. The outgoing scattered parton radiates gluons which split into $q\bar{q}$ pairs. These quarks and anti-quarks become the observed jet hadrons. Fragmentation is non-perturbative because the hadronization process for the quarks and anti-quarks involves low momentum scales and the coupling is strong.

Since fragmentation is non-perturbative it is not possible to calculate fragmentation functions from pQCD. Instead they are measured from the jet particle distributions. Since the jet cross sections are known the fragmentation

functions can be disentangled from the calculated cross section. Because of *factorization*, the fragmentation functions are independent of the details of the hard scattering process. the cross section for hadron production, $d\sigma_c(l)$, are written in terms of a piece which depends only on the hard scattering cross section, $d\hat{\sigma}_a(l/z)$, and a piece which depends only on the parton fragmentation into a hadron, $D_{c/a}(z)$ [9]:

$$d\sigma_c(l) = \sum_a \int_0^1 dz d\hat{\sigma}(l/z) D_{c/a}(z) \tag{1.7}$$

The sum is over the different quark flavors and c is the final hadron type. l is the hadron momentum and z is the fraction of the parton momentum the hadron carries. Fragmentation functions can also be applied to different Q^2 using evolution equations. Measurements of fragmentation functions can be made in simple systems, such as $e^+ + e^-$ collisions and used in more complicated systems such as p+p collisions and perhaps Au+Au collisions.

String Model of Fragmentation The string model is a successful paradigm for understanding the fragmentation process. In this model, which is implemented in the event generator PYTHIA [10], the partons pull a "string" as they travel apart from each other. When the tension in this string, the potential energy between the partons, becomes large enough it breaks and a quark/anti-quark pair is created. The process continues until some low momentum cutoff where hadrons are formed from the produced quarks and anti-quarks. Baryon production in the string model comes from the production of a diquark/anti-diquark pair, which is suppressed due to the larger mass

compared to quark/anti-quark formation. This explains the reduced probability for producing baryons compared to lighter mesons in $e^+ + e^-$ and p+p collisions [11, 12, 13].

1.4.1 Jets

Jets were first observed in 1975 in $e^+ + e^-$ collisions at the SPEAR storage ring at SLAC [14] at $\sqrt{s}$=7.4GeV based on an event shape measurement, sphericity:

$$S = \frac{3}{2} \frac{(\sum_i p_{\perp,i}^2)_{min}}{\sum_i p_i^2} \tag{1.8}$$

$\sum_i p_{\perp,i}^2$ is the transverse momentum with respect to the axis that minimizes that sum, the jet axis. The lower the value of sphericity, the more collimated along a single axis the event is. In Figure 1.3 a jet Monte Carlo predicts a smaller average value of event sphericity than a Monte Carlo which just produces particles to fill phase space evenly. At center of mass energies of 6.2GeV and 7.4GeV there is a significant difference in the two model predictions and the data agree well with the jet model.

Jet Properties The simplest jet properties are the total energy, the multiplicity and the spatial width of the jet particles with respect to the direction of the initial scattered parton. The total energy is just that of the scattered parton, but the multiplicity and width provide information about the fragmentation process. Multiplicity measurements rely on jet finding algorithms, which are discussed below and are complicated by soft particles which are hard to assign definitively to jet or non-jet sources. The jet cone width decreases

with increasing jet energy because hadrons are formed with a characteristic p_T with respect to the parton direction, j_T. j_T has been measured to be constant as a function of jet energy [15], leading to more focused jet correlations for higher energy jets.

Sphericity and other event shape variables can statistically show jets in a sample of events, but they cannot determine if a single event contains a jet or not. Quantitative event-by-event jet finding is generally done by either cone jet finders [16, 17] where a large amount of energy inside a cone of half angle $R = \sqrt{\Delta\eta^2 + \Delta\phi^2}$ is defined as a jet. Cones have R of 0.7. The other main jet finder used in high energy physics is the $k_\perp$ jet finder [18] which combines particles with small emission angles.

In $e^+ + e^-$ and p+p collisions a jet event does not contain much background from other processes, but in head on heavy ion collisions there are thousands of particles particles produced, whereas a jet creates only a few. Consequently, normal jet finding algorithms cannot currently be used in heavy ion collisions. Event shape variables are also not useful, since the event shape will be determined primarily by the non-jet part of the event. Work is on-going to find individual jets in heavy ion collisions, since it will be very interesting to study in detail how the jet properties change in quark gluon plasma.

1.4.2 Hard Scattering in $e^+ + e^-$ Collisions

$e^+ + e^-$ collisions provide the simplest environment to study hard scattering. The two beam leptons annihilate to form a virtual photon which decays into a $q\bar{q}$ pair, each with the beam energy; cross sections for such processes can

be calculated perturbatively. The quarks then fragment into the final state hadrons which are observed in the detector.

$e^+ + e^-$ collisions provide the cleanest system in which to measure fragmentation functions. Because of factorization these fragmentation functions can then be used in other systems. Figure 1.4 shows fragmentation functions for quark and gluon jets as measured in the OPAL experiment [19]. Gluon led jets have a much softer fragmentation function and higher multiplicity than quarks led jets [20] because the color charge of gluons is larger than quarks. This increases the amount of gluon radiation in the fragmentation process [21]. The jet cross section falls faster with increasing jet energy than the fragmentation functions do with a final hadron carrying a larger fraction of the total jet energy. Thus a high energy particle is more likely to be at large z, the fraction of the jet p_T which is carried by a hadron, from a lower energy jet than at moderate z from a higher energy jet.

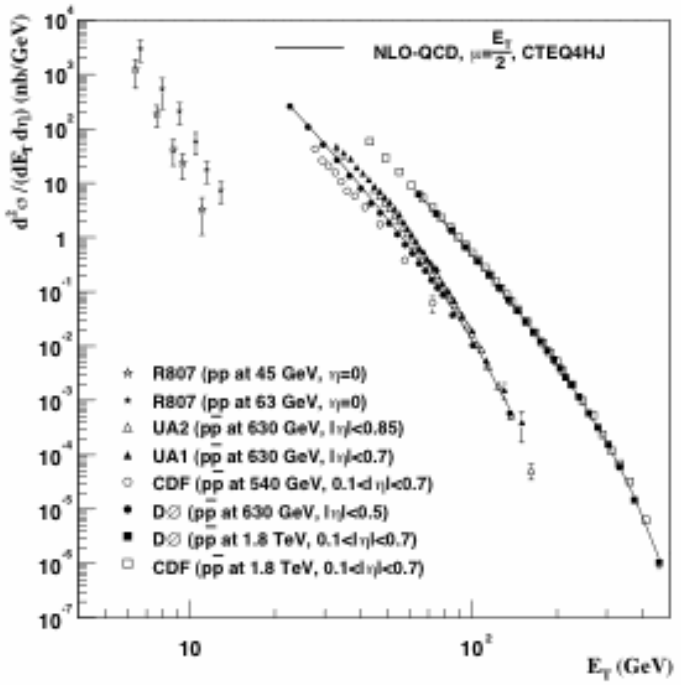

Figure 1.2: Jet cross section as a function of jet energy for a range of collision energy as observed in multiple experiments. Plot is from [8].

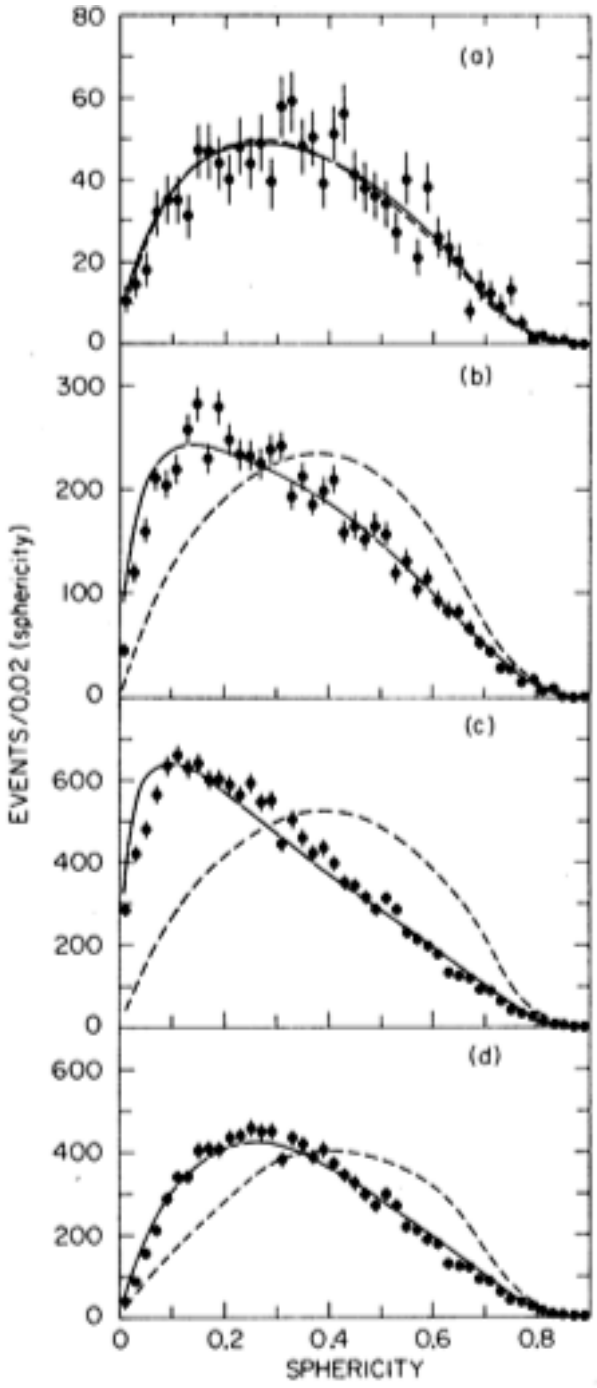

Figure 1.3: Event sphericity (see Equation 1.8 for center of mass energies of 3.0GeV (a), 6.2GeV (b), 7.4GeV (c) and 7.4GeV with largest $x < 0.4$ (d). Solid curves are a jet model and dashed curves are a phase space model. Plot is from [14].

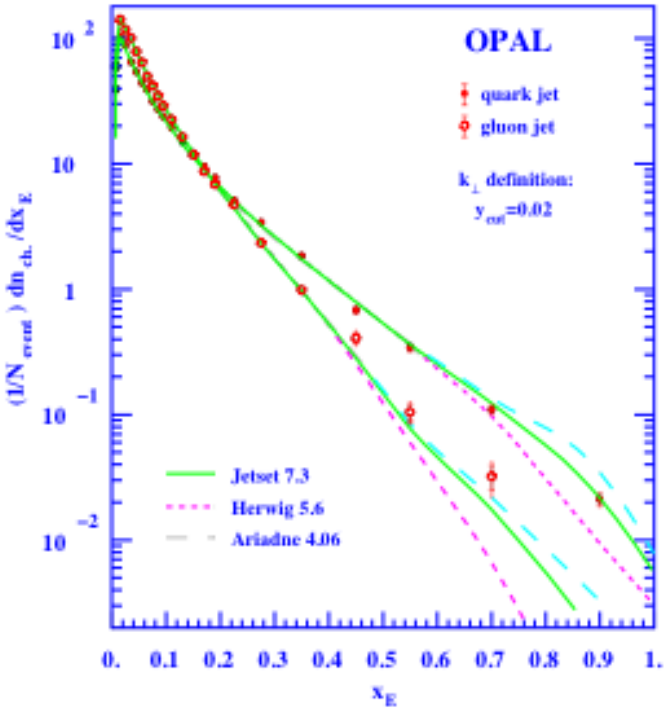

Figure 1.4: Fragmentation functions for quark and gluon jets as a function of $x_E = E/E_{jet}$ where E is the energy of the particle and E_{jet} is the energy of the jet. Plot is from [19].

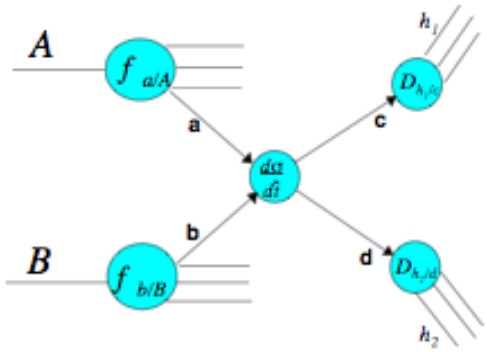

Figure 1.5: Schematic representation of a hard scattering between partons a and b in nucleons A and B respectively. $f_{a/A}$ and $f_{b/B}$ are the parton distribution functions. $\frac{d\sigma}{dt}$ is the hard scattering cross section for partons a and b into partons c and d. $D_{h/c}$ and $D_{h/d}$ are the fragmentation functions.

1.4.3 Hard Scattering in Hadron Collisions

The composite structure of nucleons makes them a less straightforward system for understanding hard scattering processes. In addition to pQCD cross section calculations and fragmentation functions, nucleon-nucleon collisions require knowledge of the probability for finding a parton of type a in a hadron of type A, the parton distribution functions. Like the fragmentation functions, parton distribution functions are not calculable in pQCD, but they are universal. Figure 1.5 schematically shows the ingredients to jet production in hadronic collisions.

Parton distribution functions (PDFs) are generally measured in deep inelastic scattering experiments (DIS). In DIS, there is an electron beam and a hadronic target. The electron scatters off one of the target protons producing a jet of hadrons and an outgoing lepton. If the momentum of the outgoing lepton is measured, the Q^2 of the interaction is known. The momentum difference between the incoming and outgoing leptons is the jet momentum.

The final hadron distributions are a convolution of the PDFs, the jet production cross section and the fragmentation functions, each of which can be measured or calculated independently due to factorization.

With the measured fragmentation functions from $e^+ + e^-$ collisions it is possible to calculate the single particle spectra in p+p collisions using pQCD. Figure 1.6 shows the p_T distribution for π^0s at $\sqrt{s}$=200GeV p+p collisions as measured in the PHENIX experiment along with a next to leading order pQCD calculation. Good agreement between the data and calculation is observed over eight orders of magnitude.

1.4.4 Hard Scattering in Au+Au Collisions

Hard scattering in Au+Au collisions occurs the same way that it does in p+p collisions, only scaled by the number of binary collisions. This is known because the production of direct photons (photons from the hard scattering process $q + g \rightarrow q + \gamma$) in Au+Au collisions scaled by the number of binary collisions agrees well with scaled pQCD calculations of p+p collisions [23] as can be seen in Figure 1.7 which compares the observed yield of direct photons to the yield expected from a pQCD calculation scaled by the number of binary nucleon-nucleon collisions. Photons do not interact via the strong force and thus escape the QCD medium essentially unmodified. The agreement between hard scattering in p+p and Au+Au collisions is because hard scattering occurs in the very early phases of the Au+Au collisions before any medium can be formed.

In Au+Au collisions, to escape the collision region the hard scattered par-

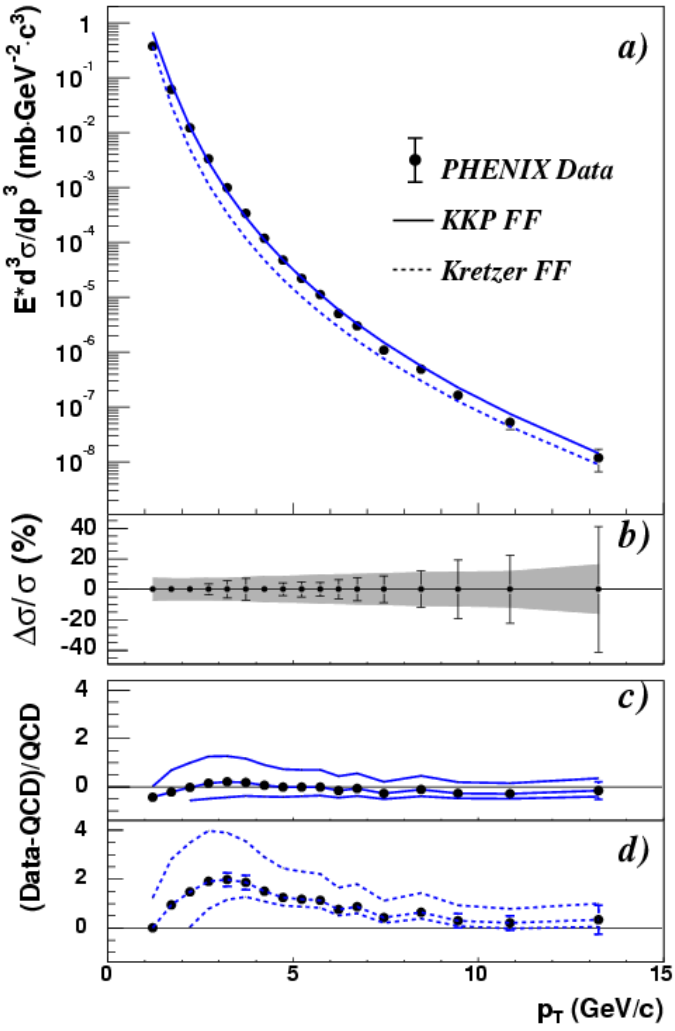

Figure 1.6: The top panel shows π^0 spectrum measured in the PHENIX experiment compared to a next to leading order (NLO) pQCD calculation with two different fragmentation functions. The relative error sizes are shown in (b). Panels (c) and (d) show the quality of the agreement between data and theory as a function of p_T . Good agreement is seen for p_T >2GeV/c . The figure is from [22].

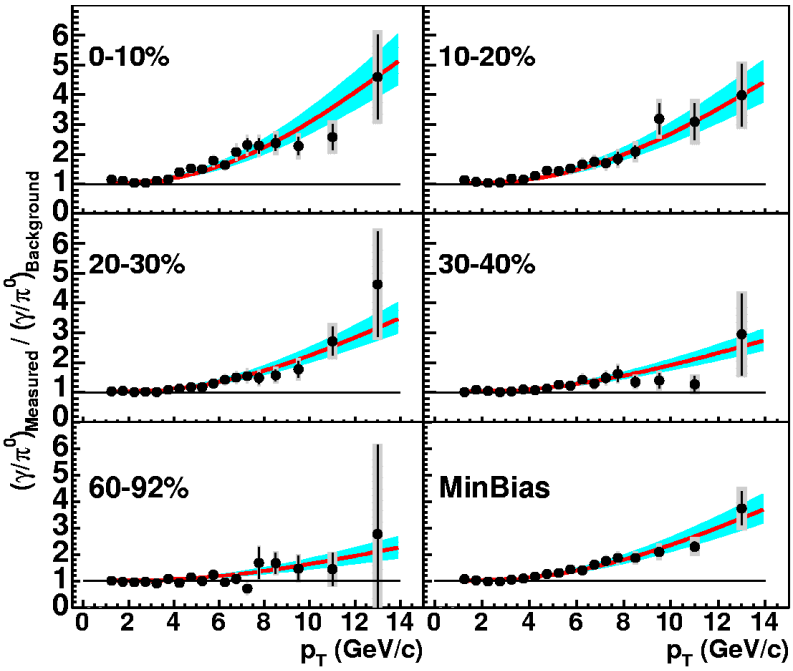

Figure 1.7: Double ratio of the inclusive photon spectra in Au+Au to the photon spectra expected from the measured hadron decays (such as $\pi^0 \rightarrow \gamma\gamma$) for both real data over a simulation based on the observed hadron spectra for five centralities and minimum bias. The red lines are a pQCD calculation scaled by the number of binary collisions. Figure is from [23].

tons must traverse the medium. The primary mode for interaction between the hard scattered partons and the medium partons is thought to be hard scattered partons to radiating gluons via bremsstrahlung after scattering off color charges in the medium [24]. This causes a depletion of high p_T partons compared to what is expected from binary scaled p+p collisions as can be seen in Figure 1.8 [25]. The solid data points are the charged hadron spectra as measured in Au+Au collisions divided by the charged hadron spectra from

p+p collisions multiplied by the number of binary collisions (N_{coll}):

$$R_{AA} = \frac{1/N_{evt} d^2N_{AA}/d\eta dp_T}{\langle N_{coll}\rangle/\sigma_p^{inel} p/d\eta dp_T} \tag{1.9}$$

. The hollow points are the same ratio, but for π^0s. An R_{AA} value of 1.0 at all p_T indicates that no nuclear effects occur; Au+Au collisions are a superposition of N_{coll} independent p+p collisions. Each panel shows a different centrality. In the most central collisions the R_{AA} values are much less than one at high p_T indicating that there are many less high p_T particles in Au+Au collisions than would be expected from N_{coll} scaled p+p collisions.

Figure 1.8 also shows a clear difference at intermediate p_T (between 2-5GeV/c) between the suppression of inclusive charged particles and π^0s. This difference is found to be due to the protons and anti-protons which do scale with the number of binary collisions at all centralities in Au+Au collisions; Figure 1.9 [26] shows the proton and anti-proton spectra scaled by $1/N_{coll}$ for four centralities. Above 2GeV/c, the lower limit of intermediate p_T, a universal scaling is observed. The physics of the intermediate p_T range is typically thought to contain elements of both hard and soft physics, while binary scaling is indicative of hard scattering processes. Single particle observables do not have the sensitivity to distinguish between binary scaling due to hard scattering processes and and accidental scaling caused by some unknown soft process. However, the presence of jet-like spatial correlations between protons and other particles would provide evidence for a hard scattering origin for at least some of the protons and anti-protons observed. Purely soft processes would not be expected to yield additional particles in the angular region characteristic of jet

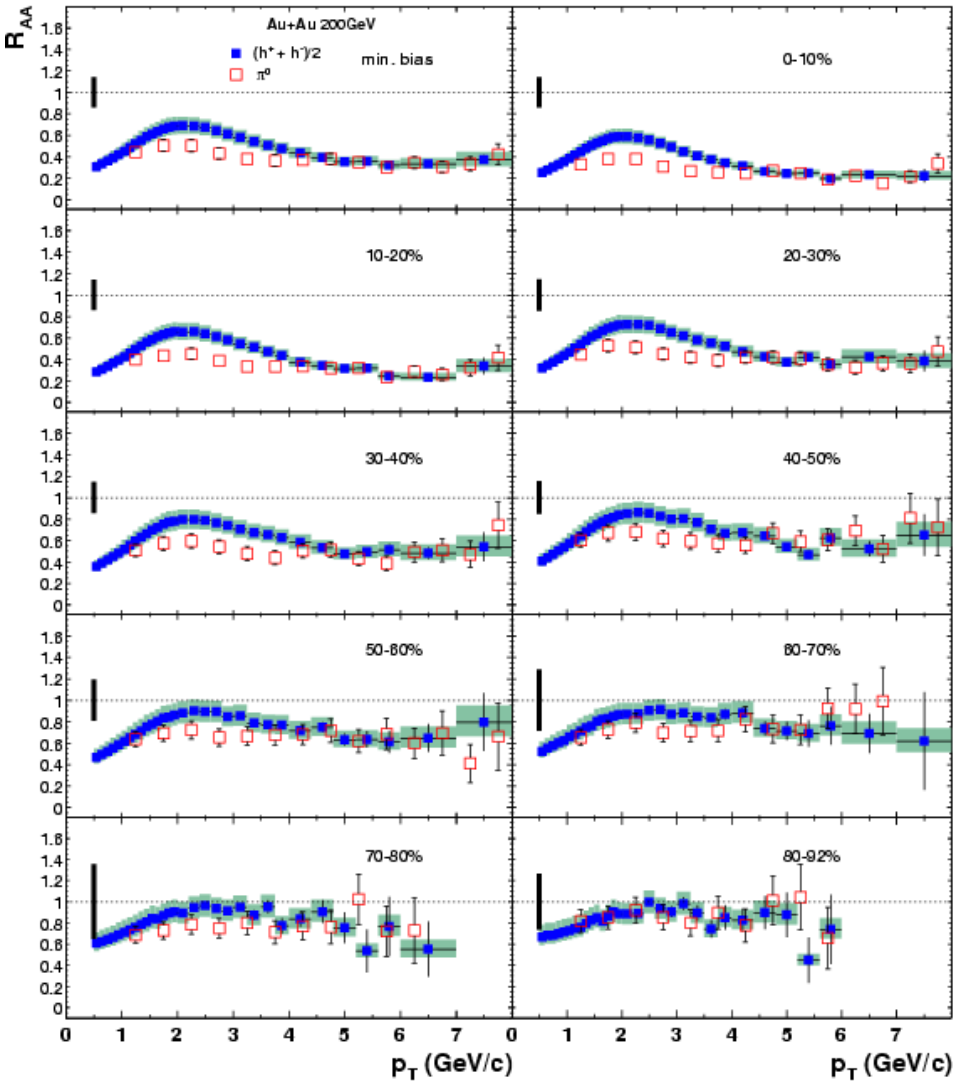

Figure 1.8: Ratio of hadron spectra observed in Au+Au collisions to binary scaled spectra from p+p collisions for nine centralities and minimum bias. A significant depletion of high p_T particles is observed for central collisions which peripheral collisions agree well with the binary scaling hypothesis. Solid points are for charged hadrons and hollow points are π^0s.

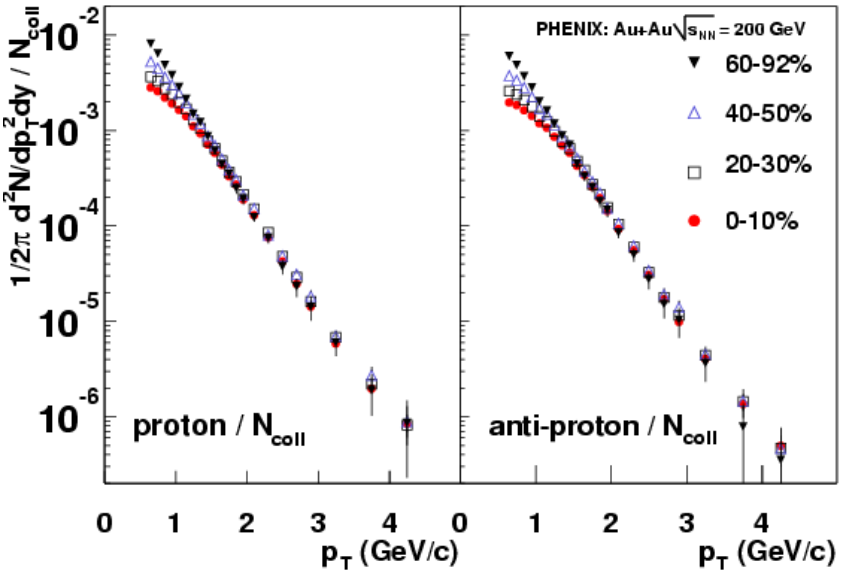

Figure 1.9: Proton and anti-proton spectra in Au+Au collisions scaled by the number of binary collisions.

fragmentation.

1.5 Hadron Production

1.5.1 Soft Particle Production

At p_T below roughly 2GeV/c the majority of particles in Au+Au collisions are not expected to come from jet fragmentation, but rather from soft processes. These processes are not well understood, but are characterized by Q^2 small enough such that the length scale involved is larger than the size of the nucleon. Coherence effects are expected to be important and cause violations of factorization. Thus, the universal fragmentation functions of jet particle production cannot be used here. Soft particle yields have been observed to scale with the number of participating nucleons, rather than the number of binary collisions in Au+Au collisions [27].

1.5.2 Elliptic Flow

For Au+Au collisions with finite impact parameters there exists an initial azimuthal asymmetry due to the almond shaped nuclear overlap region as shown in Figure 1.10. Initial multiple scattering collisions transform the initial state spatial asymmetry into a momentum asymmetry which makes it easier for particles to escape the collision region along the plane defined by the impact parameter and the beam axis, called the reaction plane, than perpendicular to it.

This asymmetry is quantitatively described by v_2 where:

$$\frac{dN}{d\phi} \propto 1 + 2v_2 \cos(2(\phi - \Phi_{RP})). \tag{1.10}$$

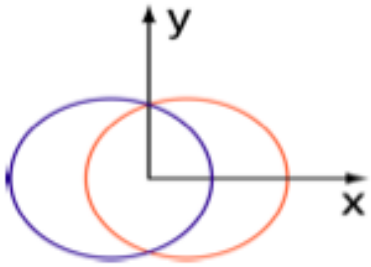

Figure 1.10: Illustration of the collision geometry in a non-central Au+Au collision. The reaction plane is the xz plane.

Φ_{RP} is the reaction plane angle and ϕ is the azimuthal angle. Higher order terms are small and are ignored. v_2 varies with particle type and p_T . At low p_T , below roughly 2GeV/c , v_2 values are well explained by hydrodynamic calculations which assume equilibrium established early in the collision and large pressure gradients leading to strong expansion of the system [3].

1.5.3 Baryon Excess

As seen in Figure 1.9, the spectra of baryons and anti-baryons at intermediate p_T in Au+Au collisions scales with the number of binary nucleon nucleon collisions for all centralities as opposed to the π^0 and inclusive charged particle spectra which, show a significant and increasing suppression compared to binary scaling in more central collisions. Another way of studying the baryon excess is via the p/π^+ and $\bar{p}/\pi^-$ ratios in different collision systems as a function of p_T. Figure 1.11 shows the p/π^+ ratio as a function of p_T for p+p, d+Au, peripheral Au+Au, and central Au+Au collisions as measured by PHENIX. There is approximately a factor of three increase in the value of p/π^+ at intermediate p_T . Since the increase is also seen in the $\bar{p}/\pi^-$ ratio, the increase cannot be due to baryons from the incoming nuclei being scattered to midrapidity. A larger than expected number of protons and anti-protons are created in the collision.

The ϕ meson provides a means of determining what caused the enhanced proton and anti-proton production. The ϕ has a mass of 1020MeV/c^2, approximately the mass of a proton, but it is a meson. If the ϕ yield at intermediate p_T scales similarly to that of the proton, then the process which alters the p/π^+ ratio is predominantly sensitive to the mass of the particle, but if the ϕ scaling is similar to that of pions the process is sensitive to valence quark number. Figure 1.12 [29] shows R_{CP} for identified protons and anti-protons, π^0s, and ϕs. R_{CP} is the binary scaled ratio of the spectra in central collisions (in this case 0-10%) to peripheral collisions (40-92%). Like R_{AA}, an R_{CP} value of 1 indicates binary scaling under the assumption that no nuclear effects are

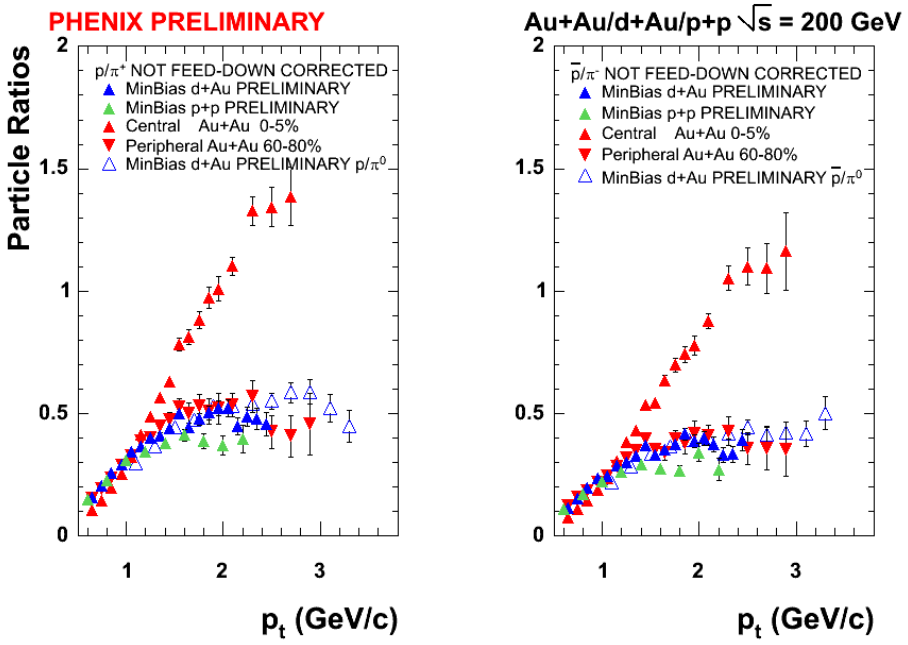

Figure 1.11: p/π^+ ratio (left) and $\bar{p}/\pi^-$ ratio (right) as a function of p_T for p+p, d+Au, peripheral Au+Au and central Au+Au collisions. The p and $\bar{p}$ do not have the contribution from λ and $\bar{\lambda}$ decays removed. Figure is from [28].

present in peripheral collisions. Both the ϕ and the π^0s are clearly suppressed relative to binary scaling, while the protons and anti-protons show binary scaling. This is suggests that the proton excess is caused by a process which is unique to baryons.

The p_T region where the baryons are enhanced relative to the mesons is intermediate p_T 2-5GeV/c , where both soft and hard processes are expected to be important particle production mechanisms. The goal of this work is to determine whether hard or soft processes are primarily responsible for the baryon excess.

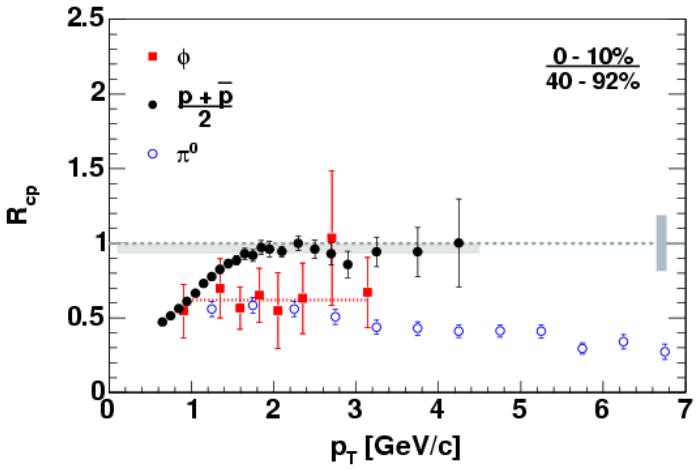

Figure 1.12: R_{cp} for protons and anti-protons, π^0s and ϕ mesons. Binary scaling is observed for protons and anti-protons, while the π^0s and ϕs are suppressed.

1.5.4 Recombination/Coalescence

Recombination is the idea that final state hadrons are produced by valence quarks from the thermal medium, which are close together in phase space. The theory was first developed by Das and Hwa [30] to explain hadron production in the forward region of p+p collisions. Due to the baryon excess [26] and valence quark number scaling of v_2 [31] at RHIC there has been work on explaining midrapidity hadron production at intermediate p_T by such models [32, 33, 34] where the valence quarks come from the thermal medium. Hadron production by recombination is expected to dominate over fragmentation as long as the parton p_T spectra is exponential. This is because recombination involves adding quark momenta together; each valence quark adds its momentum to the final hadron's momentum. Baryon production is enhanced because of the extra quark momentum compared to mesons. In fragmentation

the hadron momentum must be less than the parent parton's momentum because multiple final state hadrons come from each fragmenting parton. Figure 1.13 [35] schematically shows this. With an exponential p_T spectrum lower p_T quarks are so much more abundant than high p_T quarks that the chances for lower p_T quarks to recombine are much higher than the chance for a higher p_T quark from a hard scattering to fragment into the final state hadron. Recombination models assume that all gluons become quark/anti-quark pairs and then recombine. If recombination models can explain the data, it implies that there is a large thermalized source of quarks and anti-quarks and is strong evidence for quark gluon plasma formation at RHIC [36].

Figure 1.14 shows a calculation from [32] showing the fraction of hadrons expected to come from recombination as a function of hadron type, p_T, and centrality in Au+Au collisions. The most striking thing about Figure 1.14 is the dominance of recombination at all centralities. including peripheral events where a large medium is not created. An impact parameter of 12fm, corresponding to the peripheral curves in Figure 1.14, corresponds to a centrality of approximately 65% and approximately 22 participating nucleons. According to Figure 1.14 95% of the protons and anti-protons and 50% of the pions come from recombination at this impact parameter. In contrast, the data in Figure 1.11 though show a p/π^+ ratio in that centrality which is very similar to what is observed in p+p collisions. Thus, either the calculation over estimates the importance of recombination or recombination must be considered even for midrapidity particle production in p+p collisions.

Calculations for d+Au collisions have been done with a recombination model [37, 38] and can explain the spectra for pions [39, 40] and protons

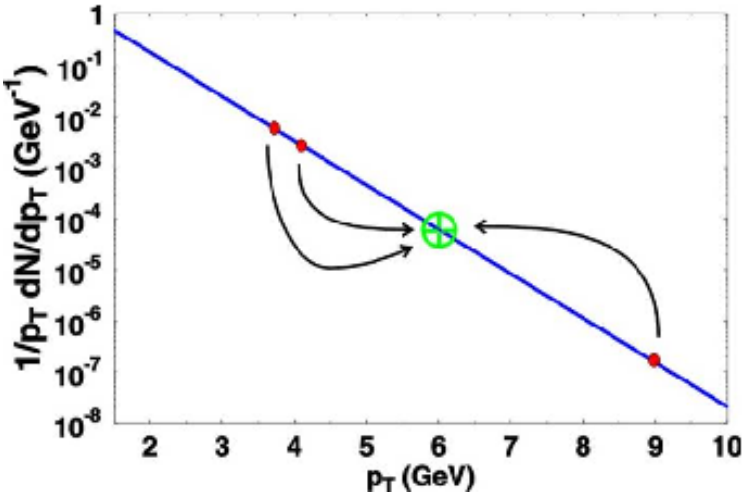

Figure 1.13: Illustration of why recombination is expected to dominate hadron production as long as the parton p_T spectrum is exponential from [35]. When the parton p_T becomes power law in shape, fragmentation becomes more important due to the enhancement of high p_T partons.

[40] in terms of recombination. Because of this sensitivity, a good test of recombination models in general is how well they can simultaneously explain both peripheral and central Au+Au and d+Au data.

One important property of recombination is that correlations between the quarks are amplified according to the valance quark content of the final state hadrons. The elliptic flow of hadrons, v_2^h, is related to the quark v_2 by

$$v_2^h(p_T) = n v_2(\frac{p_T}{n})$$

where n is the number of valance quarks (two for a meson and three for a baryon) and p_T is the hadron transverse momentum [32]. This v_2 scaling is observed in the data, as seen in Figure 1.15 from [31], and was one of the main reasons for enthusiasm about the applicability of recombination models to heavy ion collisions.

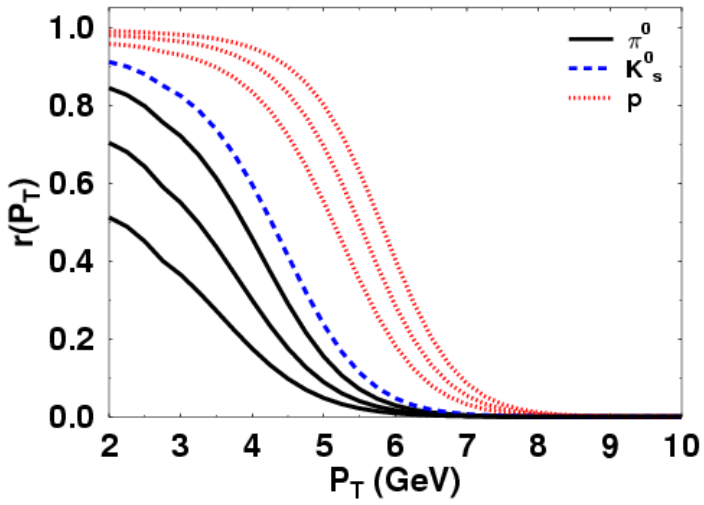

Figure 1.14: Fraction of hadrons in Au+Au collisions which come from recombination at impact parameters (from greatest fraction) of 0, 7.5 and 12fm from [32] (larger fraction of particles from recombination correspond to smaller impact parameters). For K only impact parameter of 0fm is shown.

1.6 Goal of this Analysis

In this work we will investigate jet-like azimuthal correlations between two particles where one or both is identified at intermediate p_T . Two particle correlations provide additional information to can discriminate between particle production mechanisms than single particle observables.

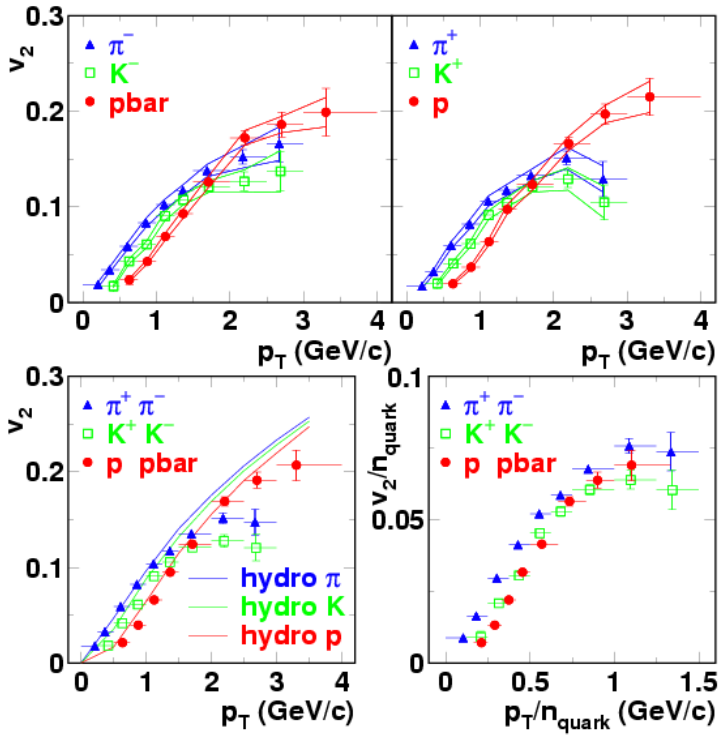

Figure 1.15: The lower right hand panel shows v_2 scaled by valence quark number as a function of p_T scaled by valence quark number for charged pions, kaons and protons and anti-protons. A nearly universal scaling is observed in values of p_T/n corresponding to intermediate p_T.

Chapter 2

The PHENIX Experiment

2.1 PHENIX Overview

The PHENIX experiment at RHIC is a large multi-purpose detector optimized to measure identified hadrons, high p_T hadrons, photons and leptons. PHENIX consists of two central arms for charged and neutral particle measurement at midrapidity, two muon arms for muon measurements at forward and backward rapidities and detectors at high rapidity for measuring global event characteristics. Figure 2.1 shows an schematic overview of the PHENIX detector. Figure 2.2 shows a schematic outline of the central and muon arms.

The PHENIX coordinate system is defined with respect to the beam direction, which is labeled the z axis (positive z points toward the North Muon Arm). The polar angle with respect to this axis is θ. The azimuthal angle around the z axis is ϕ with ϕ =0 parallel to the hall floor pointing into the West Arm.

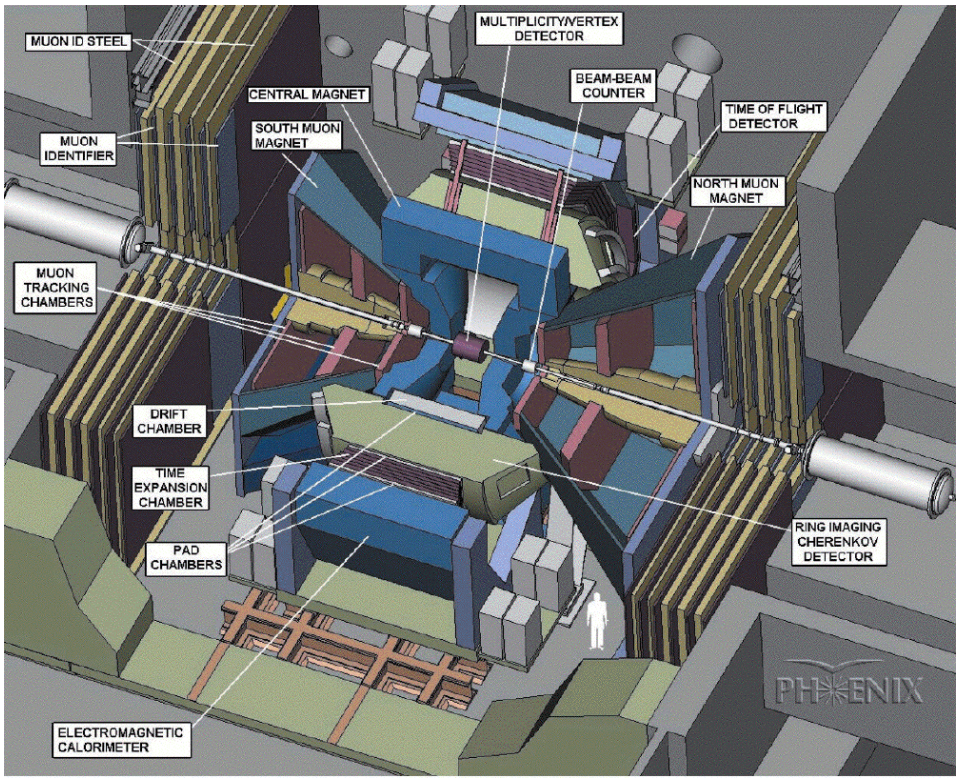

Figure 2.1: A drawing of the PHENIX experiment

2.2 PHENIX Vertex and Trigger Detectors

2.2.1 Beam-Beam Counters

PHENIX has two Beam-Beam Counters (BBCs) located at pseudo-rapidity of $\pm|3.0 - 3.9|$ with full azimuthal coverage. Each BBC consists of 64 quartz Cherenkov detectors. Identical BBC's are installed on the North and South sides of PHENIX and are located 144 cm from the center of the interaction region directly behind the central magnet. The BBC's main functions are to measure the vertex position along the z axis, to trigger minimum bias events and to provide a start signal for the PHENIX TOF system based on the average hit time in each BBC. More detailed information on the BBC's can be found

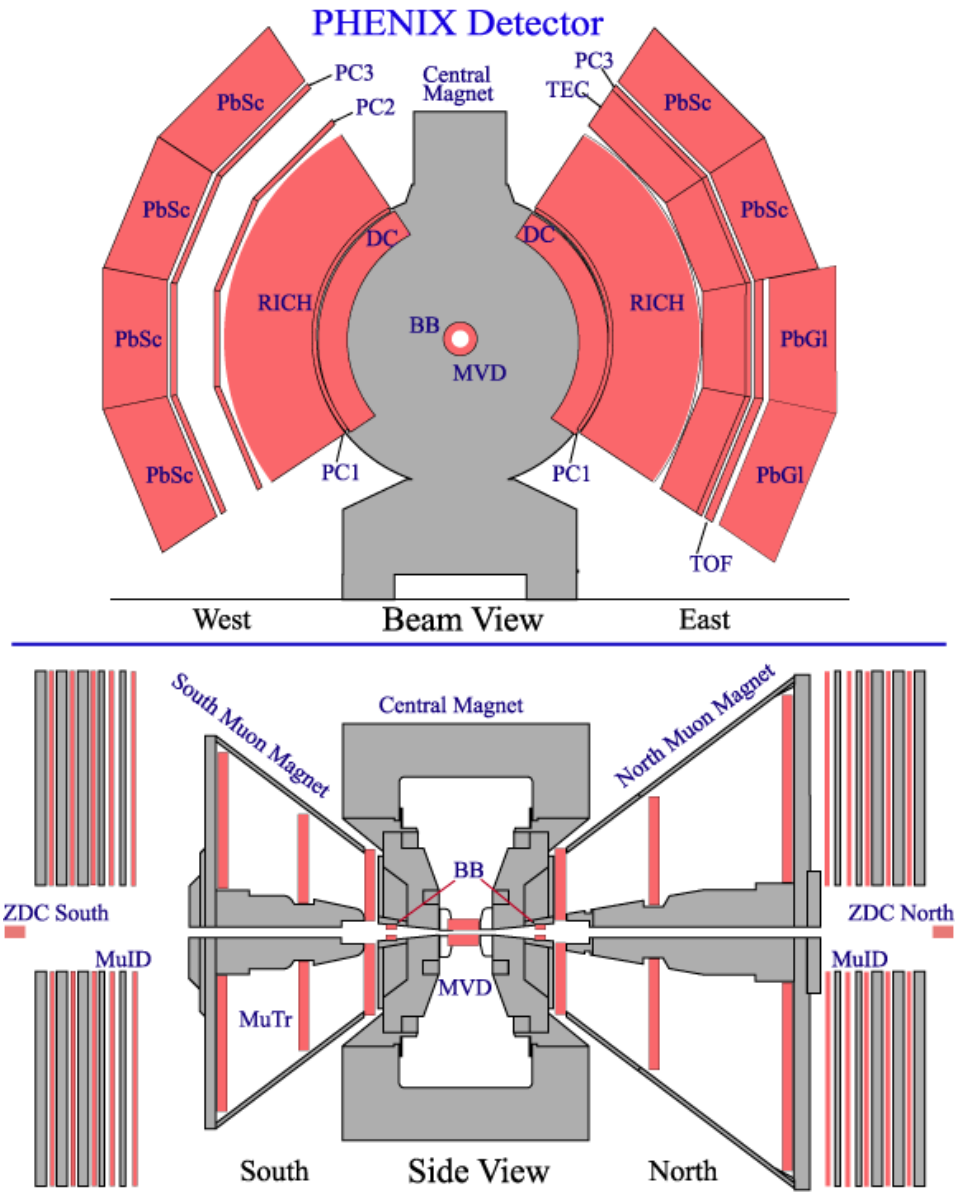

Figure 2.2: A drawing of the PHENIX experimental setup when the Au+Au data used for this analysis was taken. The top panel shows a beam view of the Central Arm detectors and the bottom panel shows a side view showing the placement of the Muon Arms and the global detectors: Beam Beam Counters (labeled BB), Zero Degree Calorimeters (ZDC North and South) and Multiplicity Vertex Detector (MVD).

in Reference [41].

2.2.2 Zero Degree Calorimeters

The Zero Degree Calorimeters (ZDC)are small hadronic calorimeters which measure neutral energy. They exist in all four RHIC experiments. In PHENIX they are near the muon identification system along the beam pipe direction 18 m to the North and South of the collision region. The time difference between the neutron signals in the ZDC North and ZDC South can be used to determine the vertex position along the z. This is used when the BBC is not able to reconstruct the vertex. For further information on the ZDC's see Reference [42].

2.2.3 PHENIX Centrality Measurement

The centrality in PHENIX Au+Au collisions is determined with a correlation of the charge measured by the BBC and the energy deposited in the ZDC. The BBC signal is proportional to the total number of collision participants, N_{part} until the most central collisions where the BBC is saturated. The ZDC energy is proportional to the number of spectator neutrons, those neutrons from the Au nuclei uninvolved in the collision which continue forward in the beam direction. Figure 2.3 shows the normalized ZDC energy distribution as a function of the normalized BBC charge distribution. The solid lines mark the different centrality selections. Low centralities correspond to events with a small impact parameter. For a further discussion of centrality see Section 1.3.1.

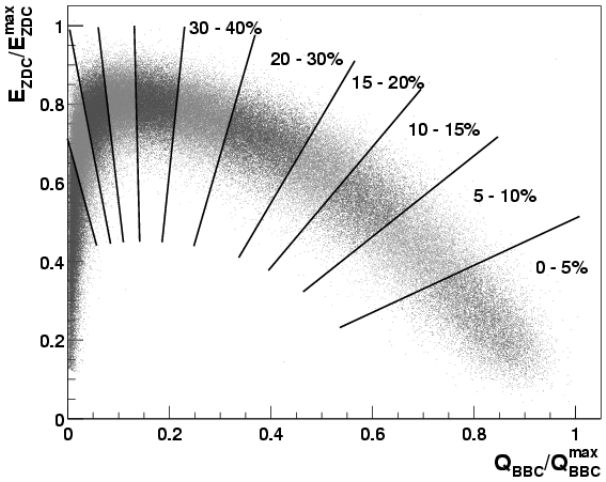

Figure 2.3: Fractional ZDC energy distribution as a function of fractional BBC charge distribution for minimum bias Au+Au collisions. The solid lines indicate centrality selections for the Run 2 data [27].

centrality	N_{part}	sys. err.	N_{coll}	sys. err.	b (fm)	sys. err.
0-5%	351.4	2.9	1065.4	105.3	2.3	0.1
5-10%	299.0	3.8	845.4	82.1	4.1	0.2
10-20%	234.6	4.7	602.6	59.3	5.7	0.3
20-40%	140.4	4.9	296.8	31.1	8.1	0.4
40-60%	60.0	3.5	90.7	11.8	10.5	0.4
60-70%	25.7	3.8	28.5	7.6	11.9	0.5
60-90%	14.5	2.5	14.5	4.0	13.0	0.5

Table 2.1: Glauber model results for the number of collision participants, number of binary collisions and the impact parameter (b) along with the systematic errors for the centrality bins used in this analysis.

In this analysis six centrality bins are used in Au+Au collisions: 0-5%, 5-10%, 10-20%, 20-40%, 40-60% and 60-70% (60-90% in Run 4). The statistics of the final measurement do not allow finer centrality bins or a measurement for collisions more peripheral than 70% in Run 2. The Glauber model results for the centrality bins used here are shown in Table 2.1.

2.3 PHENIX Charged Particle Measurements in the Central Arms

2.3.1 Drift Chambers

The two PHENIX drift chambers each cover $\pi/2$ in azimuth and $180cm$ in the z direction centered around midrapidity. The drift chambers are positioned outside the magnetic field from 2.02m to 2.46m radial distance from the interaction point. Charged particles passing through the drift chamber ionize the gas mixture, 50% argon and 50% ethane with <1% alcohol. The electrons released are measured on sense wires. The hit position is measured by the time the electrons hit the wire. Each track consists of many hits. Momentum measurements are made by measuring the angular deflection of the track from a straight line trajectory through the collision vertex. The drift chambers are also used to measured the azimuthal angle of the tracks.

Each drift chamber consists of 20 sectors each with six wire layers: X1, U1, V1, X2, U2 and V2. Figure 2.4 shows a side view of a single sector. There are four types of wires in the drift chamber, as shown in the inset of Figure 2.4. Potential wires are the wires which create the drift electric field in the detector. The sense wires are the wires which collect the signal charge for the hits. The gate wires further shape the field to direct the charge toward the sense wires from one side. The back wires block charge from the other side from reaching the sense wires. This prevents left-right ambiguities in the hit position; alternating sense wires collect charge from alternating sides. The U and V wire layers are oriented at an angle, $\approx 6^o$, with respect to the X layers;

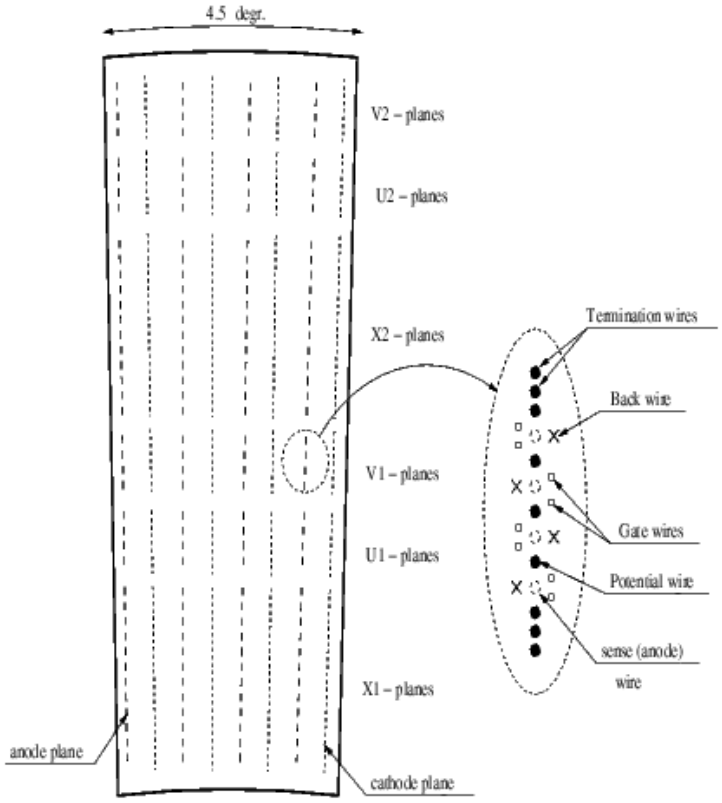

Figure 2.4: Side view of a drift chamber sector showing the positions of the wire layers. Also shown is the wire positions for the V1 layer (other layers are similar).

opposite ends of the U and V layers are in neighboring sectors (see Figure 2.5). The U and V layers provide z position information on the tracks. The drift chamber provides spatial resolution better than 0.15mm in the ϕ direction, two track separation better than 1.5mm and spatial resolution in the z direction better than 2mm. The single wire efficiency is $\approx$95%; the single track efficiency is $>$99%.

High quality reconstructed tracks in the drift chamber, the only kind used in this analysis, have hits in both the X1 and X2 layers and information from

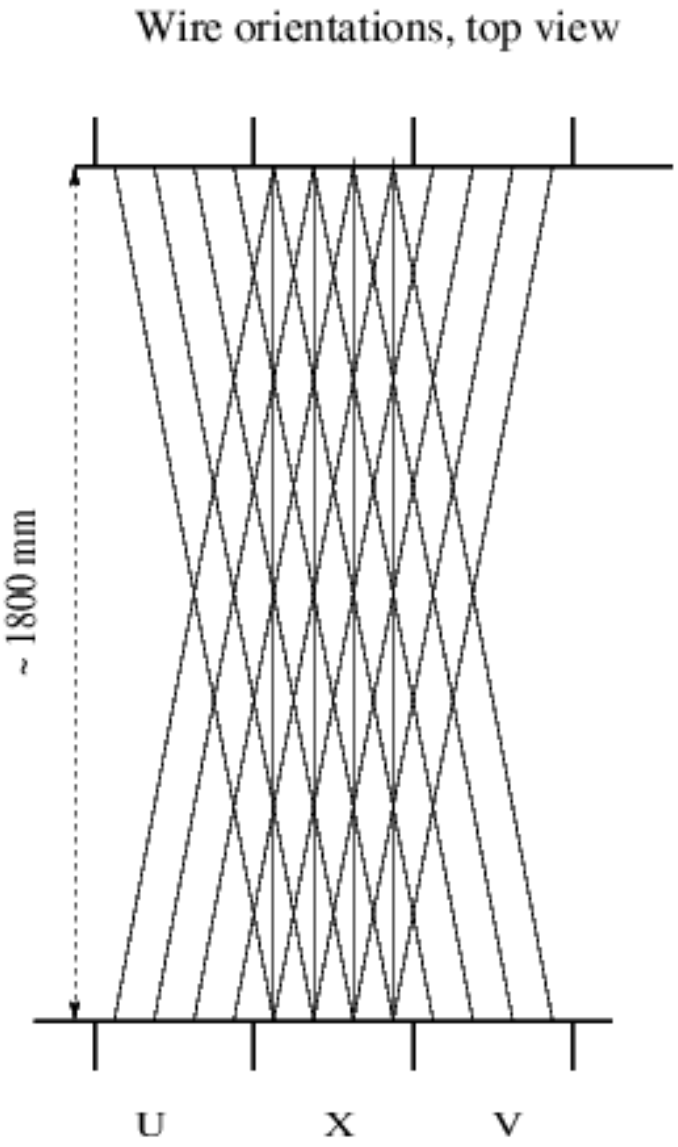

Figure 2.5: Top view of the wire orientations for the X, U, and V layers. U and V wires are oriented at $\approx 6^o$ with respect to the X wires to provide z information about the hit.

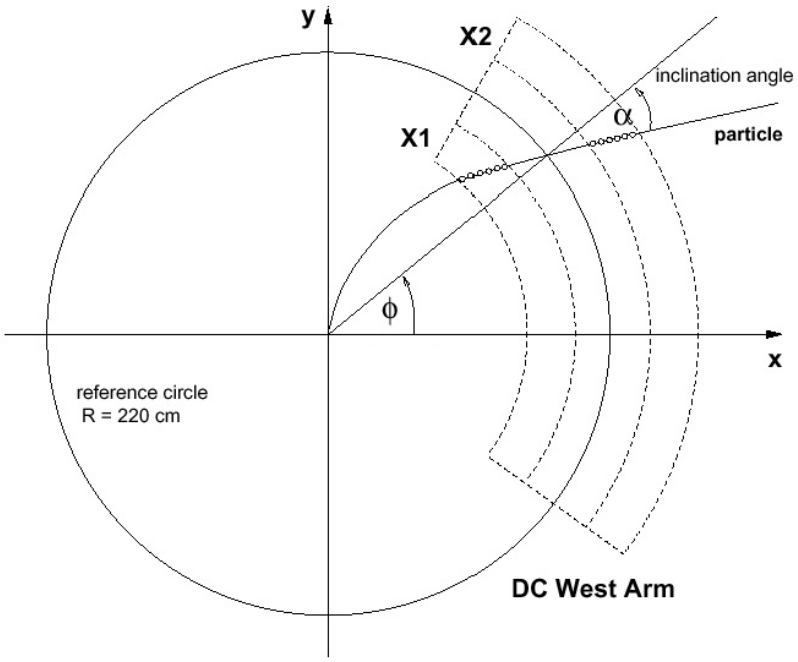

Figure 2.6: A drawing of tracking parameters for the drift chamber. α is the track's deflection from a straight line and ϕ is the azimuthal angle of the track measured at the drift chamber reference radius of 220cm.

the stereo wires which aid PC1 (discussed in the next section) in the determination of the track z position.

Momentum measurements are made by measuring the tracks angular deflection from a straight line, α (see Figure 2.6). α is inversely proportional to the track momentum. The momentum resolution of high quality tracks in the drift chamber is $\delta p/p = 0.7\% \oplus 1.0\% p$ (GeV/c) for the Au+Au in Run2 and $\delta p/p = 0.7\% \oplus 1.1\% p$ (GeV/c) for the d+Au and p+p data.

Tracks in the drift chamber are reconstructed via a combinatorial Hough transform. All hit combinations are plotted in $\phi - \alpha$ space where good quality tracks show up as peaks.

Additional information about the drift chambers can be found in Reference

[43].

2.3.2 Pad Chambers

The PHENIX Pad Chambers (PC) are multi-wire proportional chambers that are part of the PHENIX central tracking. Each PC is a single plane of wires bounded by two cathode planes, one of which is segmented into pixels. The pad chambers consist of three layers in the West Arm (PC1, PC2 and PC3) and two layers in the East Arm (PC1 and PC3). PC1 East and West are directly behind the drift chambers in both arms and are used as part of the system to identify good tracks by associating a PC1 hit with a drift chamber track. All good tracks have a PC1 association and the track z measurement comes from PC1. PC2 and PC3 are located farther away from the interaction region (4.2m for PC2 and 5.0m for PC3) and a match between a track projection based on the DC track information and a hit in PC2 or PC3 is used to confirm good tracks and reduce background from photon conversions and particle decays. More information about the Pad Chamber system can be found in [43].

2.3.3 High Resolution Time of Flight

The PHENIX Time-of-Flight (TOF) detector provides high resolution particle identification of charged particles in the East Arm of PHENIX with an azimuthal acceptance of $\pi/8$. The resolution of $\approx 120ps$ is sufficient to separate p from K at the 4σ level to $p \simeq$4GeV/c .

The TOF consists of 960 scintillator slats oriented along the $r-\phi$ direction at a radius of $5.1m$, situated behind PC3 and in front of the EMCal. The

scintillators are divided into 10 panels of 96 segments each. Each slat has photo-multiplier tubes at both ends. Hit position information comes from the time difference between the signal on the two ends of the slat.

Particle identification based on the time of flight, t_{TOF}, measurements from the BBC and TOF, the track momentum, p, and the path length, L, from the collision vertex to the TOF. The m^2 of the particle is described by:

$$m^2 = \frac{p^2}{c^2}((\frac{t_{TOF}}{L/c})^2 - 1). \tag{2.1}$$

Identification is based on the difference between the observed m^2 and that expected from the known particle mass. Figure 2.7 shows the TOF particle separation in the Run2 Au+Au dataset. For further details about the PHENIX TOF see Reference [44].

2.3.4 TOF with Electro-Magnetic Calorimeters

PHENIX has two independent Electromagnetic Calorimeters (EMCal) designed to measure the position, energy and time of flight of photons and electrons. The Lead-Scintillator Calorimeter (PbSc) is a sampling calorimeter made of alternating layers of Pb as an absorber and scintillator to generate light. The PbSc covers all of the West Arm of PHENIX and the top half of the East Arm of PHENIX. The bottom half of the East Arm has has a Lead Glass Calorimeter which is a homogeneous lead-glass Cherenkov radiator.

Particle identification in the PbSc calorimeter is done in the same manner as in the TOF. The timing resolution allows the separation of of K from p to $p_T \approx$2.5GeV/c with a much larger acceptance than the TOF. More information

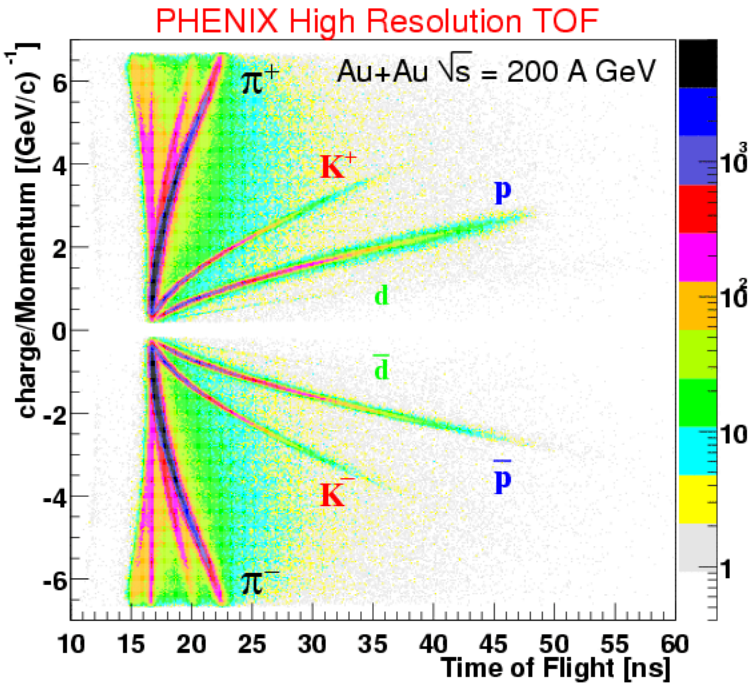

Figure 2.7: Charge divided by momentum as a function of measured time of flight in the PHENIX TOF for the Run2 Au+Au data.

on the PHENIX calorimeters can be found in [45].

2.3.5 PHENIX Central Magnet

The PHENIX Central Magnet provides an axially symmetric field parallel to the beam pipe. Charged particles bend in a plane perpendicular to the beam axis and their deflection is measured with the drift chambers to provide momentum measurements. Figure 2.8 shows the magnetic field lines for both the Central Magnet and the North and South Muon Magnets. The central magnet field is ≈0.48T in the Run 2 and 3 data at $r = 0$ and decreases with increasing radius. In Run 4 the inner coil was turned on increasing the

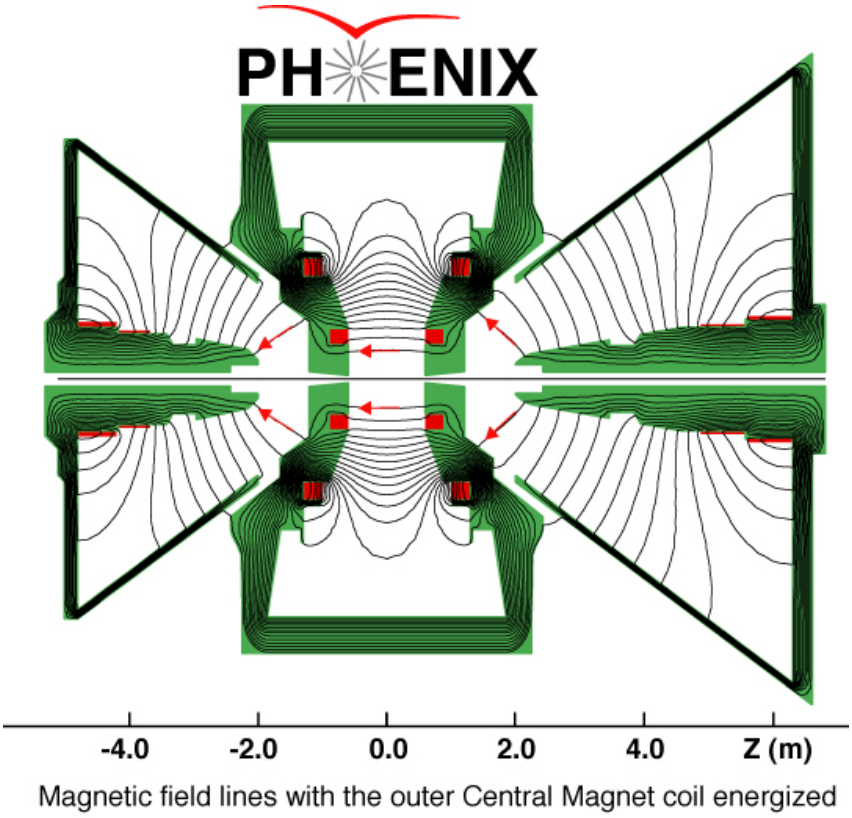

Figure 2.8: Magnetic field lines for the PHENIX magnets.

magnetic field strength. The field varies with z as well, but is nearly constant in the range covered by the drift chamber.

Chapter 3

Jets and Two Particle Azimuthal Correlations

As was discussed in Section 1.4 jets consist of particles in close proximity. The measurements of the baryon excess discussed in Section 1.5.3 could not determine whether the extra baryons came associated with other particles as would be expected from jets. Here we describe the two particle correlation technique which is used to get additional information on the jet structure of the baryon excess source.

Two particle correlations are an important tool for finding small structures which would otherwise be lost in the high multiplicity environment of central Au+Au collisions. In addition to jet correlations [46, 47, 48, 49, 50], two particle correlations have also been used to study elliptic flow [31] and Hanbury-Brown Twiss (HBT) correlations [51] in Au+Au collisions. Two particle azimuthal angular correlations are the distributions of azimuthal angular differences between pairs of particles of interest. Jets will create particles

nearby in $\Delta\phi$, typically within $\approx 1 rad$; di-jets, the jet from the opposing hard scattered parton should create a similar structure around $\Delta\phi = \pi$. We will study two particle correlations either of two particles from the same jet (near side correlations) or one particle from each of the jets making up a di-jet pair (away side correlations).

3.1 Jets and Azimuthal Correlations

The jets we aim to study in this analysis consist of a particle with $p_T > 2.5\text{GeV}/c$, the *trigger*, and some number of lower p_T particles *partners*. In a low multiplicity environment, such as p+p collisions, it is possible to pick such jets out in a single event basis by looking for clusters of a few particles in the detector. In a high multiplicity environment, such as central Au+Au collisions, such clusters may still remain, but they are overshadowed by a huge non-jet background. Most nearby particles are uncorrelated with each other. For this reason, finding jets on an event by event bias in Au+Au collisions has not yet been accomplished. Instead, we make distributions of pairs as a function of their azimuthal angular difference, $\Delta\phi$. Correlations of particles in this variable, as is expected from jets, will be visible above the background which is not correlated with the trigger in $\Delta\phi$ beyond correlations from elliptic flow.

The jets found by the two particle correlation technique are different than the average jet with the same total p_T because in order to reduce the combinatoric background two relatively high p_T particles are required. These particles are, on average, expected to carry most of the jet's total p_T . For un-biased jets,

the expectation would be that a jet of a given p_T would be made up of more particles of lower p_T. This is because the jet production cross section, Figure 1.2, has a steeper p_T dependence than the fragmentation functions, Figure 1.4. Thus, a trigger particle of a given p_T is likely to be carrying most of the energy of a lower energy jet. Jets with a high p_T particle do not look like the average jet of the same energy which does not have such a particle. Requiring a second high p_T particle, as in this analysis, further increases the bias. Therefore, caution is needed when attempting to understand jet properties from two particle correlation measurements. However, two particle correlations provide an unbiased way to determine if some fraction of the baryon production is from a jet source by comparing the yield of correlated particles as a function of collision system and centrality.

3.2 Azimuthal Correlations in PHENIX

If the azimuthal acceptance of the detector is non-uniform as in PHENIX, *mixed pairs*, where each particle is from a different event, must also be created. The distribution of azimuthal angular difference, $\Delta\phi$, these pairs also needs to be measured. This measures the pair acceptance of PHENIX. This acceptance varies with the p_T of both particles, the z vertex of the events used and the event centrality. The acceptance dependence on z vertex is because events populate the detector differently depending on where the collision vertex is in relation to the detector. The pair acceptance dependence on centrality is due to edge effects near dead regions in the detector. When the detector is full of tracks the chance of finding a random match in PC3 is reduced when

the track hits near the edge of a dead area, whereas in peripheral events the chance of finding a random track is very small at all locations. The change in the acceptance correction with centrality is ≈2% [52].

The p_T dependence is due to tracks bending in the magnetic field.

Dividing the $\frac{dN}{d\Delta\phi}$ from real pairs by that from mixed pairs corrects for the detector non-uniformities. If the real pairs contained no azimuthal correlations the resulting distribution would be flat in $\Delta\phi$.

The PHENIX detector non-uniformities in $\Delta\phi$ are large. Figure 3.1 shows the mixed pair distribution measured in PHENIX for one particle with $2.5 < p_T < 4.0\text{GeV}/c$ and a hit in the TOF wall and the second particle with $1.7 < p_T < 2.5\text{GeV}/c$ measured anywhere in the central arms, confirmed with a matching hit at PC3. The placement of the TOF at the bottom half of the East Arm causes a region of no acceptance near $\Delta\phi = \pi/2$.

The total integral of the acceptance correction is normalized to π for each p_T , centrality and z vertex bin. With this normalization the average efficiency for measuring the partners is unchanged (the average value for the acceptance correction is 1.0), but the relative efficiencies as a function of $\Delta\phi$ are equalized. It is easy to see that in the limiting case of a perfect detector this normalization, correctly, does not change the signal distribution. Following this correction the single particle efficiency correction for the partner particles can be applied to get the proper overall normalization.

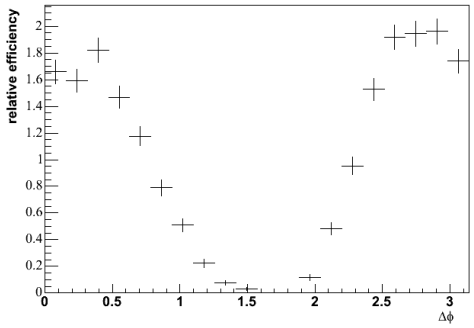

Figure 3.1: Mixed pair distribution in PHENIX.

3.3 Mathematical Framework for Two Particle Correlations

Once the distributions have been corrected for acceptance the small centrality and z vertex bins the analysis is done in (see Section 4.4) can be combined. Mathematically this is:

$$\frac{1}{N_{trig}}\frac{dN}{d\Delta\phi} = \frac{1}{\epsilon \sum_i N_{trig,i}}(\sum_i \frac{dN_{real,i}/d\Delta\phi}{Acc_i(d\Delta\phi)}) \tag{3.1}$$

the summation is over the centrality and z-vertex bins. The acceptance correction, $Acc_i(\Delta\phi)$, is the mixed pair distribution for bin i, normalized such that the total integral of π. $N_{trig,i}$ is the total number of triggers (with and without partners) in centrality and z vertex bin i. N_{trig} is the total number of triggers in all centrality and z vertex bins. ϵ is the correction for detector efficiency and acceptance and will be discussed in Sections 4.5.1 and 4.5.2. The quantity on the left in Equation 3.1 includes both the combinatoric background from the underlying event and the signal. In this analysis we assume

that the combinatoric background is constant as a function of $\Delta\phi$ except for the correlations caused by elliptic flow. The flow correlations modulate the combinatoric background level, $n_{comb,i}$ by

$$1 + 2v_2^{trigger}v_2^{partner}\cos(2\Delta\phi) \tag{3.2}$$

Methods for calculating $n_{comb,i}$ will be discussed in Section 3.4. The resulting distribution of jet correlated partners per trigger, $J(\Delta\phi)$ is:

$$J(\Delta\phi) = \frac{1}{\epsilon\sum_i N_i}(\sum_i \frac{dN_{real,i}/d\Delta\phi}{Acc_i(d\Delta\phi)})) - n_{comb,i}(1 + 2v_2^{trigger}v_2^{partner}\cos(2\Delta\phi) \tag{3.3}$$

In order to quantify the partner jets for the same jet and opposing di-jet the near side yield is:

$$\int_0^{0.94} J(\Delta\phi)d\Delta\phi \tag{3.4}$$

and the away side yield is:

$$\int_{2.0}^{\pi} J(\Delta\phi)d\Delta\phi. \tag{3.5}$$

The integration ranges were chosen to contain as much of the near and away side jet as possible while avoiding the regions in $\Delta\phi$ where PHENIX has small acceptance. These quantities contain varying fractions of the jet associated partners per trigger depending on the jet width, but they do not require any assumptions about the jet shape or any fitting of $J(\Delta\phi)$.

3.4 Combinatoric Background Normalization

Two equivalent methods are used to determine n_{comb}.

The first method involves the study of mixed events. These events are created by sampling from the single particle number distributions of triggers and partners, independently; mixed events contain the same number of uncorrelated pairs as real events (real events of course also contain correlated pairs–the signal). Independent sampling of the number of triggers and partners for the mixed event ensures that the mixed event will have the number of pairs in only the combinatoric part of real events. If they were drawn non-independently then mixed events would on average contain the same number of pairs as signal events. Clearly, using this as the background normalization would lead to the average remaining partners, the signal, being zero.

The second method is to calculate the background level from the average number of partner particles per event. No event mixing is necessary (mixed pairs are still needed to get the acceptance correction). The mixed event normalization for the previous method is:

$$\langle triggers_i \rangle \langle partners_i \rangle N_{events,i}$$

where $\langle triggers_i \rangle$ and $\langle partners_i \rangle$ are the average number of triggers and partners per event and $N_{events,i}$ are the total number of events in the bin i. Normalizing by the total number of triggers gives:

$$\frac{\langle triggers_i \rangle \langle partners_i \rangle N_{events,i}}{N_{triggers}} = \frac{N_{triggers} \langle partners \rangle}{N_{triggers}} \quad (3.6)$$

$$= \langle partners \rangle \quad (3.7)$$

Since the final measurement is normalized by the total number of triggers the

combinatoric background normalization is simply:

$$\int_0^{\pi} n_{comb,i} d\Delta\phi = \langle partners_i \rangle. \tag{3.8}$$

Ideally, correctly both methods are equivalent. In practice since the first method relies on the event mixer (a random number generator) to get the normalization correct and the second method relies only on the data being analyzed, the second method is preferable and computationally less time consuming. The number of mixed pairs required to get the normalization correct in the first method is much greater than is required for small statistical errors on the acceptance correction. The first method essentially re-measures $\langle partners \rangle$ by mixing events. The Run 2 and 3 analyses [47] use the first method. An additional systematic error on the normalization then results from the variation in normalization for different numbers of mixed events per real event (see Section 4.7.2). The Run 4 analysis uses the second method.

Chapter 4

Data Analysis

The data analyzed in this thesis come from three years of RHIC operations: Run 2, Run 3 and Run 4. The Run 2 data provides the first full energy, $\sqrt{s_{NN}}$=200GeV, Au+Au collisions. The Run 3 data are d+Au and p+p collisions at $\sqrt{s_{NN}}$=200GeV which provide a baseline for comparison with Au+Au measurements. The Run 4 has a high statistics Au+Au dataset at $\sqrt{s_{NN}}$=200GeV. The PHENIX detector configuration for the Run 2 and Run 3 datasets was very similar and the data were analyzed at the same time. Consequently the analysis procedures and corrections are similar. The Run 4 data were analyzed after the publication of the results from the previous data. The are some improvements to the analysis methods and some changes in the PHENIX detector setup, most notably the increased magnetic field strength in the central region. The basic strategy of the analysis is the same for all three Runs and the physics results are directly comparable.

For the remainder of this work "Run" refers to a year of RHIC operations and "run" refers to a short period of PHENIX data taking (typically no more

than an hour) for which the detector and beam conditions are very stable.

4.1 Event Selection

The event mixing technique used works under the assumption that the underlying detector acceptance is constant throughout the events from which particles used in the mixing are drawn. Non-uniformities in the acceptance can create artifacts in the mixed event $\Delta\phi$ distributions which are not present in the real event distributions. The jet signals under investigation are small and these artifacts can alter the measurement.

The PHENIX acceptance does, however, change with time. The primary source of these changes are trips in the high voltage supplies in the drift chambers and pad chambers. This causes a localized region of the detector to not have any recorded tracks until the high voltage is reset, typically at the end of a run.

If the pair rate per event were high it would be possible to create mixed pairs from events which were recorded within the same run, essentially eliminating any time variation. In the current measurement, the pair rate is very low due to the small acceptance of the TOF and the relatively high p_T of the trigger particles. Consequently, we have taken advantage of the fact that runs near in time tend to have similar acceptance.

4.1.1 Run by Run Drift Chamber QA in Runs 2 & 3

The data groups used in this analysis are based on the number of dead channels in the north and south sides of both the east and west arms of the drift

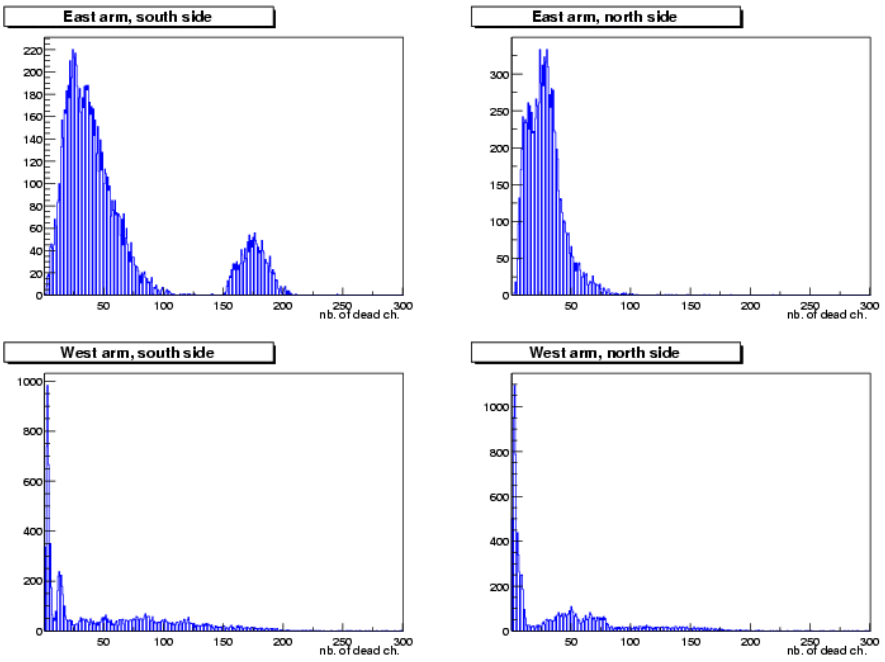

Figure 4.1: Histograms of the number of dead channels in a run for the four sides of the drift chamber.

chambers. Figure 4.1 shows histograms of the number of dead channels per run after subtracting out the channels which were dead for the entire Au+Au data taking period. Most of the data comes from runs which have a small and nearly constant number of dead channels and a small amount of data comes from runs in which larger portions of the detector were off. Each of the four drift chamber sides is assigned a flag based on the number of additional dead channels, see Table 4.1. The sizes of the final run groups used in this analysis are listed in Table 4.2. The d+Au and p+p data sets were too small to divide into run groups; outliers were discarded based on the single particle quality assurance.

DC side	Good Runs (0)	Okay Runs (2)	Okay Runs (3)	Bad Runs (1)
East South	0-130 (84%)	130-255 (14%)		255 < (2%)
East North	0-110 (98%)			110 < (2%)
West South	0-8 (32%)	8-25 (16%)	25-240 (49%)	240 < (3%)
West North	0-15 (51%)	15-85 (34%)	85-210 (13%)	210 < (3%)

Table 4.1: Number of dead channels in each run grouping followed by the fraction of the total data used in that run group. Numbers in parentheses, from 0-3, are the flag used to identify the run group. Runs labeled bad in any side are not used in this analysis.

ES Flag	EN Flag	WS Flag	WN Flag	Number of Events (millions)
0	0	0	0	5.9
0	0	3	2	11.5
0	0	2	0	1.9
0	0	3	3	1.4
2	0	2	0	3.9
2	0	0	0	1.5

Table 4.2: Number of events in each run group used for the Au+Au dataset. Flag combinations not listed were excluded because the total number of events was too small to obtain a stable result.

4.1.2 Run by Run Central Arm QA in Run 4

Events used in this analysis are from Run 4 200GeV Au+Au runs. Only runs with more than 1M events are used; these longer runs are more likely to come from stable detector running. The runs are also required to pass QA for both single particle and pair variables ($\Delta\phi$) to ensure overall detector performance and stability.

Centrality QA The centrality distribution for a run should be flat for events more central than ≈92%. Due to a BBC gain problem some runs from the beginning of Run 4 had to be excluded because their centrality distribution was non-uniform.

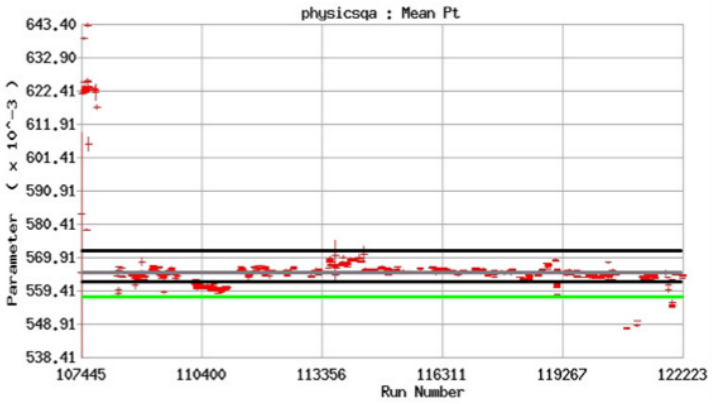

Figure 4.2: Mean momentum of good quality (31 or 63) drift chamber tracks in minimum bias events. The upper black line and the green line show the good region.

Single Particle QA The single particle QA ensures the stability of the central tracking and magnet systems across runs. Runs were excluded based on deviations in mean track p_T (a check on the magnetic field strength), mean number of tracks in each arm (a check on the live area of DC, PC1) and the fraction of high quality tracks which had a match in PC3 (a check on the live area of PC3). Figures 4.2, 4.3 and 4.4 show the mean track p_T , mean number of good tracks, and the match fraction to PC3, respectively. The QA cuts used are:

- $0.558\text{GeV}/c < \langle p_T \rangle < 0.572\text{GeV}/c$
- $0.553 <$ PC3 West hit fraction < 0.567
- $0.499 <$ PC3 East hit fraction < 0.517
- $103 <$ tracks/event < 114

Additional QA was applied for the TOF and EMCal timing systems.

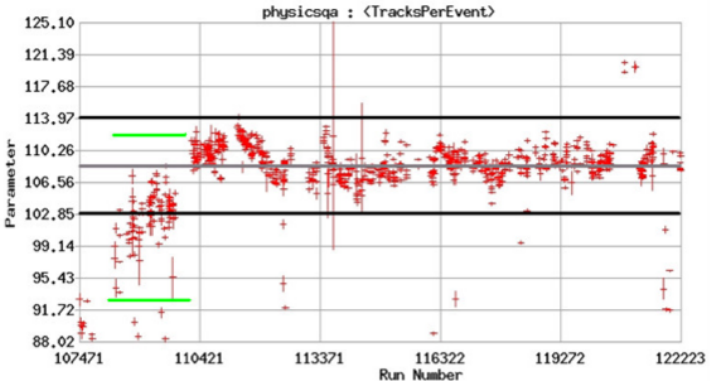

Figure 4.3: Mean number of good quality (31 or 63) drift chamber tracks per minimum bias event as a function of run number. Solid black lines show the good region.

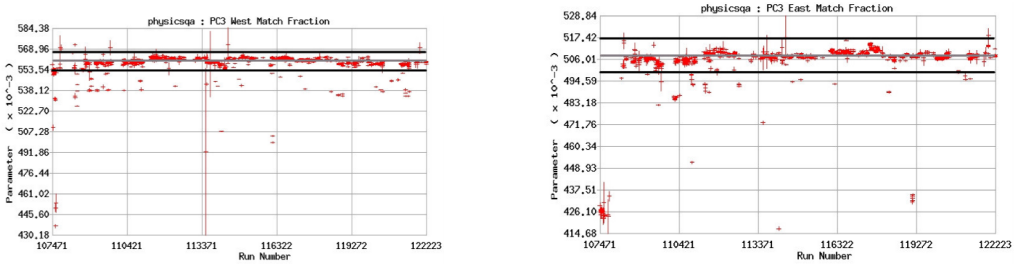

(a) West Arm

(b) East Arm

Figure 4.4: Fraction of good quality drift chamber tracks (quality 31 or 63) which have a 2σ match to a hit in PC3 for the west (left) and east (right) arms as a function of run number. Solid black lines show the good region.

Pair QA Pair QA is done to ensure stable acceptance over runs which are mixed together. Pair QA is based on the work in [53]. Six run groups are defined and shown in Figure 4.5. Mixing is done between events which are both in the same run group and within approximately 3M events of each other; this further minimizes the variation in the pair acceptance between events used for mixing. Mixing in closer proximity is not possible due to the low rates of pairs in this analysis.

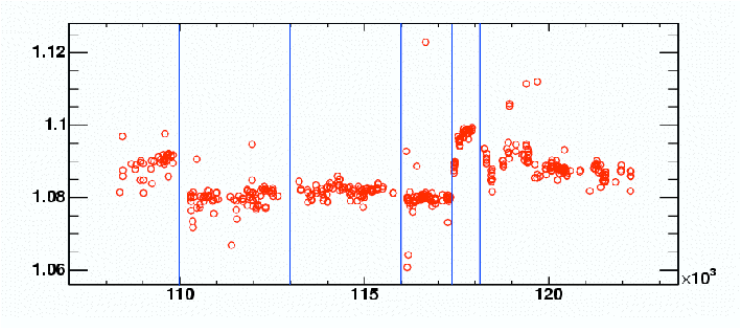

Figure 4.5: Ratio of the number of pairs with $\Delta\phi < \pi/2$ to the number of pairs with $\Delta\phi > \pi/2$ as a function of run number for Run4 200GeV Au+Au. Run group boundaries are shown with vertical lines. Figure is from [53].

4.2 Track Selection

Cuts at the drift chamber and PC3 made on the tracks used in this analysis are placed to ensure as little contamination from background as reasonably possible. Track selection criteria are the same in Runs 2, 3 and 4.

4.2.1 Track Quality Cut

The *quality* of a track in the drift chamber is assigned based on track hits in the X1 and X2 wire layers, the presence and uniqueness of hits in the UV layers, and the presence and uniqueness of track a matching hit in PC1. Tracks used in this analysis are required to have hits in X1, X2, the UV and PC1, but it is possible for the PC1 hit to be ambiguous. In that case the UV information is used to resolve the ambiguity. This cut is applied to both triggers and partners.

4.2.2 Drift Chamber *zed* Cut

Tracks used in this analysis have $|zed| < 75$cm. *zed* is the distance from the center of the interaction region along the beam pipe direction at the drift chamber. The drift chamber extents to $|zed|$=80cm. We exclude the last 5cm to minimize edge effects from particles which are not entirely in the PHENIX acceptance. The cut is a very conservative one, but does not significantly reduce the statistics available. This cut is applied to both triggers and partners.

4.2.3 Matching at PC3

Unidentified charged hadron tracks are matched to hits in PC3. The distributions of the distance of the track projection, based on its position at the drift chamber, and the hit position in PC3 is fit to a Gaussian. The distances are measured in two dimensions: z, along the beam direction and ϕ, around the beam direction. The Gaussian distributions differ for different types of tracks. Low p_T tracks multiple scatter more in the detector material and thus have wider distributions than high momentum tracks. Particles of different charge sign bend in different directions in the residual magnetic field, so the mean values of the distributions will be offset from each other. The distributions are also made differently for the East and West Arms to account for differences in the two separate systems. Matches at 2σ (2.5σ in d+Au and p+p collisions) are required in both dz and $d\phi$ independently. The wider matching cuts in d+Au and p+p are used because of fewer random background hits in PC3 in the smaller system. PC2 is not used here because with the moderate p_T values used in this analysis, the background is not large and PC2 is only located in

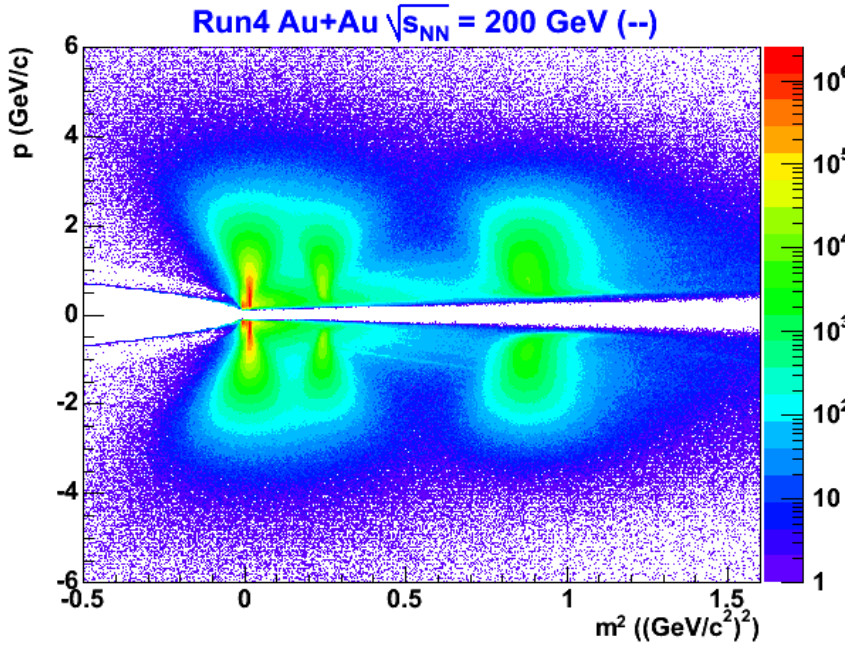

Figure 4.6: m^2 as a function of charge divided by momentum for identified pions, kaons, protons and anti-protons in the TOF in Run 4.

the West Arm making azimuthal correlation analyses impossible because of the small $\Delta\phi$ acceptance.

4.2.4 Matching and PID at the TOF

Tracks are matched in the TOF in the same manner partner tracks are at PC3. Again 2.5σ cuts in both z and ϕ are made for d+Au and p+p and 2σ cuts are made in Au+Au. Tracks identified in the TOF are not matched in PC3 because the additional cut does not reduce the background contribution, but only reduces statistics. A 2σ cut on the difference between the measured m^2 and the expected m^2 is required for identified particles. Figure 4.6 shows the m^2 of identified particles in the TOF for the Run 4 data.

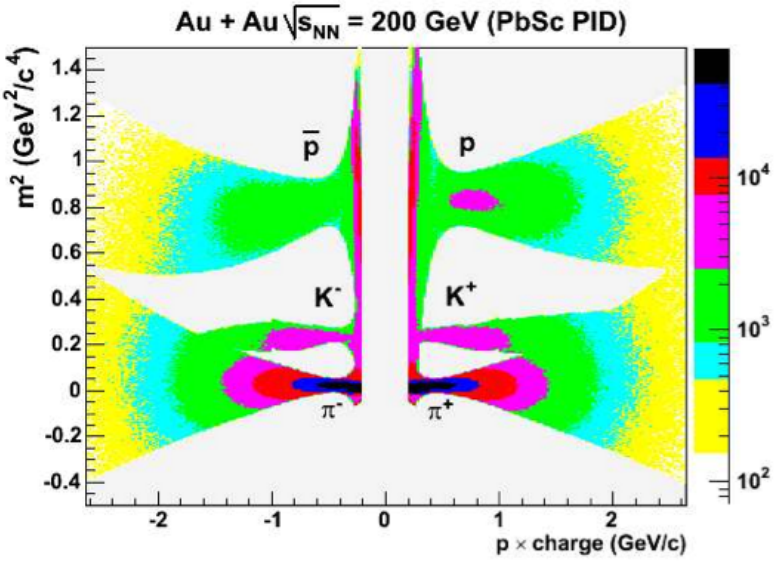

Figure 4.7: m^2 as a function of charge divided by momentum for identified pions, kaons, protons and anti-protons in the EMCal.

4.2.5 Matching and PID at the EMCal

Matching at the EMCal is used in the same manner as in PC3 and the TOF when tracks are identified in the EMCal. An additional match to PC3 is not required. A 2σ cut on the difference between the measured m^2 and the expected m^2 is required for identified particles. Figure 4.7 shows the m^2 of identified particles in the EMCal.

4.3 Pair Selection

Pair cuts are important for jet analyses because the finite resolution of the detector means that real pairs from two tracks close together with have a different efficiency than mixed pairs. The jet signal is small; so real and mixed

events must have the same acceptance. Small differences in the acceptance for real and mixed pairs will obscure the signal. Pair cuts are used to ensure that two tracks which are closer together than the resolution of the detector get removed from both the real and mixed distributions.

Here we evaluate the pair cuts in the approximate momentum ranges used for jet correlation measurements. We look at the distributions of pair variables between a trigger track with p_T >2.5GeV/c and a partner track with p_T >1.0GeV/c. Tracks were required to have high quality and a 2σ match to an outer detector (in this case PC3 instead of the TOF and EMCal because PC3 has larger acceptance), as is required in the final analysis.

4.3.1 Pair Cuts at the Drift Chamber

The drift chamber variables for pair cuts are $\Delta\alpha$ and $\Delta\phi$. $\Delta\phi$ is used to reject tracks which are too close together in the drift chamber to both be reconstructed. Tracks which have small $\Delta\alpha$ and $\Delta\phi$ are possibly ghosts, where a single track is reconstructed as two. Figure 4.8 shows the real minus mixed pairs (each distribution is normalized to have the same total integral). Two structures are clearly visible, the deficiency at small $\Delta\phi$ which is independent of $\Delta\alpha$ and an excess which depends on both $\Delta\phi$ and $\Delta\alpha$. The second feature is due to hit sharing and merged hits PC1, as can be seen in Figure 4.9 where tracks with hits close together in PC1 ($R_{PC1} < 7.5cm$, see Section 4.3.2) have been removed and the feature is gone. The deficiency at small $\Delta\phi$ calls for a pair cut of $|\Delta\phi| < 0.008rad$.

A Δzed cut at the drift chamber is not justified because the track *zed*

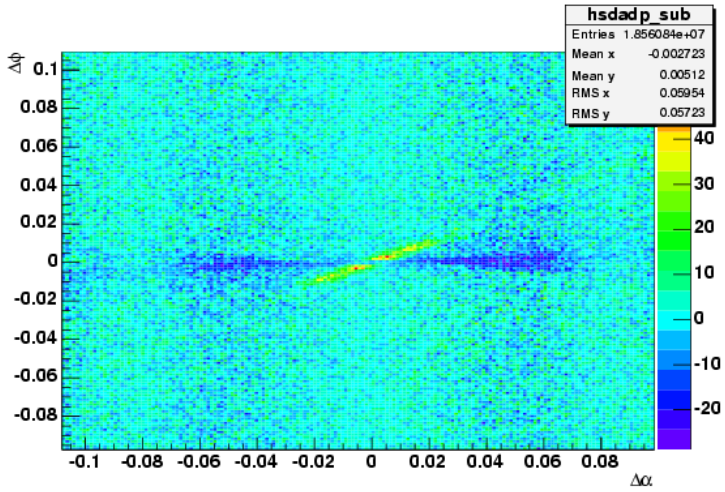

Figure 4.8: $\Delta\phi$ as a function of $\Delta\alpha$ for real events divided by mixed events. The real and mixed events are normalized to have the same total integral.

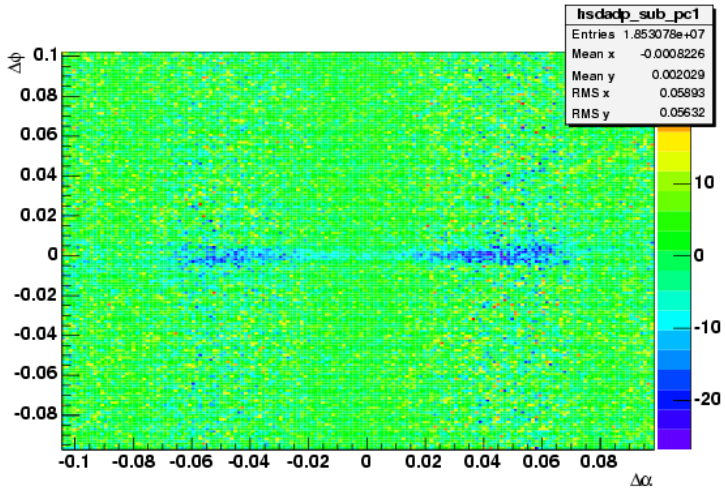

Figure 4.9: $\Delta\phi$ as a function of $\Delta\alpha$ for real events divided by area normalized mixed events with an additional cut on $R_{PC1} < 7.5cm$. The real and mixed events are normalized to have same total integral.

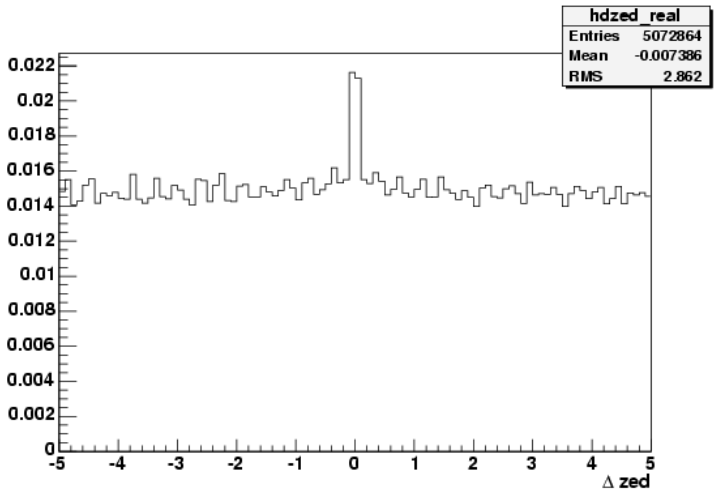

Figure 4.10: Δzed for real events divided by mixed events. No ΔR_{PC1} cut has been made.

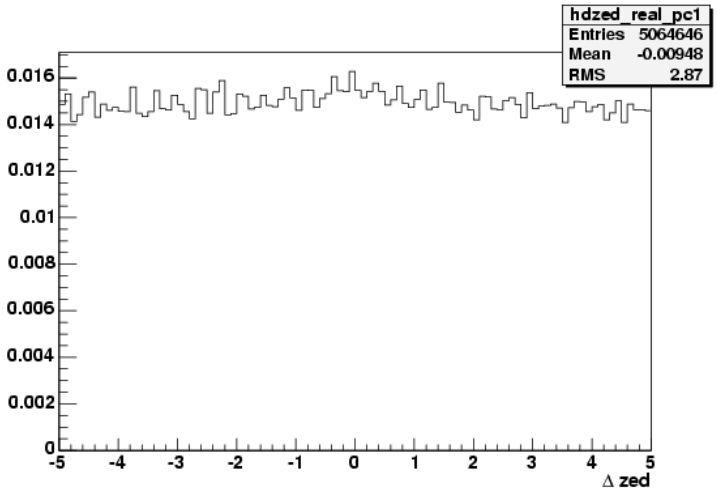

Figure 4.11: Δzed for real events divided by mixed events. A cut on $\Delta R_{PC1} < 7.5cm$ has been made.

information primarily comes from the location of the hit in PC1. Figures 4.10 and 4.11 show that while there is an excess at small Δzed, the cut is not necessary once a cut has been made on R_{PC1} (see Section 4.3.2).

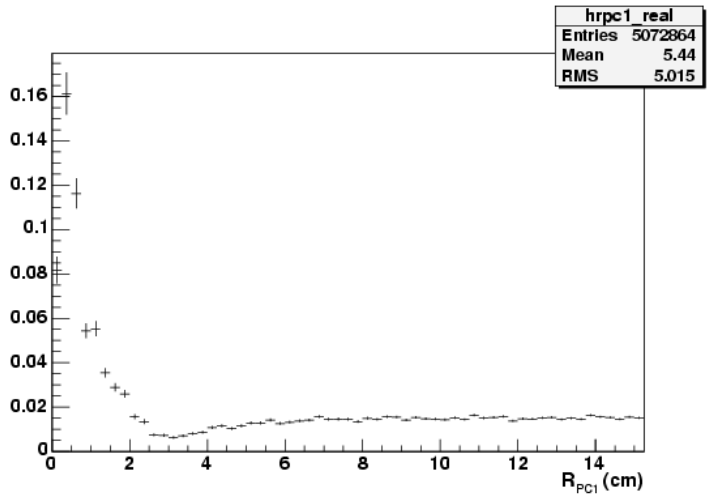

Figure 4.12: R_{PC1} distribution for real events divided by mixed events

4.3.2 Pair Cuts at PC1

The pair cut variable used for PC1 is R_{PC1} which is the distance between the hit projections of the two tracks in PC1 (the actual hit locations are not kept in the reconstructed data files). Figure 4.12 shows R_{PC1} for the real events divided by the mixed events showing a deficiency in real events for close PC1 hits. Based on this figure, the R_{PC1} cut should be at 6cm.

4.3.3 Pair Cut Summary

We find that pairs of charged particles for jet correlations at intermediate p_T should be rejected if:

- $|\Delta\phi| < 0.008 rad$
- $R_{PC1} < 6.0 cm$

In the Run 2 & 3 analyses slightly larger pair cuts were used. This is because the pair cuts were evaluated at lower p_T due to insufficient statistics.

These pair cuts are:

- $|\Delta\phi| < 0.008 rad$
- $R_{PC1} < 7.5 cm$

4.3.4 Effects of Pair Cuts on Background Normalization

The foreground pairs lost to pair cuts must be accounted for in the background normalization. Approximately 0.6% of all foreground pairs are rejected because of the pair cuts, most from the $\Delta\phi$ cut at the drift chamber. In the Run 2 and 3 analysis this effect was not taken into account. In the Run 4 analysis the $\langle partners \rangle$ was reduced to account for this.

4.4 Mixed Pair Generation

Mixing is done in 5cm event z vertex bins and in 5% centrality bins for the Au+Au (no centrality selection is done for the d+Au and p+p data sets). It is necessary to mix in small bins in the vertex in order to keep the overall detector acceptance nearly constant. Mixing in small centrality bins is done in order to minimize the effects of multiplicity correlations. Multiplicity correlations cause the apparent combinatoric background level to rise in a way that is not measured in the mixed events; mixed events contain only the uncorrelated combinatoric background. Remaining multiplicity correlations which cannot be eliminated by binning finer in centrality will be discussed in the Section 4.5.3.

The number of events mixed per real event is chosen to minimize the statistical uncertainty coming from the acceptance correction and absolute normalization (in Run 2 and 3 analyses only). Because central events have an overall greater number of particles there is a greater chance to get a combinatoric pair. Therefore for central events fewer events are mixed for every real event. In more peripheral events there is obviously a much smaller chance to get pairs and therefore many more events must be tried to create a large sample of pairs. The reason the fraction of possible pairs actually used is low because the vast majority of generated mixed events contain no pairs. Triggers and partners are added to the mixing lists regardless of whether or not there actually is a pair in their original event (e.g. if a real event has one partner particle and no triggers there are no pairs in the event, but the partner is available for making mixed events). The accurate counting of events is necessary to get the absolute normalization of the conditional yield correct. The absolute normalization relies on a large absolute number of mixed events, so in the smaller run groups more mixed events per real event are needed. Table 4.3 shows the number of mixed events per real event as a function of centrality, trigger type and run group. While the number of mixed events per real event is quite large for the more peripheral centrality bins, the fact that most events do not contain any pairs protects against oversampling. The shape of the final distribution only depends on the shape of the mixed distribution.

centrality	E00W00	E00W32	E00W20	E00W33	E20W20	E20W00
trigger baryons						
0-10%	40	24	160	160	80	160
10-20%	80	32	320	320	160	320
20-40%	480	320	1600	1600	800	1600
40-60%	4800	4800	10000	10000	10000	10000
60-70%	10000	10000	10000	10000	10000	10000
trigger mesons						
0-10%	24	16	80	80	40	80
10-20%	40	24	160	160	80	160
20-40%	160	160	800	800	400	800
40-60%	2400	800	10000	10000	10000	10000
60-70%	10000	10000	10000	10000	10000	10000

Table 4.3: Number of mixed events per real event for different centrality, trigger types and run groups in the Run 2 analysis. Checks were done to ensure we are not exhausting the possible unique pairs.

4.4.1 Edge Effects in Mixed Pairs in Run4

In the Run 4 analysis the mixed events did not properly reproduce the shape of the pair acceptance in the region around $\Delta\phi = \pi/2$ where the acceptance is small. It is believed that this is due to the higher magnetic field in Run 4. The higher field bends particles more; positive and negative particles are bent into and out of the acceptance in different places. The number of pairs as a function of their charge combination are different in real and mixed pairs in this region (see Table 4.4). Points with $1.26 < \Delta\phi < 2.04$rad were removed because of this problem. This is outside the region used for integrating the conditional yield measurements so the results are not changed in any way.

4.5 Corrections

4.5.1 Efficiency and Occupancy Corrections in Run2 & 3

Detector Efficiency Correction

Single Particle Monte Carlo Correction for Run 2 and Run 3 Analyses The acceptance correction equalized the probability of finding a track anywhere in $\Delta\phi$. The efficiency correction corrects for the cases when a partner is not reconstructed, independent of the trigger location. This includes detector dead areas, track reconstruction efficiency and the losses due to matching cuts at PC3. This correction comes from a Monte Carlo simulation of single particles, $\pi^{\pm}$, $K^{\pm}$, p and $\bar{p}$ separately, passed through a GEANT based simulation of the PHENIX detector. This Monte Carlo has also been used to correct charged hadron spectra in Au+Au, d+Au and p+p collisions [25, 39, 54]. Those analyses, to reduce background at high p_T , required tracks to have $|zed| < 40cm$, the distance along the beam direction from the center of the interaction region. In the present analysis we do not use high p_T tracks so we can allow $|zed| < 75cm$. Therefore we decrease the correction factor by 40/75. The correction function is multiplied by 0.7 to undo the extrapolation from the PHENIX $\Delta\eta$ acceptance of $|\Delta\eta| < 0.7$ to ± 0.5 in η that is made in the single particle analyses under the assumption that particle production is flat in η for $|\eta| <$0.5; for this pair analysis any extrapolation beyond the measured $\Delta\eta$ acceptance must involve an assumption about the shape of the signal, which we do not want to make. The correction functions are determined separately for

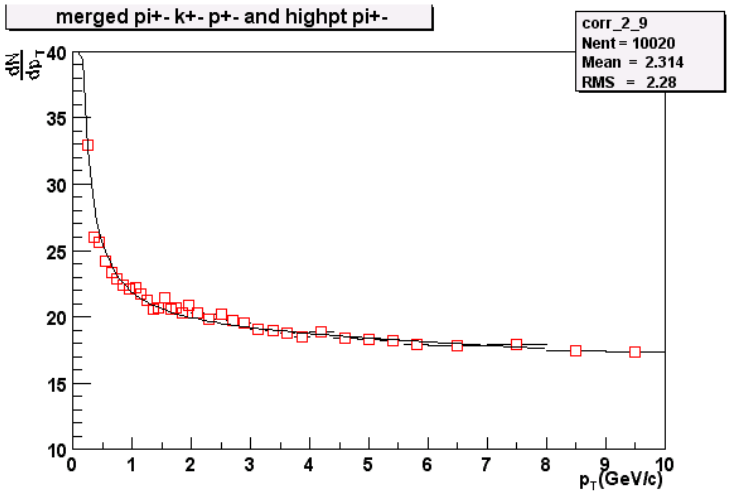

Figure 4.13: Correction function for the East Arm in d+Au

the East and West Arms of PHENIX; Figures 4.13 and 4.14 show the correction as a function of p_T . In order to smooth the statistical variation between the bins in the correction function a fit is used; the fit function is:

$$CF(p_T) = \frac{A}{p_T} + B + Cp_T + Dp_T^2$$

The fit parameters are given in Table 4.5

The East and West Arms are independent systems which have different efficiency, leading to an unequal number of tracks measured in each arm. This unequal performance is due to differing live areas in the drift chamber and the outer detectors and can change as a function of collision system. For the Run 2 Au+Au runs included in this analysis 53.4% of the partner tracks were measured in the East Arm and 46.6% were measured in the West Arm. For the d+Au runs 48.5% of the tracks are in the East Arm and 51.5% of the tracks are in the West Arm. For the p+p run 49.5% of the tracks are in the East

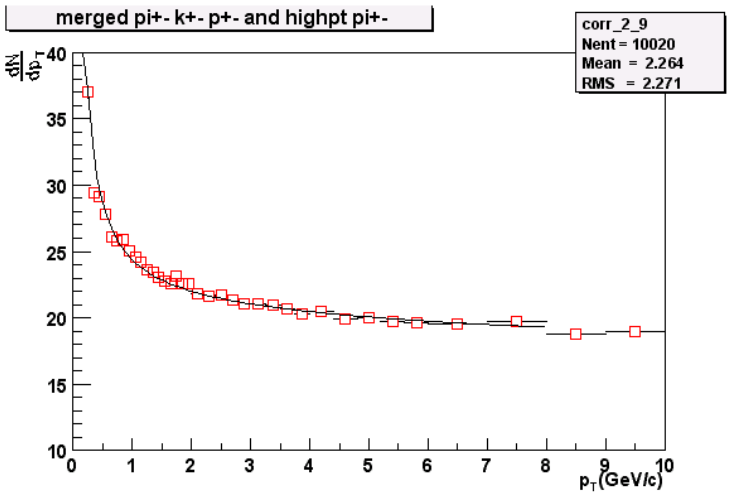

Figure 4.14: Correction function for the West Arm in d+Au

Arm and 50.5% of the tracks are in the West Arm. In this analysis, tracks are no longer distinguished by which arm they hit so the final correction factor is:

$$F = (e_{East}x_{East} + e_{West}x_{West})N_{MC}$$

where x_{East} (x_{West}) are the fraction of tracks that hit the East (West) Arm and e_{East} and e_{West} are the appropriate efficiency values for p_T and collision system listed in Table 4.6.

There is an additional overall scaling factor, N_{MC}, to account for the differences between the Monte Carlo detector performance and the real detector performance. This number is close to 1 because the simulation describes the data well. For Au+Au $N_{MC} = 0.98$ and for d+Au and p+p $N_{MC} = 1.06$ (the performance for d+Au and p+p were assessed separately). F is the final multiplicative centrality independent correction to the angle integrated conditional yields. An additional 4% correction is applied in Au+Au to account for

the tighter matching cuts. Values for F, e_{East}, and e_{West} are shown in Table 4.6 for the p_T ranges used in this analysis.

Detector Occupancy Correction The occupancy correction corrects for the centrality dependent detector occupancy effects. It has been measured to be p_T independent [25]. In d+Au, due to low detector occupancy, this correction is taken to be 1. In Au+Au the correction was evaluated by embedding simulated tracks into real events and evaluating the probability to reconstruct it within the underlying event. The values of this correction are the reciprocals of the tracking efficiencies shown in Table 4.7 [25].

4.5.2 Efficiency and Occupancy Corrections in Run4

The efficiency corrections for the Run 4 analysis are calculated by comparing the measured raw partner rates per event with the integral of the relevant single particle p_T spectra published in [25, 27]. This approach was used because a Monte Carlo simulation and embedding study had not yet been done for the Run 4 experimental setup. This approach has been used in other PHENIX analyses [48] and is much less time consuming than a Monte Carlo simulation. The systematic errors are similar in both methods, but this approach relies on single particle spectra analyses and the results are not independent.

Since the p_T binning of the single particle spectra is not the same as the binning used in this analysis for the partner particles, a fit to the single particle spectrum in the relevant p_T range is used to integrate the yield. The fit function is:

$$\frac{1}{p_T N_{evts}} \frac{1}{2\pi} \frac{d^2N}{dp_T d\eta} = \frac{A}{(B + p_T)^C} \tag{4.1}$$

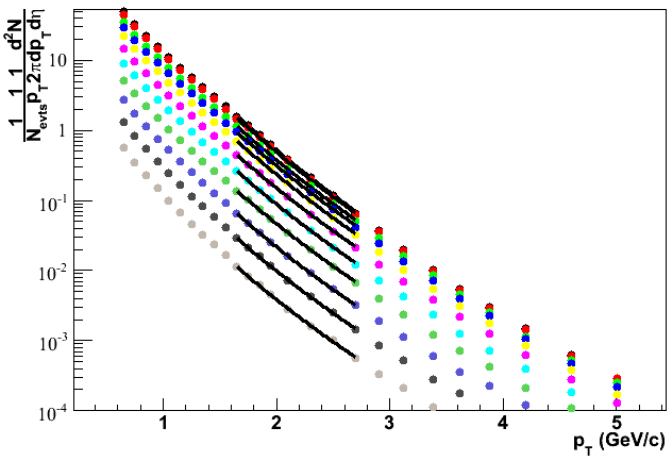

Figure 4.15: The charged hadron spectra for as measured in Au+Au collisions from [25] for several central selections: 0-5%, 0-10%, 10-15%, 15-20%, 20-30%, 30-40%, 40-50%, 50-60%, 60-70%, 70-80% and 80-92%. Fits shown are for 1.7d< p_T <2.5GeV/c .

A separate fit is done for each partner p_T range to minimize errors due to the fit shape. Figures 4.15 and 4.16 show the fits and the ratios of data to the fit for the partner p_T range of 1.7< p_T <2.5GeV/c .

To get the number of corrected charged particles which hit the PHENIX η acceptance we take the integral:

$$2\int_{p_{T,low}}^{p_{T,high}} 2\pi\Delta\eta \frac{Ap_T}{(B+p_T)^C} dp_T \tag{4.2}$$

where A, B and C are the parameters fit in Equation. 4.1, $p_{T,low}$ and $p_{T,high}$ are the low and high p_T edges of the partner p_T bin of interest, respectively and $\Delta\eta$ is the PHENIX $|\Delta\eta| < 0.7$ acceptance. The additional factor of 2 is because [25] reports the spectra as $\frac{h^+ + h^-}{2}$. Table 4.8 lists the results of the integration for 1.7< p_T <2.5GeV/c .

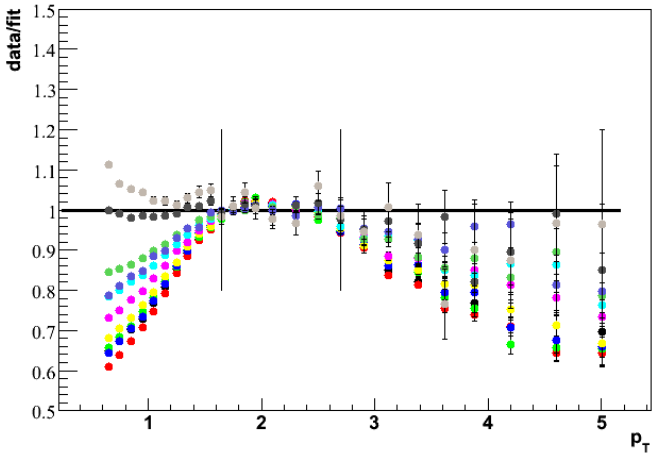

Figure 4.16: Ratio of data to the fits shown in Figure4.15. The vertical lines indicate the region over which the integral is taken: 1.7< p_T <2.5GeV/c . The color code is the same as in Figure 4.15.

Computation of the final efficiency correction values used in the analysis is done by combining the corrections for the wide centrality bins in [25] weighted by the number of trigger particles in the bin. The trigger particle weighting is how centrality bins are combined for the $\frac{1}{N_{trig}}\frac{dN}{dN}d\Delta\phi$ distributions. These efficiency corrections for charged hadron partners for the centrality bins used in this analysis are shown in Table 4.9.

Efficiency Correction for Identified Partner Particles For the identified baryon and meson partners the single particle spectra from [27] are used and fit in the same manner as the unidentified particle spectra above. The fits to the data and the ratios of the data to the fits are shown in Figures 4.17, 4.18 and 4.19 for $\pi^{\pm}$, $K^{\pm}$ and protons and anti-protons, respectively with 1.7< p_T <2.5GeV/c . $\pi^{\pm}$ and $K^{\pm}$ spectra are added for the meson partners and p and $\bar{p}$ spectra are added for the baryon partners. Additionally, the

baryon partners include contributions from decays of Λ and $\bar{\Lambda}$ baryons which are measured as protons and anti-protons in PHENIX because of their short lifetime. The spectra in [27] have been corrected for this feed down. For the efficiency correction in this analysis we need to remove the feed down correction as we are measuring Λ and $\bar{\Lambda}$ partners as well. Figure 4.22 shows the ratios Λ to measured protons and $\bar{\Lambda}$ to measured $\bar{p}$ as a function of p_T , $\delta_{feed}(p_T)$. The p_T dependent correction factor applied to the proton and $\bar{p}$ spectra to remove the Λ and $\bar{\Lambda}$ contribution in [27] is:

$$C_{feed}(j, p_T) = 1 - \delta_{feed}(j, p_T) \tag{4.3}$$

where $j = p, \bar{p}$. The inverse of this correction, which is applied to increase the proton and $\bar{p}$ spectra in the present analysis is:

$$\frac{1}{1 - \delta_{feed}(j, p_T)}. \tag{4.4}$$

The integral calculated to get the yield for the various particles is the same as Equation. 4.2 except for the replacement of $\Delta\eta$ by Δy since the mass of the particles is known,

$$2\int_{p_{T,low}}^{p_{T,high}} 2\pi\Delta y \frac{Ap_T}{(B + p_T)^C} dp_T \tag{4.5}$$

The PHENIX rapidity acceptance varies with the mass of the particle and is calculated for each particle type based on the $\langle p_T \rangle$ of the partner p_T bin.

The efficiency corrections for baryon and meson partners are shown in Table 4.10. The efficiency corrections for proton and anti-proton partners are

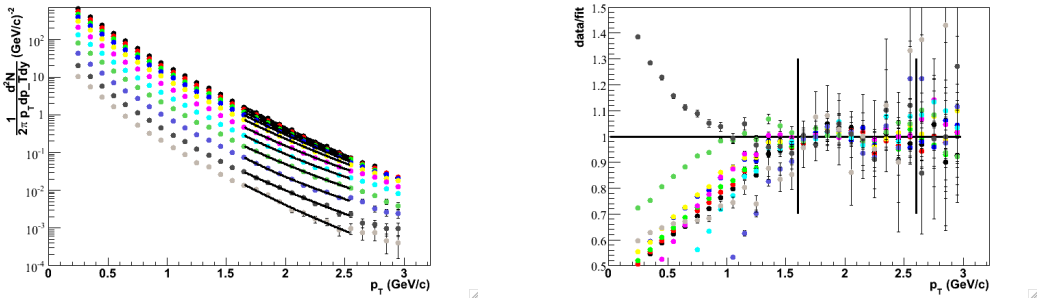

(a) (b)

Figure 4.17: Left: Spectra of combined $\pi^{\pm}$ from [27] for the centrality bins: 0-5% (black), 5-10% (red), 10-20% (green), 20-30% (blue), 30-40% (purple), 40-50% (teal), 50-60% (sage), 60-70% (light blue), 70-80% (grey) and 80-92% (light grey). The fits are also shown over the range fitted to. Errors are statistical only. Right: Ratios of the data to the fit. Vertical bars mark the fit range; the color code is the same as the left figure.

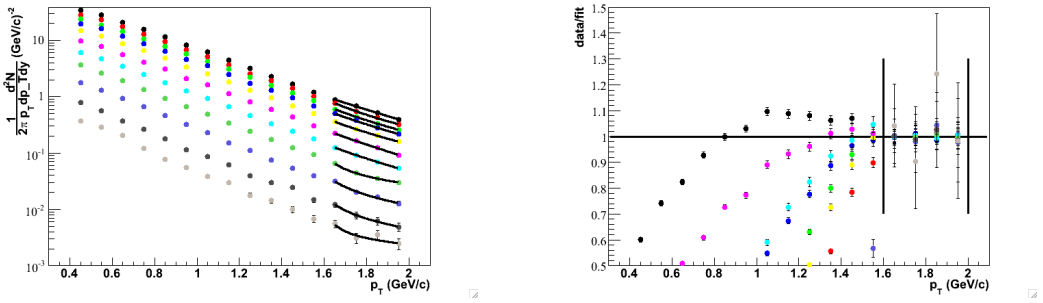

(a) (b)

Figure 4.18: Left: Spectra of combined $K^{\pm}$ from [27] for the centrality bins: 0-5% (black), 5-10% (red), 10-20% (green), 20-30% (blue), 30-40% (purple), 40-50% (teal), 50-60% (sage), 60-70% (light blue), 70-80% (grey) and 80-92% (light grey). The fits are also shown over the range fitted to. Errors are statistical only. Right: Ratios of the data to the fit. Vertical bars mark the fit range; the color code is the same as the left figure.

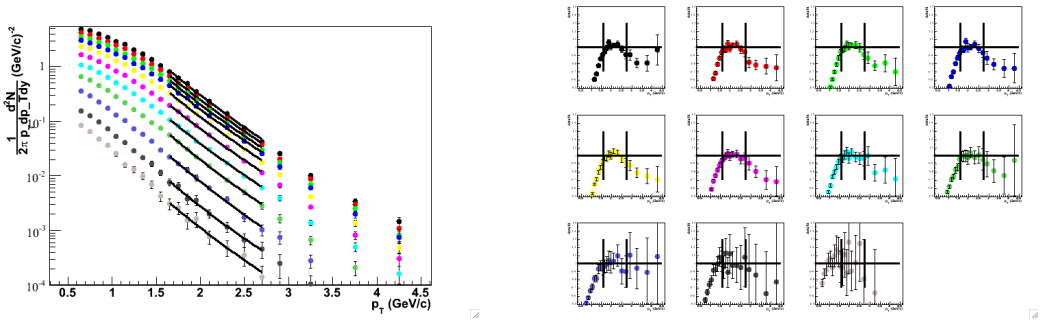

(a) (b)

Figure 4.19: Left: Spectra of combined p and $\bar{p}$ from [27] for the centrality bins: 0-5% (black), 5-10% (red), 10-20% (green), 20-30% (blue), 30-40% (purple), 40-50% (teal), 50-60% (sage), 60-70% (light blue), 70-80% (grey) and 80-92% (light grey). The fits are also shown over the range fitted to. Errors are statistical only. Right: Ratios of the data to the fit. Vertical bars mark the fit range; the color code is the same as the left figure.

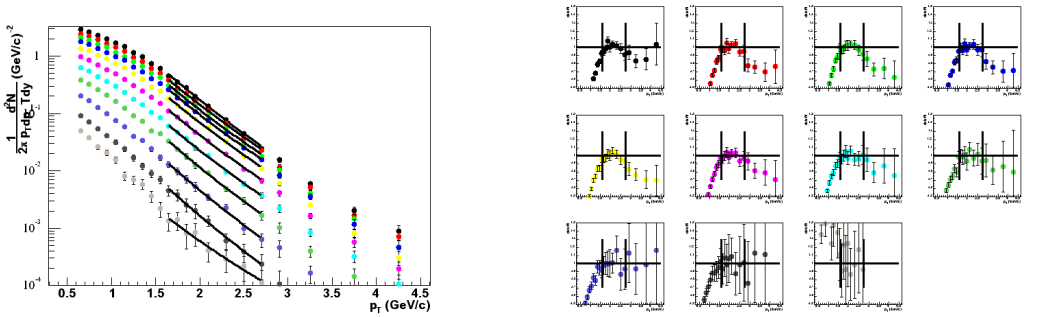

(a) (b)

Figure 4.20: Left: Spectra of protons (anti-protons are not included) from [27] for the centrality bins: 0-5% (black), 5-10% (red), 10-20% (green), 20-30% (blue), 30-40% (purple), 40-50% (teal), 50-60% (sage), 60-70% (light blue), 70-80% (grey) and 80-92% (light grey). The fits are also shown over the range fitted to. Errors are statistical only. Right: Ratios of the data to the fit. Vertical bars mark the fit range; the color code is the same as the left figure.

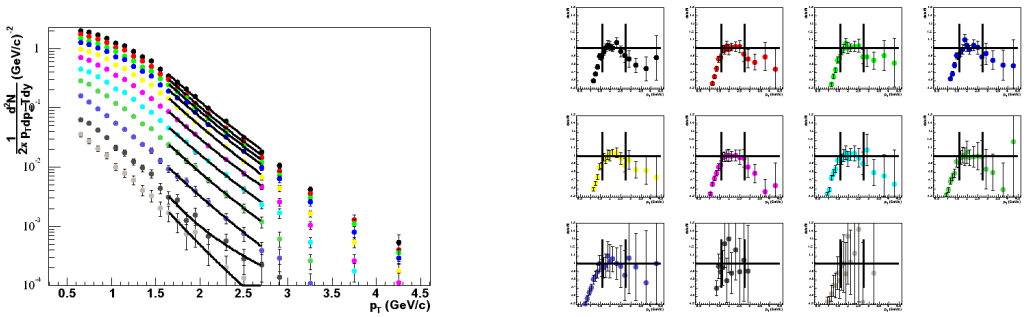

(a) (b)

Figure 4.21: Left: Spectra of anti-protons (protons are not included) from [27] for the centrality bins: 0-5% (black), 5-10% (red), 10-20% (green), 20-30% (blue), 30-40% (purple), 40-50% (teal), 50-60% (sage), 60-70% (light blue), 70-80% (grey) and 80-92% (light grey). The fits are also shown over the range fitted to. Errors are statistical only. Right: Ratios of the data to the fit. Vertical bars mark the fit range; the color code is the same as the left figure.

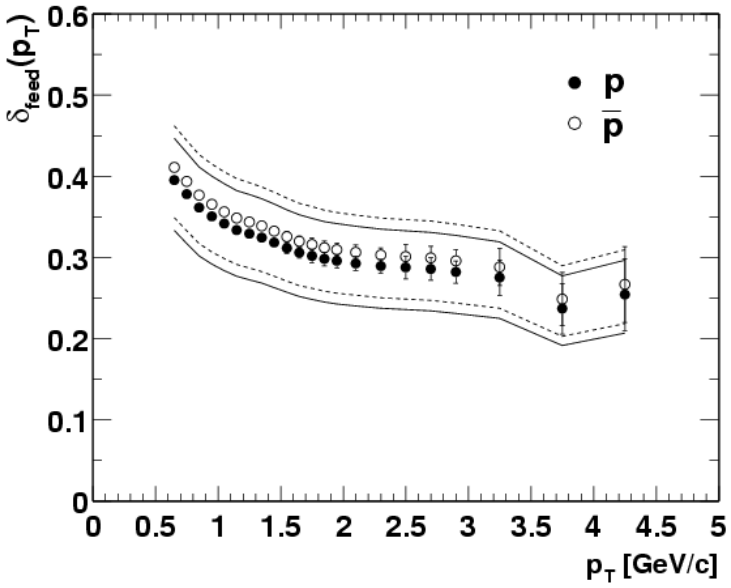

Figure 4.22: Fractional contribution of protons ($\bar{p}$) from Λ ($\bar{\Lambda}$) decays in all measured protons ($\bar{p}$), δ_{feed} as a function of p_T . The solid (dashed) lines are the systematic errors for protons ($\bar{p}$) and the error bars are the statistical errors. Figure is taken from [27].

shown in Table 4.11.

4.5.3 Centrality Bias Correction

Multiplicity correlations are a real source of unwanted correlations which we measure. They occur because of the finite size of the centrality bins used for mixing and fluctuations of the particle multiplicity for a given centrality. The more central events within a bin have, on average, a higher number of trigger partner pairs than those from the lower centrality part of the bin due to the larger overall multiplicity. Likewise, events which have multiplicity higher than the average event for that centrality will have more pairs. These pairs occur only because of the overall event multiplicity and have nothing to do with jets, but they do have a real correlation so they are not included in the calculated combinatoric background.

These correlations increase with the width of the centrality bin used for mixing as the fluctuations from the average multiplicity become larger. Mixing in fine centrality bins is done to minimize the importance of these correlations, but since the jet signal we wish to measure is small compared to the combinatoric background level in central Au+Au collisions, the effects of these correlations must be added to the final combinatoric background level. We have found that using centrality bins narrower than the 5% bins currently mixed does not make a measurable difference, indicating that we are already using bins close to the resolution of the PHENIX centrality measurement.

To remove the multiplicity correlations, we use what we know from the Glauber model and the normalization of background to determine a parame-

ter, ξ, which is the ratio of what we should have subtracted, removing the effects of multiplicity correlations, to what the $\langle triggers \rangle \langle partners \rangle$ background normalization scheme determines the background level to be. Since multiplicity correlations increase the real events in a way that is not measured in the mixed events, ξ is greater than one. The effects of multiplicity correlations are large when either ξ or the combinatoric background level is large.

The value of ξ depends on the centrality dependence of the number of trigger and partner particles per event; a strong dependence of the multiplicity on centrality leads to larger multiplicity correlations because there is more of a difference between the central and peripheral edges of the centrality bin. The centrality dependence is quantified by fitting the single particle yields at a given p_T, the mean trigger or partner p_T, as a function of a centrality measure, N_{part} or N_{coll}. Other centrality measures such as the centrality itself or the collision impact parameter could have been used. Initially it was thought that the variation in ξ values from using linear N_{part} and N_{coll} scaling of the yields would be small enough that the average of the two ξ values could be used with the two scalings defining the systematic error since the real scaling of the yields at the p_T values used in this analysis with centrality is somewhere in between. However, neither of these scalings described the data well enough to give satisfactory results.

Instead, a reasonable description of the yields as a function of N_{part} and N_{coll} can be obtained with these functional forms:

$$f_{trigger}(N) = A(1 - e^{-BN^{\alpha}}) \tag{4.6}$$

and

$$f_{trigger}(N) = A \arctan(BN^{\alpha}). \tag{4.7}$$

These parameterizations were determined essentially by trial and error. Polynomial functions were tried, but were unsuitable because of unphysical changes in the sign of the second derivative. Also, polynomials would give uncontrolled behavior in the region beyond the data at high and low centralities. In very central collisions the particle yields are not expected to increase dramatically with N_{part} or N_{coll} as the impact parameter approaches zero and the yields certainly do not decrease. Likewise, the functions in Equations 4.6 and 4.7 both increase smoothly toward an asymptote as $N \to \infty$

When this has been fit, we have parameterizations of the yields as a function of centrality for both the trigger and the parter, $f_{trigger}(N)$ and $f_{part}(N)$, where N is either N_{part} or N_{coll}. Triggers (partners) are assumed to be distributed according to a Poisson distribution with a mean of $f_{trigger}(N)$ ($f_{part}(N)$). For each event N is randomly taken from the Glauber distribution of either N_{part} or N_{coll} for each 5% centrality bin in Au+Au (minimum bias in d+Au). In this way pairs whose only correlation is the underlying centrality of the event are created.

Because multiplicity is the only correlation in this simple picture we want to subtract everything; there is no signal. We also know what we would subtract if we blindly applied our $\langle triggers \rangle \langle partners \rangle$ procedure above. The value of ξ is simply the ratio of what we should subtract over what we would subtract

if ξ=1. ξ modifies Equation 3.1 to:

$$J(\Delta\phi) == \frac{1}{\epsilon \sum_i N_i}(\sum_i \frac{dN_{real,i}/d\Delta\phi}{Acc_i(d\Delta\phi)}) - \xi n_{comb,i}(1 + 2v_2^{trigger} v_2^{partner} \cos(2\Delta\phi). \tag{4.8}$$

4.5.4 ξ for Au+Au Analysis

In Au+Au collisions, ξ depends on both the width of the centrality bin mixed in and its mean. Consequently, a separate ξ value must be determined for each centrality bin we mix in. In the most central bins ξ is very close to one and increases with decreasing centrality as the relative effect of multiplicity fluctuations around the mean increases. Though ξ is close to 1 in central collisions, the combinatoric background is also very high in central events so the multiplicity correlations are important and must be included. For the unidentified charged hadron partners, the centrality dependent yields are taken from [25] at the appropriate mean p_T. For the identified leading mesons the yields are taken from [22], π^0 yields only, at $p_T = 2.75GeV$. The pion yields are taken from the neutral pion measurement to reduce the statistical errors. The $\pi^{\pm}$ yields in [27] stop at 3.0GeV and have large errors in the last couple of points. The $K^{\pm}$ which is also included in the leading meson category stops in [27] at 2.0GeV. These are added together to get the meson yields for partners between 1.7< p_T <2.5GeV/c . For the baryon yields the proton and anti-proton spectra in[27] are used to get the single particle spectra.

The values of the fit parameters for the p_T ranges used and plots of the data and fits together can be found in Appendix A.

We have no physics reason to believe that the yields should necessarily

follow either Equation 4.6 or 4.7, but they do fit the data points. There is also no reason to prefer either controlling parameter for the multiplicity correlations, N_{part} or N_{coll}. In light of this we simply treat all four methods of getting ξ equally. The points are placed at the average and the systematic errors are the maximum deviations from the average. Tables B.0.3 through B.12 show the ξ values used in this analysis for Au+Au. There are slightly different ξ values between the Run 2 and Run 4 analyses. In Run 2 the Monte Carlo was stopped by hand when the ξ values looked stable; in Run 4 the Monte Carlo was stopped when the ξ value had changed by less than 0.0001 over 100,000 generated events.

4.5.5 ξ for d+Au Analysis

The d+Au analysis here was done with a single minimum bias centrality bin. The single particle yields in d+Au were fit as a function of centrality using the same procedure as in Au+Au. For the d+Au only the arctan fitting function (Equation 4.7) described the data. Additionally, the π^0 yields could not be fit with either function for an unknown reason. The charged hadron yields were used instead. This is justified because the p/π ratio changes very little with centrality in d+Au and the charged hadrons are primarily $\pi^{\pm}$ [40]. The fit parameters are in Table A.11. The inability to fit some of the yields with one function is not troubling. The variation in ξ comes mainly from switching between fitting as a function of N_{part} and N_{coll} and in d+Au collisions the jet signal to combinatoric background is large making ξ less important. The d+Au values of ξ used are found in Table B.13. Plots of the yields and the fit

functions are found in Tables A.11 though A.16.

4.5.6 Centrality Bias in p+p Collisions

The method used above for determining ξ is not suitable for p+p collisions because $N_{coll} = 1$ and $N_{part} = 2$ in all cases where a collision actually happens. In p+p collisions the absence of a large soft underlying event means the jet signal strongly dominates the combinatoric background making any variation in the background level fairly unimportant. We have taken the effect of multiplicity correlations in p+p collisions to be negligibly small.

4.6 v_2 Measurement

The v_2 values used in this analysis come from [31] which contains measurements of v_2 as a function of p_T , centrality and particle type (protons and anti-protons and separately $\pi^{\pm}$ and $K^{\pm}$). v_2 values are measured by charged particles' orientation with respect to the reaction plane. The reaction plane is measured by the BBC at $3< |\eta| <4$, minimizing the contribution from jets to the reaction plane definition; in order for a jet observed in the central PHENIX arms $|\eta| <0.35$ to influence the reaction plane resolution it must also have at least one particle at pseudo-rapidity covered by the BBC. Such jets are very rare [31]. v_2 is derived from the azimuthal direction of particles in an event:

$$\frac{dN}{d\phi} \propto 1 + 2v_2 \cos(2(\phi - \Phi_{RP}))$$

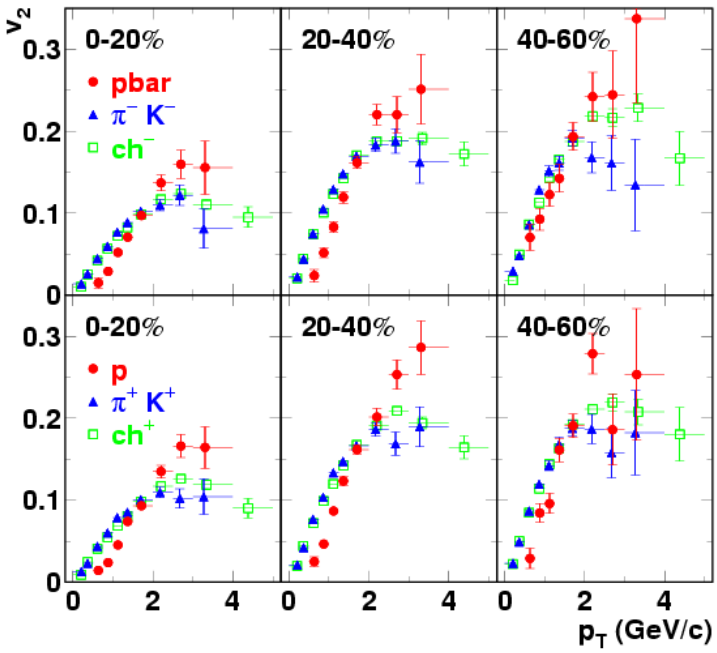

Figure 4.23: v_2 as a function of p_T for identified protons, anti-protons, mesons (π and K) and inclusive charged particles in three centrality selections from [31]. The top panels show negative particles and the bottom panels show positive particles.

where ϕ is the azimuthal direction of a particle and Φ_{RP} is the direction of the reaction plane. If the reaction plane direction is not known, it is possible to measure v_2 with two particle correlations:

$$\frac{dN}{d\Delta\phi} \propto 1 + 2v_2^1 v_2^2 \cos(2\Delta\phi) \tag{4.9}$$

This measurement is obviously sensitive to other correlations between particles, such as the jets measured in this analysis so v_2 values from the reaction plane method are used here.

v_2 as a function of p_T is shown in Figure 4.23 from [31] for identified particles in three centrality selections. The data in Figure 4.23 are shown

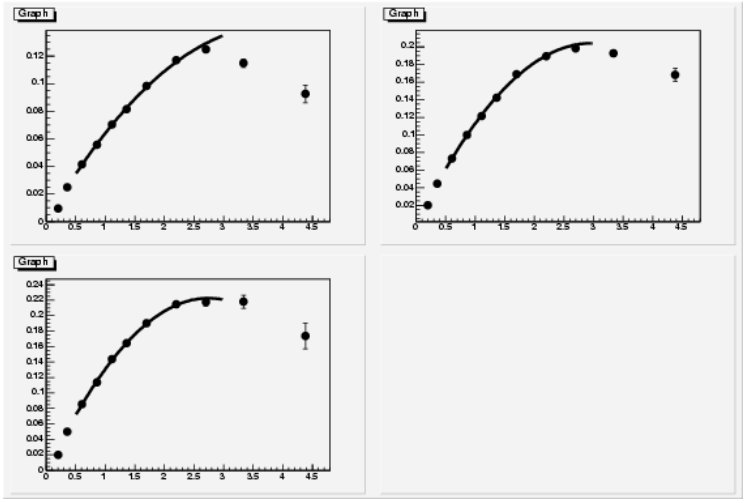

Figure 4.24: Charge averaged v_2 values as a function of p_T for 0-20% (top left), 20-40% (top right) and 40-60% (bottom left) from [31]. The fits are second order polynomials. The fits are only used between 1.0< p_T <2.0GeV/c , so it is unimportant that they do not describe the data outside of this range. Errors shown are statistical.

separately for the different charge signs, but no difference in v_2 values is seen between positive and negative particles. In order to minimize statistical errors all v_2 values are taken from an average of positive and negative values. The p_T binning in the v_2 analysis and the present analysis are not identical. To get the partner v_2 values at the p_T a second order polynomial was fit to the charge averaged v_2 values from Figure 4.23. The fits can be seen in Figures 4.24 (unidentified charged particles), 4.25 (mesons) and 4.26 (baryons). The v_2 values used were the fits evaluated at a given $\langle p_T \rangle$ of the partner. Trigger v_2 values were evaluated at p_T =2.7GeV/c .

The centrality selections used in the v_2 analysis are not identical to those used in this analysis. The most central bin in [31] is 0-20%, which corresponds to three bins in the current analysis: 0-5%, 5-10% and 10-20%. The v_2 values are expected to change significantly in these three bins. Figure 4.27 from

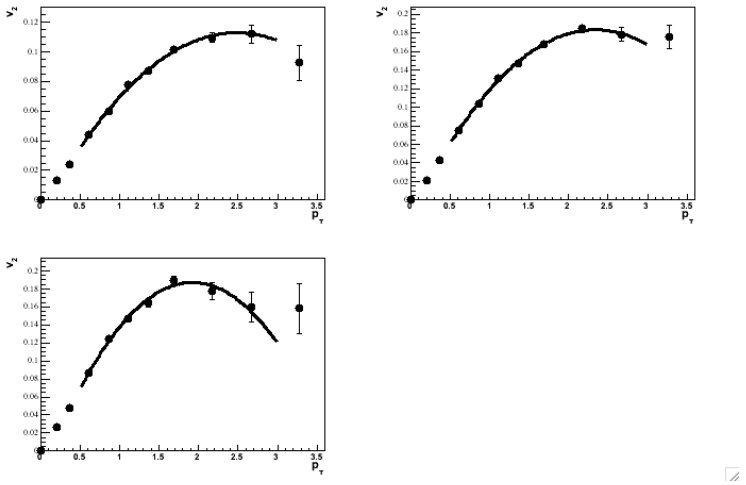

Figure 4.25: Charge averaged v_2 values for $\pi^{\pm}$ and $K^{\pm}$ as a function of p_T for 0-20% (top left), 20-40% (top right) and 40-60% (bottom left) from [31]. The fits are second order polynomials. The fits are only used between 1.0< p_T <2.0GeV/c , so it is unimportant that they do not describe the data outside of this range. Errors shown are statistical.

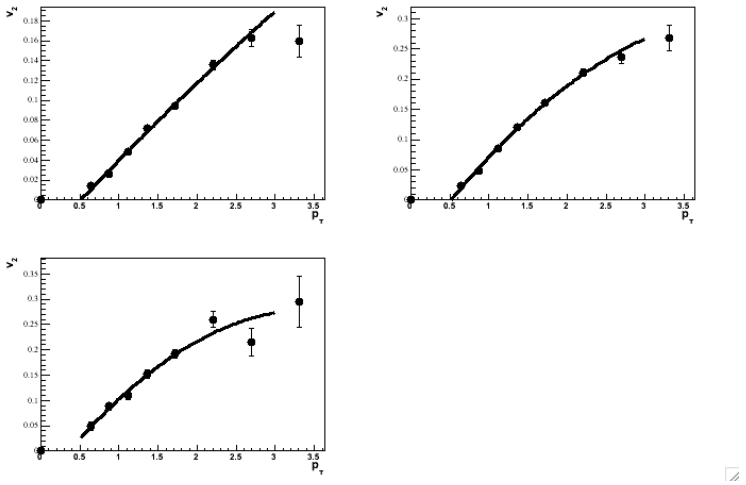

Figure 4.26: Charge averaged v_2 values for p and $\bar{p}$ as a function of p_T for 0-20% (top left), 20-40% (top right) and 40-60% (bottom left) from [31]. The fits are second order polynomials. The fits are only used between 1.0< p_T <2.0GeV/c , so it is unimportant that they do not describe the data outside of this range. Errors shown are statistical.

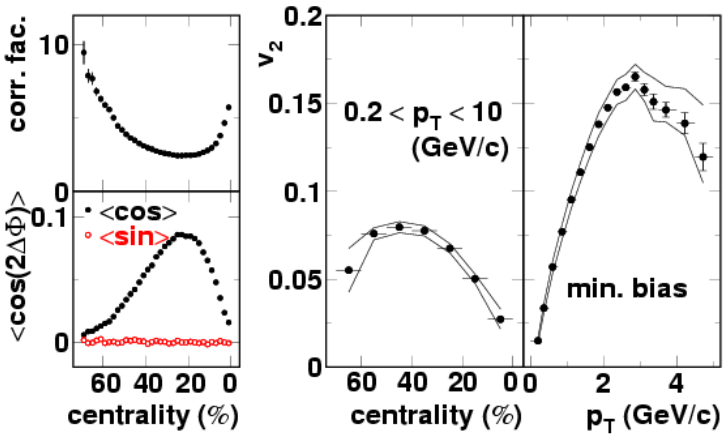

Figure 4.27: The center panel shows p_T integrated v_2 as a function of collision centrality. For collisions more central than 40% an approximate linear dependence on v_2 with centrality is observed.

[31] shows p_T integrated v_2 as a function of centrality for finer centrality bins than exist for the p_T differential measurement. For collision more central than 40% an approximately linear dependence on v_2 with centrality is observed. In the most central collisions, with a zero impact parameter, v_2 should be zero because there is no collision asymmetry. This additional information is used to interpolate for the additional centrality selections needed for this analysis. For the 5-10% and 10-20% centralities the v_2 values are obtained by linear interpolation of the 20-40% and 0-20% centralities. The 0-5% centrality v_2 values are obtained by an average of the interpolation above and one based on the 0-20% values and $v_2(0\%) = 0$. The systematic error on the v_2 values in the most central bin covers both interpolation methods. v_2 values used in all centralities are shown in Tables 4.12 (unidentified charged particles), 4.13 (meson partners), 4.14 (baryon partners) and 4.15 (trigger particles).

4.7 Systematic Errors

4.7.1 Particle Identification

At the high end of the trigger p_T range there is a slight overlap between protons and kaons when a $\pm 2\sigma$ cuts on the proton mass are done. This overlap is no greater than 5% of the total proton triggers also passing the particle identification (PID) cut for kaons. To evaluate the effect of this contamination on the yield, the baryon triggered analysis was run again with $\pm 1\sigma$ cuts on the proton mass for the Run 2 dataset. The changes in the yield come both from PID error we want to measure and from the loss of statistics in going from 2σ to 1σ cuts. Additionally, the change in the conditional yield due to meson contamination will vary with the difference in the true meson and baryon triggered conditional yields. We have used the relative change in the yield as the best estimate of this systematic error and applied it symmetrically to the baryon yield. The changes in the baryon triggered yield with the tighter cuts brought approximately half the centralities closer to the meson triggered points and half further away. For the most peripheral Au+Au bin there are very few triggers and the statistical errors greatly dominate. For that bin we have used the error from the 40-60% bin where there are much more statistics and the error seems reasonable. The PID error for the d+Au is larger, but still smaller than the statistical error on the yield. Due to the larger number of mesons, the baryon contamination of the mesons is negligible. The values of the error are listed in Table 4.16. The same values for this systematic error is applied to the Run 2 and Run 4 datasets.

4.7.2 Mixed Event Generation

To evaluate the systematic error coming from the generation of mixed events, the number of mixed events per real event was varied. Mixing was done with $0.5x$, $1.5x$, and $2x$ mixed events per real event where x is the default mixing factor from Table 4.3. The effect of this change on the near side yield is shown in Figure 4.28 for the partner range 1.7-2.5GeV/c and the values of the error (absolute, maximal extent) are listed in Table 4.17. Since the partner p_T ranges were chosen such that the combinatoric background level is approximately constant the error is evaluated in the partner p_T range 1.7-2.5GeV/c and used for all the other p_T ranges. This error is not included in the p+p analysis since the systematic error includes no subtraction at all.

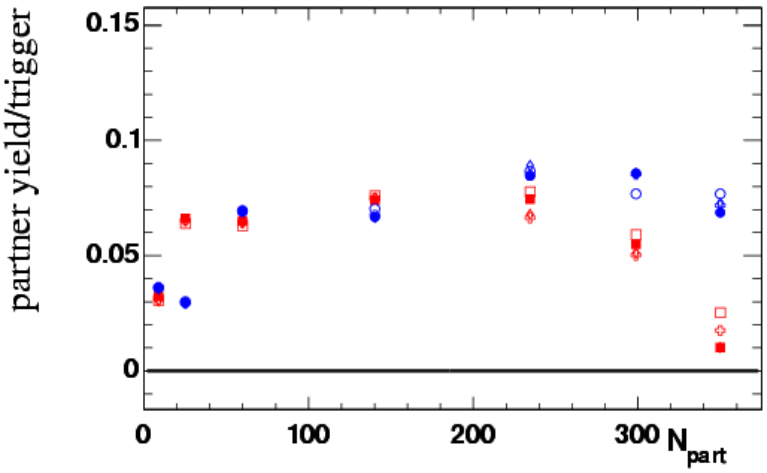

Figure 4.28: Differences in the yields with different numbers of mixed events. Solid points indicate the default mixing value. Blue points are trigger mesons and red points are trigger baryons.

Because the absolute normalization in the Run 4 analysis comes from the

$\langle triggers \rangle \langle partners \rangle$ normalization, not mixed events, this systematic error does not apply.

4.7.3 Efficiency & Occupancy Corrections

Efficiency Correction Systematic Errors in Runs 2 & 3 The systematic error on the centrality independent efficiency correction used in the Run 2 and Run 3 analyses comes primarily from the systematic error on the description of the Monte Carlo matching distributions to PC2 & 3 (10%) and the fit function used to smooth the correction functions in Figures 4.13 and 4.14. An additional 5% uncertainty comes from matching the $\frac{dN}{d\phi}$ distributions from the data to those of the Monte Carlo which is done separately for each collision system. The total systematic error on the efficiency corrections is 12%.

Occupancy Correction Systematic Errors in Run 2 The systematic errors on the occupancy correction come from the variation in the derived values with the changing the matching cuts to PC3. The occupancy corrections are sensitive to the matching cuts used; wider windows increase the occupancy effects in central collisions. The values of the systematic error are shown in Table 4.7. The systematic error on the occupancy correction can move the conditional yields for each centrality independently, but changes the conditional yield for each trigger type together.

Efficiency & Occupancy Correction Systematic Errors in Run 4 Au+Au The efficiency correction systematic error includes the centrality independent normalization of the single particle spectra in [25, 27], the cen-

trality dependent occupancy correction error and the mis-match between the data and the fit used to integrate the spectra in Section 4.5.2. The normalization systematic error of 7.4% moves all $\frac{1}{N_{trig}}\frac{dN}{d\Delta\phi}$ and yield/trigger plots by the same scale factor. The occupancy correction and fit systematics can move the yields independently as a function of centrality, but it cannot change the ratio of the baryon to meson triggered yields at a single centrality. The efficiency corrections used depend only on the type of partner, not the type of trigger.

The occupancy correction errors are shown in Table 4.18 [25]. Though the occupancy correction is not done as a separate step in the Run 4 analysis, the systematic error is separated in [25] in addition to the centrality independent error on the absolute normalization. Since the centrality bins used in this analysis are generally made up of multiple centrality bins from the single particle analyses, the error on the occupancy correction enters independently for each single particle spectra centrality bin which make up the larger centrality bins used here. These systematic errors are taken to be independent of the species of the partner.

The deviation of the fits used from the data is less than 4% for all centralities. This error enters once for each centrality bin in the single particle spectra.

The final centrality dependent systematic errors on the combined efficiency and occupancy corrections are listed in Table 4.19.

4.7.4 Centrality Bias Correction

The systematic error on the centrality bias was discussed in Section 4.5.3. This systematic error is probably correlated with both centrality and particle type, though the correlation is not known.

4.7.5 v_2

The main systematic error on the conditional yields due to the v_2 measurements is the reaction plane resolution. The fractional error on the v_2 measurement due to the reaction plane resolution is given in Table 4.20. This error is the same in both the trigger and partner v_2 values, so it enters twice and is correlated. The remaining systematic error on the v_2 measurements on the conditional yields is the statistical errors on the v_2 values in [31]. These errors are independent both of each other and of the reaction plane resolution errors.

4.7.6 Combinatoric Background Normalization

Here we investigate the possible systematic error due to the background normalization method used: $\langle triggers \rangle \langle partners \rangle$.

Let $\langle n_1 \rangle = \langle triggers \rangle$ and $\langle n_2 \rangle = \langle partners \rangle$. Then, in any event, $n_1 \equiv a + k$ where a is the number of triggers which are part of an observed jet pair and k is the number of triggers which are not part of an observed jet pair (k includes triggers which have a partner that is not detected by PHENIX or is in a different p_T range). Similarly, $n_2 \equiv b + m$ where b is the number of partners which are part of an observed jet pair and m is the number of partners which are not part of an observed jet pair. Experimentally, it is impossible to

distinguish a from k and b from m.

The average number of total pairs in an event is $\langle n_1 n_2 \rangle$. The proper combinatoric background normalization is

$$\langle n_1 n_2 - N_S \rangle = \langle n_1 n_2 \rangle - \langle N_S \rangle$$

where $\langle N_S \rangle$ is the average number of signal pairs in an event. If N_S were directly measurable, the background normalization would be trivial, but N_S is what we want to measure.

$$\begin{aligned} \langle n_1 n_2 \rangle - \langle N_S \rangle &= \langle ab + km + kb + am \rangle - \langle ab \rangle & (4.10) \\ &= \langle ab \rangle + \langle km \rangle + \langle kb \rangle + \langle am \rangle - \langle ab \rangle & (4.11) \\ &= \langle km \rangle + \langle kb \rangle + \langle am \rangle & (4.12) \end{aligned}$$

In this notation the $\langle triggers \rangle \langle partners \rangle$ normalization is:

$$\begin{aligned} \langle n_1 \rangle \langle n_2 \rangle &= (\langle a \rangle + \langle k \rangle)(\langle a \rangle + \langle m \rangle) & (4.13) \\ &= \langle a \rangle \langle b \rangle + \langle k \rangle \langle b \rangle + \langle a \rangle \langle m \rangle + \langle k \rangle \langle m \rangle & (4.14) \end{aligned}$$

We assume all pairs of a, b, k and m are independent except a and b, the jet signal. So:

$$\begin{aligned} \langle a \rangle \langle b \rangle &\neq \langle ab \rangle & (4.15) \\ \langle a \rangle \langle m \rangle &= \langle am \rangle & (4.16) \\ \langle b \rangle \langle k \rangle &= \langle bk \rangle & (4.17) \end{aligned}$$

$$\langle k\rangle\langle m\rangle \;=\; \langle km\rangle \tag{4.18}$$

Thus, $\langle n_1 n_2 - N_S\rangle = \langle n_1\rangle\langle n_2\rangle$ if $\langle a\rangle\langle b\rangle$ is small compared to $\langle k\rangle\langle b\rangle + \langle a\rangle\langle m\rangle + \langle k\rangle\langle m\rangle$. We expect the background normalization in p+p to be most sensitive to this systematic error, since the largest fraction of the total pairs come from jets in the smallest system. It is possible to estimate an upper limit to the error on the background normalization in this case. For a given $5cm$ z-vertex bin in p+p 10132 partners, 2109 triggers and 81 pairs are observed:

$$n_1 \;=\; 2109 \tag{4.19}$$

$$n_2 \;=\; 10132 \tag{4.20}$$

$$N_S \;\leq\; 81 \tag{4.21}$$

Of the 81 pairs some are from jets and some are combinatoric. The normalization is maximally wrong if all pairs are from jets since that maximizes $\langle a\rangle\langle b\rangle$. In that case $a = 81$ and $b = 81$ (events with more than one jet pair are obviously rare enough to be neglected). We then have:

$$k \;= n_1 - a = \;\; 2028 \tag{4.22}$$

$$m \;= n_2 - b = \;\; 10051 \tag{4.23}$$

$$\tag{4.24}$$

The condition for the validity of the background normalization is:

$$\langle a\rangle\langle b\rangle \;\ll\; \langle k\rangle\langle m\rangle + \langle a\rangle\langle m\rangle + \langle b\rangle\langle k\rangle \tag{4.25}$$

$$6561 \ll 20.4M + 0.8M + 0.2M \tag{4.26}$$

$$\tag{4.27}$$

The maximal error on the background normalization is $\approx 6561/21.4\text{M}=0.03\%$. In central Au+Au collisions a much smaller fraction of the total pairs are from jets meaning the combinatoric jet term $\langle a \rangle \langle b \rangle$ is even smaller fraction of the total combinatoric pairs. Thus, with the current statistical and systematic errors, the systematic error due to the background normalization method is negligible.

4.7.7 Effects of Resonance Decays

Resonance decays could mimic a jet signal. In this analysis the dominant decay contribution is expected to be from the decay of $\Lambda \rightarrow \pi^- + p$ and $\bar{\Lambda} \rightarrow \pi^+ + \bar{p}$. In order to determine the contamination to the jet yields measured here from these decays, one million lambdas were generated and decayed into protons and π^-. The decays took place at the origin. The PHENIX acceptance was not used, as the conditional yield analyses are supposed to correct for it. The only exception to this would be where the proton hits the PHENIX acceptance and the π^- falls outside the η range of PHENIX.

Figure 4.29 shows the associated π p_T as a function of the p p_T. Within that range no associated π^- has p_T above 1.4GeV/c. Since the majority (about 70% in central Au+Au collisions) of the protons with $2.5 < p_T < 4.0$GeV/c have a p_T under 3.0GeV/c no Λ decay contribution to the jet conditional yield exists if the associated particles remain above 1.0GeV/c. About 22% of the

proton triggers are between $3.0 < p_T < 3.5\text{GeV}/c$ where the associated π^- contribution extents to $1.2\text{GeV}/c$, into the range used in the Run 2 analysis.

We have taken no additional systematic errors for this contamination. The statistical errors on the yields of partners below $1.2\text{GeV}/c$ are much larger than the resonance decay contribution.

Particle Charges	Real Pairs/Mixed Pairs
	$0.94 < \Delta\phi < 1.10$rad
+ +	0.046 ± 0.002
- -	0.044 ± 0.003
- +	0.041 ± 0.004
+ -	0.042 ± 0.001
	$1.26 < \Delta\phi < 2.04$rad
+ +	0.035 ± 0.005
- -	0.040 ± 0.007
+ -	0.052 ± 0.004
- +	0.048 ± 0.003

Table 4.4: Fraction of pairs for different charge combinations for two angular ranges, one where the mixed event $\frac{dN}{d\Delta\phi}$ distribution looks normal ($0.94 < \Delta\phi < 1.10$rad) and one where the mixed event distribution is not ($1.26 < \Delta\phi < 2.04$rad). In the normal region the fraction of pairs from different charge combinations is constant in the real and mixed pairs; in the second region it is different. The absolute values of the ratio depends only on the ratio of real to mixed pairs generated. In the absence of signal this ratio should be the same for all pair charge combinations; these $\Delta\phi$ regions are outside or at the edge of the near side jet signal window so contribution from signal pairs should be small.

	A	B	C	D
West Arm	4.17	20.56	-0.34	0.015
East Arm	3.5	18.47	-0.147	-0.0029

Table 4.5: Fit values to correction functions used in this analysis

Au+Au			
p_T	e_{West}	e_{East}	F
1.03	4.54	4.05	4.36
1.13	4.46	3.99	4.29
1.25	4.39	3.94	4.23
1.37	4.33	3.89	4.17
1.56	4.24	3.83	4.10
1.98	4.13	3.73	3.99
d+Au			
1.03	4.54	4.05	4.56
1.13	4.46	3.99	4.49
1.25	4.39	3.94	4.42
1.37	4.33	3.89	4.36
1.56	4.24	3.83	4.28
1.98	4.13	3.73	4.17
p+p			
1.03	4.54	4.05	4.56
1.13	4.46	3.99	4.48
1.25	4.39	3.94	4.42
1.37	4.33	3.89	4.36
1.56	4.24	3.83	4.28
1.98	4.13	3.73	4.17

Table 4.6: Values of the efficiency correction for the different collision systems. See text for explanation of the numbers.

Centrality	Tracking Efficiency	Error (%)
0-90	0.92	
0-10	0.85	5.0
10-20	0.90	5.0
20-40	0.95	3.6
40-60	0.96	3.6
60-90	0.99	2.3

Table 4.7: Values of the tracking efficiency as a function of centrality.

Centrality	Yield per Event
0-10%	6.4
0-5%	6.8
10-15%	4.9
15-20%	4.1
20-30%	3.1
30-40%	2.0
40-50%	1.2
50-60%	0.61
60-70%	0.28
70-80%	0.13
80-92%	0.050

Table 4.8: Values of the integral in Equation. 4.2 for various centrality selections for 1.7< p_T <2.5GeV/c .

p_T GeV/c	0-5%	5-10%	10-20%	20-40%	40-60%	60-90%
1.7-2.5	4.44	4.29	4.04	3.80	3.58	3.39

Table 4.9: Combined efficiency and occupancy correction values for unidentified partners for the centrality and p_T selections used in this analysis.

Type	0-5%	5-10%	10-20%	20-40%	40-60%	60-90%
baryons	7.2	6.7	6.3	5.7	5.1	4.2
mesons	8.2	7.9	7.4	7.0	6.5	5.9

Table 4.10: Combined efficiency and occupancy correction values for baryon and meson partners for 1.7< p_T <2.5GeV/c

Type	0-5%	5-10%	10-20%	20-40%	40-60%	60-90%
p	6.77753	6.32438	5.87426	5.44778	4.87903	4.02104
$\bar{p}$	8.1489	7.50864	7.10547	6.3126	5.57269	4.45299

Table 4.11: Combined efficiency and occupancy correction values for p and $\bar{p}$ partners for 1.7< p_T <2.5GeV/c

centrality	0-5%	5-10%	10-20%	20-40%	40-60%
$\langle p_T \rangle$	0-5%	5-10%	10-20%	20-40%	40-60%
1.03	0.031526	0.0591679	0.0778672	0.115266	0.133373
	± 0.015176	± 0.000317	± 0.000417	± 0.000459	± 0.001026
1.13	0.0341697	0.0640231	0.0840624	0.124141	0.143391
	± 0.016494	± 0.000394	± 0.000517	± 0.000564	± 0.001296
1.25	0.037253	0.0696432	0.0911542	0.134176	0.154625
	± 0.018050	± 0.000429	± 0.000561	± 0.000610	± 0.001398
1.37	0.0402391	0.0750385	0.0978726	0.143541	0.164998
	± 0.019577	± 0.000436	± 0.000568	± 0.000624	± 0.001474
1.56	0.0447684	0.0831211	0.107746	0.156996	0.179662
	± 0.021936	± 0.000483	± 0.000626	± 0.000682	± 0.001605
1.98	0.0539161	0.0989876	0.126249	0.180771	0.204422
	± 0.026897	± 0.000897	± 0.001144	± 0.001288	± 0.002936

Table 4.12: v_2 values and their errors for charged hadron partners from [31].

p_T GeV/c	0-5%	5-10%	10-20%	20-40%	40-60%
1.7-2.5	0.053994	0.098837	0.125508	0.178850	0.186815
	± 0.027062	± 0.003045	± 0.003867	± 0.004020	± 0.009879

Table 4.13: Meson v_2 values from Reference [31] for the centrality and p_T ranges used in this analysis.

p_T GeV/c	0-5%	5-10%	10-20%	20-40%	40-60%
1.7-2.5	0.059216	0.107142	0.133705	0.186832	0.215206
	± 0.030217	± 0.010909	± 0.013614	± 0.014764	± 0.037421

Table 4.14: Proton and anti-proton v_2 values from Reference [31] for the centrality and p_T ranges used in this analysis.

centrality	v_2^{meson}	$v_2^{baryons}$
0-5%	0.06 ± 0.03	0.09 ± 0.05
5-10%	0.10 ± 0.01	0.16 ± 0.02
10-20%	0.13 ± 0.01	0.19 ± 0.02
20-40%	0.18 ± 0.01	0.24 ± 0.02
40-60%	0.16 ± 0.02	0.22 ± 0.02

Table 4.15: v_2 values and errors for the trigger particles.

centrality	error (%)
0-5%	4.3
5-10%	5.8
10-20%	6.1
20-40%	5.6
40-60%	4.0
60-70%	4.0
dAu	9.5

Table 4.16: Values of the error on the yield from meson contamination in the baryons.

centrality	trigger mesons	trigger baryons
0-5%	0.008	0.015
5-10%	0.0089	0.0046
10-20%	0.005	0.008
20-40%	0.004	0.002
40-60%	0.0005	0.002
60-70%	0.0006	0.002
d+Au	0.0004	0.002

Table 4.17: Mixing error on the yields which comes primarily from the random number generation.

Centrality	Error
0-5%	5.0%
0-10%	5.0%
10-15%	5.0%
15-20%	5.0%
20-30%	3.6%
30-40%	3.6%
40-50%	3.6%
50-60%	3.6%
60-70%	2.3%
70-80%	2.3%
80-92%	2.3%

Table 4.18: Systematic error on the occupancy corrections in [25]. In the p_T ranges used in this analysis the occupancy corrections are independent of p_T ; this is an additional error on the absolute normalization of the spectra which is centrality dependent.

Centrality	Error
0-5%	6.4%
5-10%	6.4%
10-20%	8.1%
20-40%	6.5%
40-60%	5.2%
60-90%	5.6%

Table 4.19: Total point to point systematic errors on the efficiency corrections for the partners. An additional 7.4% systematic error changes all the efficiency corrections by the same factor.

Centrality	Reaction Plane Resolution Error
0-5%	12%
5-10%	12%
10-20%	12%
20-40%	4%
40-60%	5%
60-70%	5%

Table 4.20: Reaction plane resolution errors on the v_2 measurements from [31].

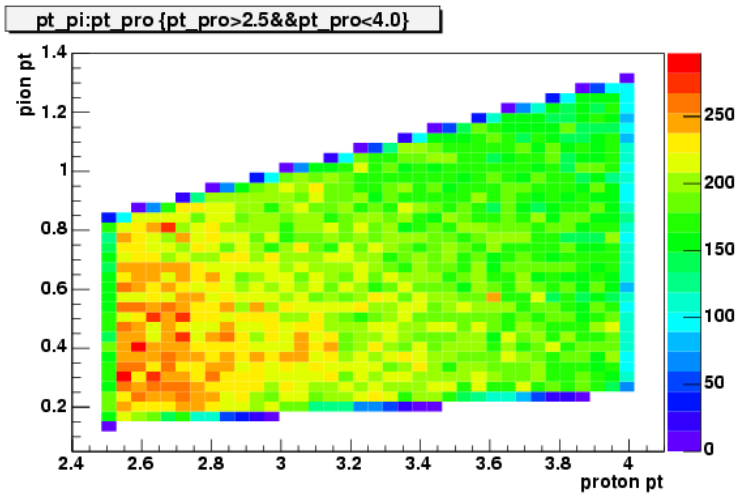

Figure 4.29: π^- p_T as a function of the proton p_T for decayed Λs.

4.7.8 Total Systematic Errors

The total systematic errors on the conditional yield measurement are the quadrature sums of the systematic errors from the sources described above. The systematic errors, broken down by source, for the Run 2 Au+Au and d+Au analyses are shown in Table 4.21.

4.7.9 Stability of Au+Au Results as a Function of Run Group

The final Au+Au results from Run 2 are a weighted average of the separate results from the six run groups. As a cross-check raw results (background subtracted, uncorrected peak integral) from each of the run groups are compared in Tables 4.22 (meson triggers) and 4.23 (baryon triggers); these are raw results and only the run group variation should be looked at not the centrality dependence (occupancy correction has not been done nor has the v_2 subtraction).

The numbers in Tables 4.22 and 4.23 are the subtracted peak integrals on the near side over 0.94rad. To turn these numbers into corrected yields they are multiplied by the efficiency correction (see Table 4.6) and divided by the occupancy correction (see Table 4.7). The v_2 contribution is subtracted by subtracting $0.47 B v_2^{trig} v_2^{part}$ where B is the combinatoric background level, v_2^{trig} and v_2^{part} are the trigger and partner v_2 values (see Tables 4.15 and 4.12) and 0.47 is the integral of $\cos(2\Delta\phi)$ from 0 to 0.94 rad. The run to run values given here are for one choice of ξ, N_{part} as the parameter of the arctan function (not an average of all four possible values as the final results are.

Variation Within the Run Groups As a final cross check on the stability of the run groups the two largest run groups (E00W00 and E00W32) were divided into into subgroups according to run number and the analysis was done separately on each subgroup. Significant variation in the results between the subgroups could mean that the run groups were too large and contained too many variations in the detector acceptance to get reasonable results. The mixed pair $\frac{dN}{d\Delta\phi}$ distributions from the subgroups were each divided by the mixed $\frac{dN}{d\Delta\phi}$ distribution from the corresponding large group. The ratios for the E00W00 run group in four vertex selections are shown in Figure 4.30 and for the E00W32 run group in 4.31. There is no significant run group dependence.

Figures 4.32 and 4.33 show the distributions χ^2 values of the horizontal line fits for the E00W00 and E00W32 run groups, respectively. The subgroup color scheme is the same as in Figures 4.30 and 4.31. No one subgroup has significantly worse χ^2 values than any other and all the fits are reasonable (the number of degrees of freedom is usually $\approx$12, some bins around $\Delta\phi = \pi/2$ are not populated.

N_{part}	trigger type	centrality corr	v_2	occupancy	PID	mix
351	baryons	-0.0010/+0.0027	0.0086	0.0012	0.0010	0.015
351	mesons	-0.0012/+0.0008	0.0054	0.0033	0	0.008
300	baryons	-0.0036/+0.0026	0.0084	0.0023	0.0027	0.005
300	mesons	-0.0019/+0.0015	0.0050	0.0036	0	0.009
235	baryons	-0.0027/+0.0031	0.0095	0.0032	0.0038	0.008
235	mesons	-0.0020/+0.0021	0.0063	0.0036	0	0.005
140	baryons	-0.0055/+0.0049	0.0044	0.0022	0.0035	0.002
140	mesons	-0.0040/+0.0039	0.0028	0.0021	0	0.004
60	baryons	-0.0036/+0.0049	0.0026	0.0020	0.0022	0.002
60	mesons	-0.0036/+0.0035	0.0018	0.0021	0	0.0005
26	baryons	-0.0011/+0.0018	-0.0007/+0.0044	0.0013	0.0022	0.002
26	mesons	-0.0014/+0.0013	-0.0005/+0.0033	0.0006	0	0.0006
9 (d+Au)	baryons	0.0060		0.0032	0.002	
9 (d+Au)	mesons	0.0043		0	0.0004	

Table 4.21: Absolute systematic errors on the near side yields.

Run Group	0-10%	10-20%	20-40%	40-60%
E00W00	0.015±0.005	0.024±0.005	0.022±0.003	0.015±0.003
E00W32	0.017±0.003	0.019±0.003	0.018±0.002	0.017±0.002
E00W20	0.019±0.008	0.022±0.008	0.028±0.006	0.022±0.006
E00W33	0.030±0.009	0.047±0.009	0.029±0.006	0.014±0.006
E20W20	0.017±0.007	0.021±0.007	0.021±0.005	0.024±0.005
E20W00	0.014±0.010	0.022±0.010	0.021±0.007	0.011±0.007

Table 4.22: Run group variation of the raw results for different centralities in Au+Au (meson triggers). The run groups are defined in Section 4.1.1. Errors are statistical.

Run Group	0-10%	10-20%	20-40%	40-60%
E00W00	0.008±0.006	0.027±0.007	0.028±0.005	0.022±0.006
E00W32	0.012±0.004	0.022±0.004	0.025±0.003	0.020±0.004
E00W20	0.016±0.010	0.006±0.010	0.011±0.008	0.006±0.009
E00W33	0.016±0.010	0.036±0.011	0.023±0.009	0.016±0.009
E20W20	0.013±0.009	0.030±0.010	0.030±0.007	0.006±0.007
E20W00	0.007±0.013	0.017±0.013	0.030±0.010	0.025±0.012

Table 4.23: Run group variation of the raw results for different centralities in Au+Au (baryon triggers). The run groups are defined in Section 4.1.1. Errors are statistical.

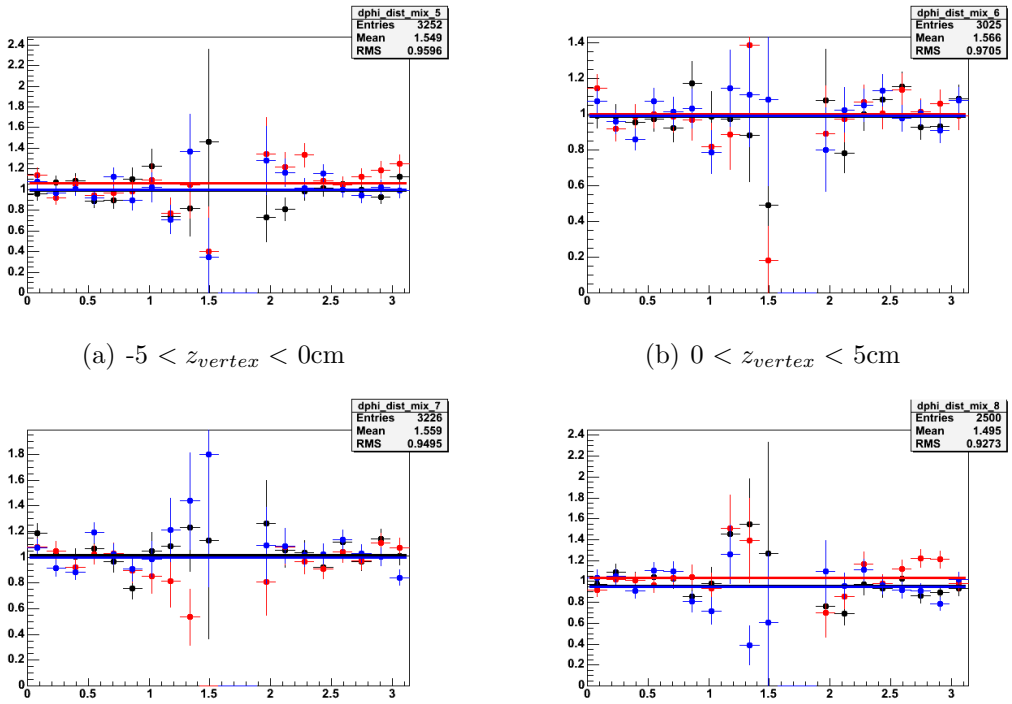

(a) -5 < z_{vertex} < 0cm

(b) 0 < z_{vertex} < 5cm

(c) 5 < z_{vertex} < 10cm

(d) 10 < z_{vertex} < 15cm

Figure 4.30: Ratio of the mixed pair $\frac{dN}{d\Delta\phi}$ distributions from the subgroups of the E00W00 run group to the mixed pair distributions $\frac{dN}{d\Delta\phi}$ distributions constructed by mixing pairs from the entire run group. Each color denotes a subgroup. Solid lines are fits to horizontal lines of the ratio of the same color. Each panel is an independent set of events for a different event vertex selection.

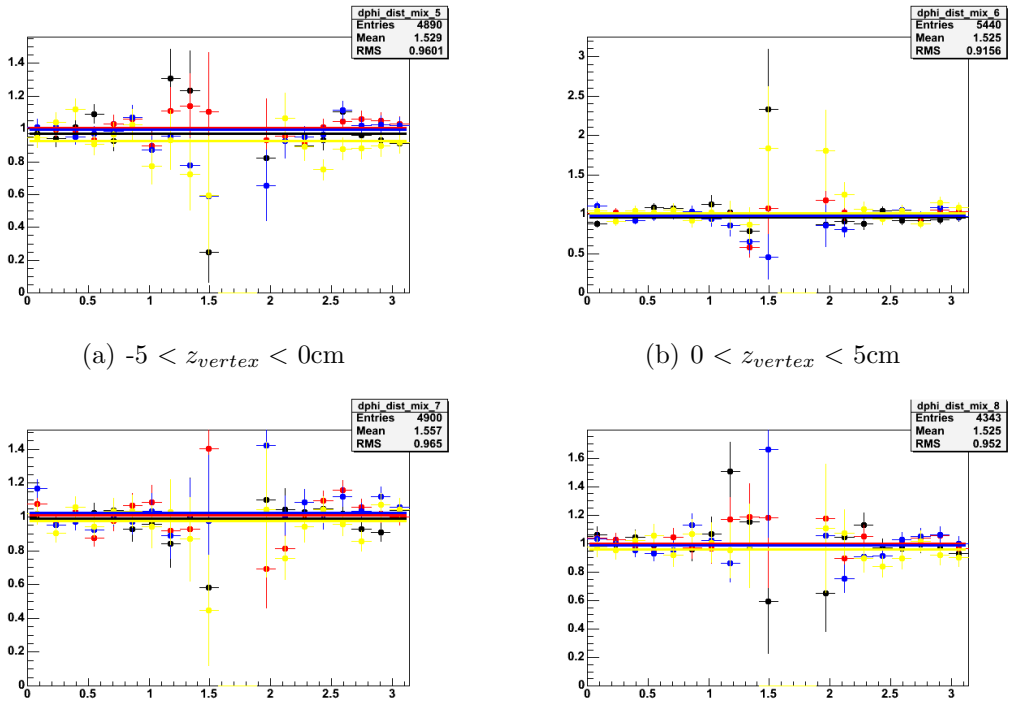

(a) -5 < z_{vertex} < 0cm

(b) 0 < z_{vertex} < 5cm

(c) 5 < z_{vertex} < 10cm

(d) 10 < z_{vertex} < 15cm

Figure 4.31: Ratio of the mixed pair $\frac{dN}{d\Delta\phi}$ distributions from the subgroups of the E00W32 run group to the mixed pair distributions $\frac{dN}{d\Delta\phi}$ distributions constructed by mixing pairs from the entire run group. Each color denotes a subgroup. Solid lines are fits to horizontal lines of the ratio of the same color. Each panel is an independent set of events for a different event vertex selection.

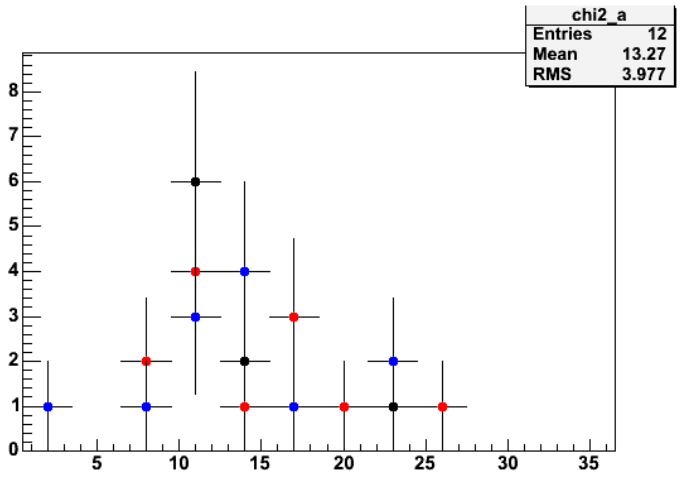

Figure 4.32: Histogram of χ^2 values of fits to horizontal lines of the ratios of $\frac{dN}{d\Delta\phi}$ distributions in subgroups to the entire E00W00 run group. Each color corresponds to a different subgroup.

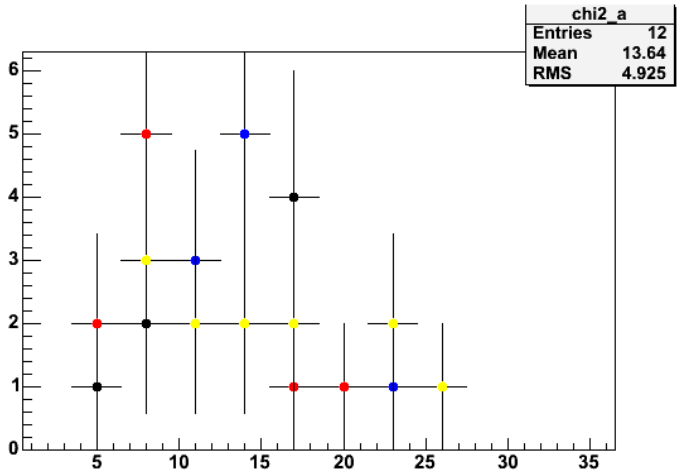

Figure 4.33: Histogram of χ^2 values of fits to horizontal lines of the ratios of $\frac{dN}{d\Delta\phi}$ distributions in subgroups to the entire E00W32 run group. Each color corresponds to a different subgroup.

Chapter 5

Results

5.1 Identified Leading Particle Correlations in Runs 2 & 3

5.1.1 Azimuthal Angular Difference Plots

Figure 5.1 shows the azimuthal angular difference distributions for triggers with 2.5< p_T <4.0GeV/c and partners with 1.7< p_T <2.5GeV/c for six centralities in Au+Au (baryon and meson triggers), p+p (non-identified triggers) and minimum bias d+Au (trigger mesons). The solid lines indicate the level of combinatoric background, which in Au+Au is modulated by the factor in Equation 4.9 with the measured v_2 values. Systematic errors are not shown. The large error bars and missing points at $\Delta\phi \approx \pi/2$ are because of the very small acceptance there when requiring one particle to be matched in the TOF.

The near side jet peak is clearly visible in all centralities for meson triggers. In the baryon triggered distributions, the statistics are more marginal, but the

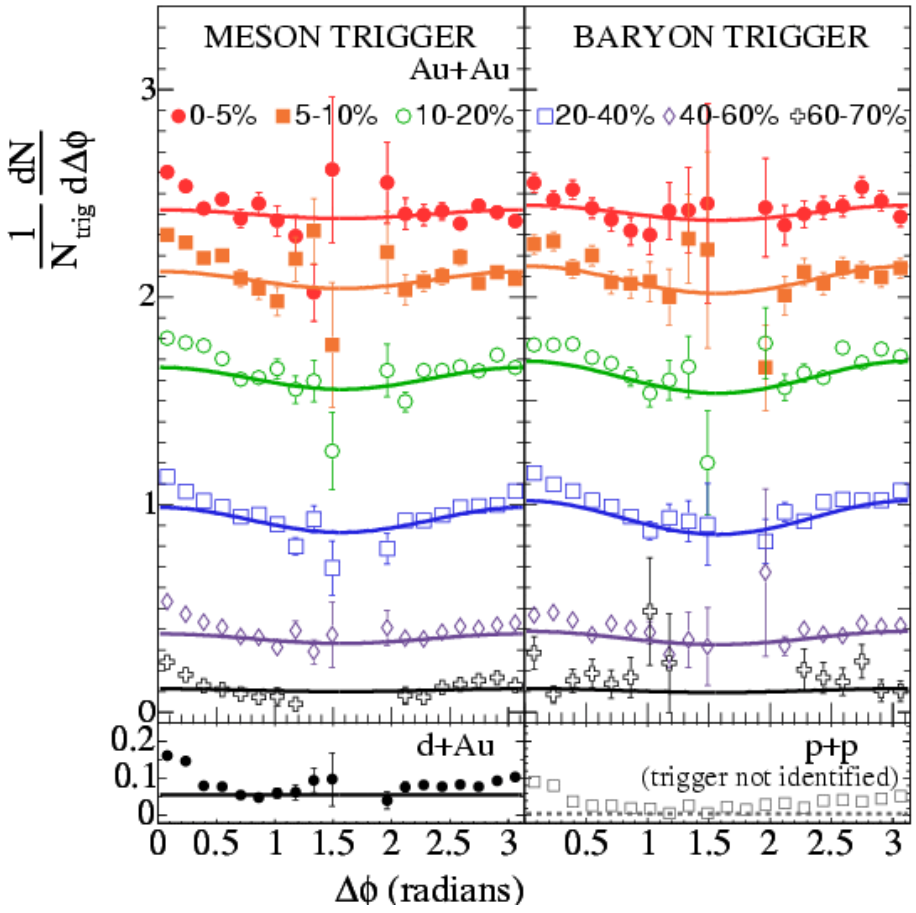

Figure 5.1: Azimuthal angular difference plots for charged particles with 1.7< p_T <2.5GeV/c associated with trigger mesons (left panels) and trigger baryons (top right panel) and inclusive charged particles (bottom right panel) in Au+Au (top panels), d+Au (bottom left panel) and p+p (bottom right panel).

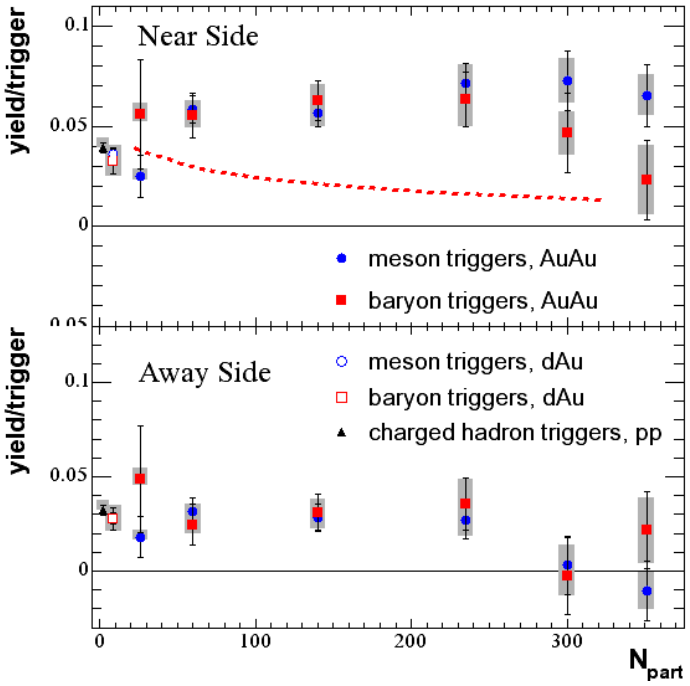

Figure 5.2: Yield of associated particles with 1.7< p_T <2.5GeV/c per trigger with 2.5< p_T <4.0GeV/c in Au+Au, d+Au and p+p collisions. The near side (top panel) is integrated for 0.0< $\Delta\phi$ <0.94rad and the away side (bottom panel) is integrated for 2.2< $\Delta\phi$ < πrad. Points are from the azimuthal angle distributions in Figure 5.1.

distributions are consistent with the presence of a near side jet peak. The away side jet is harder to see in the Au+Au on these plots since it is expected to have a smaller amplitude (due to the possibility of it falling outside the PHENIX η acceptance) and be wider than the near side peaks due to the partonic k_T. The width and amplitude differences can be clearly seen in the p+p and d+Au data.

5.1.2 Jet Conditional Yields

Figure 5.2 shows the fully corrected associated particle yield per trigger for trigger baryons (red squares) and mesons (blue circles) between 2.5 and 4.0 GeV/c and charged particles between 1.7 and 2.5 GeV/c as a function of the number of participating nucleons in the collision (N_{part}). The near side points (top panel) are integrated over $0 < \Delta\phi < 0.94$rad and the v_2 modulated combinatoric background is subtracted. The away side points (bottom panel) are integrated over $2.2 < \Delta\phi < \pi$rad. Statistical error bars are shown as bars and systematic as grey boxes.

On the near side, the Au+Au points show a lack of centrality dependence for N_{part} greater than 50 with little difference between the trigger baryon and trigger meson points. The plateau value for the mid-central and central Au+Au points is approximately one and a half times higher than the values for the conditional yields in d+Au and p+p collisions, indicating a strong medium influence on the jet yields in Au+Au collisions. The two most central trigger baryon points appear to drop, possibly indicating the introduction of a non-jet baryon source. However, the statistical error bars are too large to rule out a fluctuation. Additionally, any medium dependence is expected to smoothly evolve with centrality, as the baryon excess does, rather than appear suddenly at high centralities. The dashed line in in Figure 5.2 represents a toy model calculation which will be discussed in Section 6.3.

On the away side there is no significant centrality or collision system dependence for N_{part} less than 300 which appears to suggest that the away side jet is not strongly modified by the medium. Given that the near side jet is

strongly modified by the medium and is likely biased toward jets that originate near the surface, thus seeing much less of the medium than the away side, the away side jet must be interacting with the medium. The apparent lack of modification is likely to be accidental. Indeed, in the most central collisions, the away side yield into the fixed $\Delta\phi$ range is in agreement with previous measurements [46] which show a decreasing away side conditional yield.

5.1.3 Jet Width as a Function of p_T

Jet particles typically surround the primary parton direction in a cone determined by j_T. j_T is the transverse momentum of the fragmentation hadrons with respect to the primary parton direction. Figure 5.3 shows the relationship between j_T and the transverse momenta of the parent parton and final state hadron.

j_T has been measured to be independent of $\sqrt{s}$ and particle p_T [15, 55] and collision centrality. The PHENIX measurement of $\langle|j_T|\rangle$ is 0.359 $\pm$ 0.011 GeV/c. $\langle|j_{Ty}|\rangle$ is the width of the y projection of the two dimensional Gaussian whose width is $\langle j_T\rangle$:

$$\langle j_T\rangle = \sqrt{\pi/2}\langle|j_{Ty}|\rangle = 0.44 GeV/c$$

We use this value to determine the angular jet width as a function of the trigger and associated particle p_T:

$$\sigma = \sqrt{\left(\frac{\langle j_T\rangle}{p_{T,trig}}\right)^2 + \left(\frac{\langle j_T\rangle}{p_{T,part}}\right)^2}$$

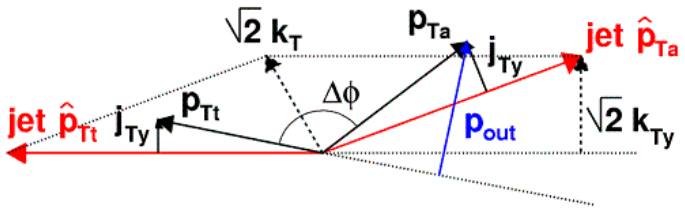

Figure 5.3: Vector illustration of jet fragmentation. *jet* $\hat{p_{Tt}}$ is the jet parton's transverse momentum and p_{Tt} is the transverse momentum of one of the jet final state hadrons. j_{Ty} is the y-projection of the transverse momentum between the parton and hadron momenta, j_T.

$p_{T,part}$	jet width (radians)
1.00-1.07	0.45
1.07-1.20	0.42
1.20-1.30	0.38
1.30-1.45	0.36
1.45-1.70	0.32
1.70-2.50	0.27

Table 5.1: Jet width in radians based on $\langle j_T \rangle = 0.44\text{GeV}/c$. $2.5 < p_{T,trig} < 4.0\text{GeV}/c$ in all cases.

where $p_{T,trig}$ and $p_{T,part}$ are the mean p_T of the trigger and partner particle bins, respectively. For the $p_{T,part}$ bins used in this analysis the jet widths are given in Table 5.1.

Jet Width in $\Delta\eta$ Assumption Because of PHENIX's limited acceptance in $\Delta\eta$ ($|\Delta\eta| < 0.7$) and the changing jet width with $p_{T,part}$ the fraction of particles from the jet-cone which are measured in PHENIX is not constant. Additionally, the low statistics of the Run 2 dataset and the small PHENIX $\Delta\eta$ acceptance do not allow us to directly measure the width of the jet in $\Delta\eta$ (the $\langle j_T \rangle$ values above come from a one dimensional measurement in $\Delta\phi$). With the Run 4 data it should be possible to directly measure the jet width

in $\Delta\eta$.

We make the assumption that the jet is a symmetric Gaussian in $\Delta\eta$ and $\Delta\phi$ in order to correct for the undetected jet particles. In p+p collisions this is expected to be a good assumption since there is no preferred direction as the parton fragments. In Au+Au collisions, however, there is evidence that the medium breaks the symmetry in some manner (possibly the longitudinal expansion of the system [56]) leading to different jet widths in $\Delta\eta$ and $\Delta\phi$ [49]. The available data is insufficient to determine the shape of the jet in $\Delta\eta$ at the p_T range of this analysis.

Correction for PHENIX Acceptance Based on the symmetric Gaussian assumption and the actual shape of the PHENIX acceptance in $\Delta\eta$ it is possible to determine the fraction of jet particles which are missed as a function of the jet width.

The fraction of the jet particles in the PHENIX acceptance is then given by the curve in Figure 5.4 which comes from the convolution of the Gaussian jet shape with the PHENIX pair acceptance in $\Delta\eta$. Table 5.2 shows the fraction of jet particles and widths as a function of the partner p_T range. The conditional yields are corrected upward by the reciprocal of the fraction of jet particles. This results in the true number of jet partners per trigger that would have been observed in a perfect detector under the symmetric Gaussian assumption.

5.1.4 Near Side Jet p_T Spectra

Figure 5.5 shows the near side associated particle p_T spectra under the width assumption described above. Only statistical errors are shown in the figure.

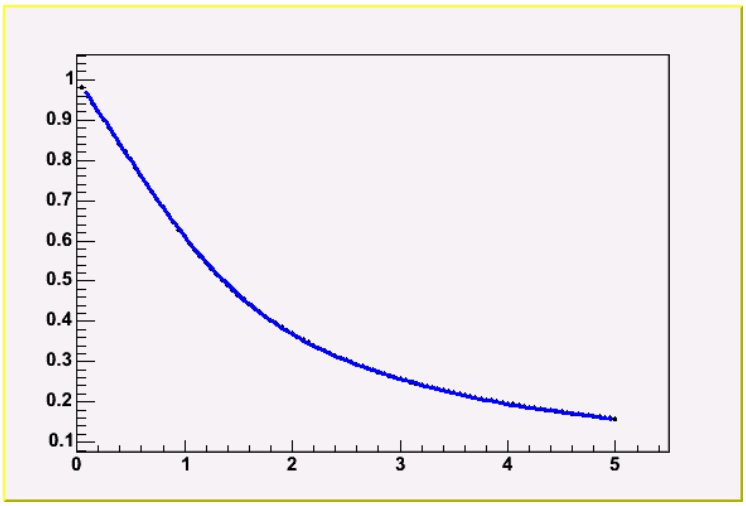

Figure 5.4: Fraction of the jet partner particles detected in PHENIX as a function of the jet width in units of $rad/0.35$ (half the nominal PHENIX η acceptance).

partner p_T range	jet width (rad)	fraction of jet in PHENIX
1.00-1.07	0.45	0.50
1.07-1.20	0.42	0.53
1.20-1.30	0.38	0.57
1.30-1.45	0.36	0.60
1.45-1.70	0.32	0.64
1.70-2.50	0.27	0.69

Table 5.2: Jet widths and fraction of the jet partner particles in PHENIX as a function of partner p_T.

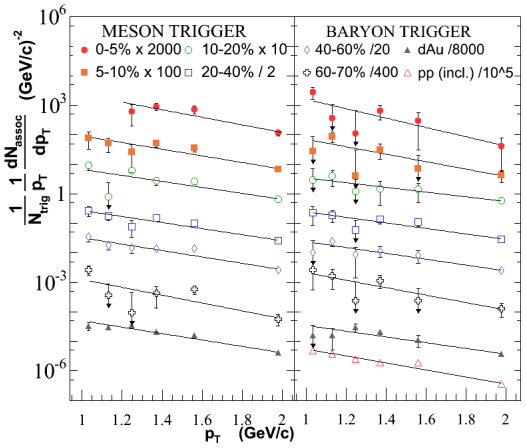

Figure 5.5: Near side associated particle p_T spectra for triggers with 2.5< p_T <4.0GeV/c for Au+Au, d+Au and p+p (inclusive charged particle trigger).

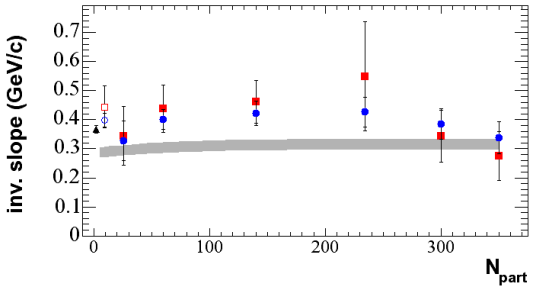

Figure 5.6: Inverse slopes of the near side associated particle p_T spectra from the exponential fits shown in 5.5. Errors are statistical only. The gray band shows the inverse slope of the inclusive charged hadron p_T spectra in Au+Au collisions from [25].

The systematic errors shown in 5.2 do not have a strong p_T dependence and are smaller than the statistical errors on the yields.

Spectra Slopes Figure 5.6 shows the inverse slopes as a function of N_{part} from the fits in 5.5. The grey band shows the slope of the inclusive spectra in the p_T range of the partners in 5.5 ($1.0 < p_T < 2.5$). Within the large statistical errors, there is no strong centrality and collision system dependence.

The main systematic uncertainty is the validity of the symmetric Gaussian

approximation used to correct for the PHENIX acceptance. Given the current knowledge of the jet shape in $\Delta\eta$ it is not possible to determine the accuracy of the correction. We conservatively put an uncertainty of 50% on the correction in the most central collisions which translates to a 20% uncertainty on the slope. This is comparable to the statistical error for the meson triggered points and smaller than the statistical error for the baryon triggered points.

Broadening in $\Delta\eta$ has been observed in a similar p_T range [49]. While the p_T and centrality dependence are incomplete, it appears that the broadening becomes greater at lower partner p_T. If this is the case then our assumption under-corrects the partner yield at the lowest p_T. The proper correction would then decrease the inverse slopes in the most central collisions, where the medium effects should be the largest. Under our assumption, the most central inverse slopes are already in agreement with those from the inclusive spectra. It is unclear what physical scenario would give jet partners a steeper spectrum than inclusive hadrons. Realistically, it does not appear that any broadening in $\Delta\eta$ could have a large effect on the slopes shown in Figure 5.6.

The lack of strong dependence on collision system and centrality dependence of the inverse slopes is further evidence that the trigger particles in Au+Au collisions are from the same jet-like mechanism as in p+p and d+Au collisions. A study of the trigger p_T dependence of the slopes for both p+p and Au+Au would be useful to further constrain the jet production mechanism in Au+Au collisions.

5.2 Identified Leading Particle Correlations in Run 4

Figure 5.7 shows the $\frac{1}{N_{trig}}\frac{dN}{d\Delta\phi}$ distributions for identified trigger particles with unidentified partner particles. Figures 5.8 and 5.9 show the near side yields integrated over 0.94rad. These distributions are directly comparable to Figures 5.1 and 5.2. The Run 4 analysis contains approximately 700 million events. The high statistics dataset confirms that the difference in the near side conditional yields for trigger baryons and mesons in the most central collisions seen in the top panel of 5.2 is significant. There is a 4.3σ difference between the baryon and meson triggered points at N_{part}=300 and a 5.1σ difference at N_{part}=351. These numbers use the statistical errors only as the systematic errors contain components which move the baryon and meson triggered conditional yields in the same manner. At other centralities and on the away side there is no significant difference between baryon and meson triggered correlations. Figure 5.9 shows a significant drop in the away side partner yield in central Au+Au collisions. A fit to the meson triggered away side yields as a function of centrality has a chi^2/dof of 2.8/3 for points at N_{part} <300 and 20.1/5 if all points are included. For the baryon triggered yields, the chi^2/dof is 20.1/3 for points at N_{part} <300 and 38.4/5 if all points are included.

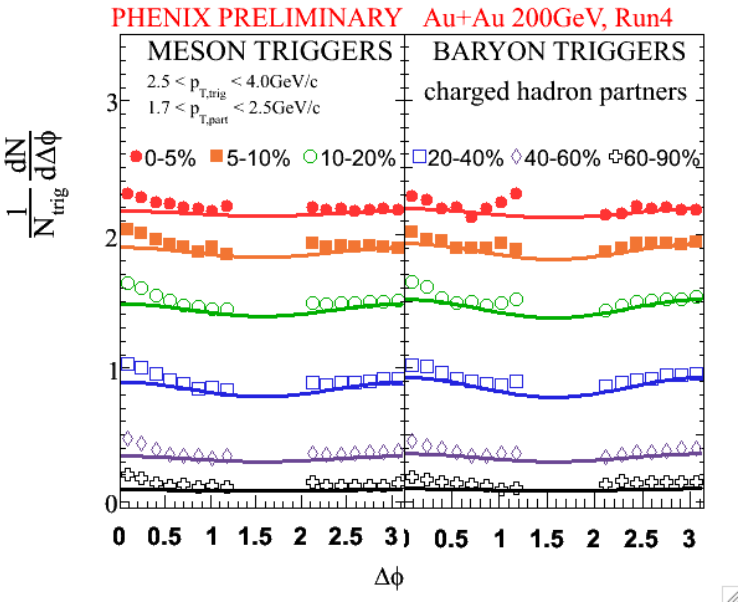

Figure 5.7: $\frac{1}{N_{trig}}\frac{dN}{d\Delta\phi}$ distributions for triggers with 2.5 $< p_T <$4.0GeV/c identified in the TOF as mesons (left panel) or baryons (right panel) and partners with 1.7$< p_T <$2.5GeV/c . The data points show six centralities: 0-5% (red), 5-10% (orange), 10-20% (green), 20-40% (blue), 40-60% (purple) and 60-90% (black). The solid lines show the combinatoric background level modulated by the v_2 contribution. Corrections for efficiency, acceptance and multiplicity have been applied.

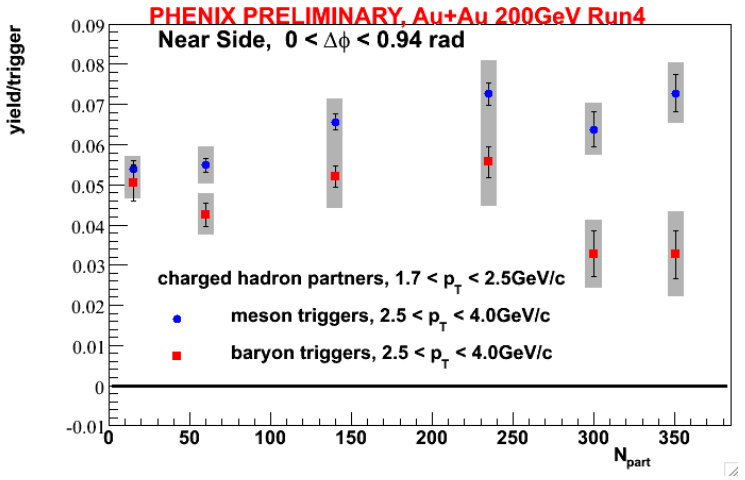

Figure 5.8: Integrated yields per trigger on the near side, 0< $\Delta\phi$ <0.94rad for triggers between 2.5< p_T4.0GeV/c and partners between 1.7< p_T <2.5GeV/c as a function of N_{part}. Squares are for trigger baryons and circles are for trigger mesons.

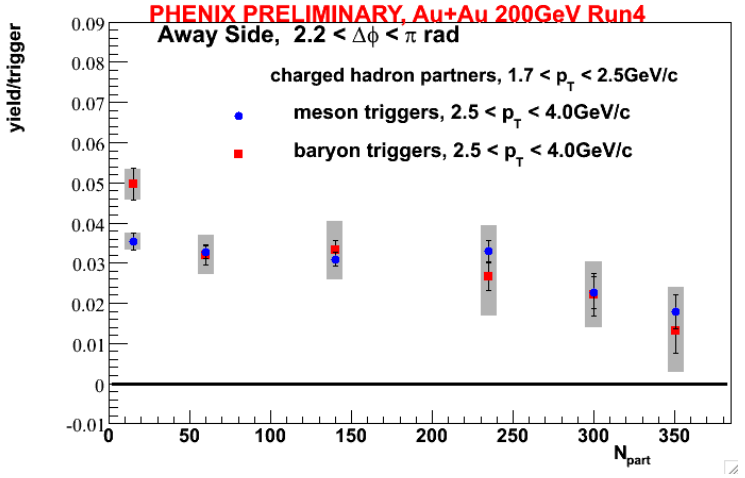

Figure 5.9: Integrated yields per trigger on the far side, 2.2< $\Delta\phi$ < πrad for triggers between 2.5< p_T4.0GeV/c and partners between 1.7< p_T <2.5GeV/c as a function of N_{part}. Squares are for trigger baryons and circles are for trigger mesons.

5.3 Correlations Between Identified Pairs

Here we present the results of two particle correlations where both the trigger and partner particles have been identified as baryons or mesons in Run 4. Figures 5.10 and 5.13 show azimuthal angular difference distributions for leading baryons and mesons with partner mesons and baryons, respectively. Partner mesons for both trigger types show a more pronounced near side jet structure as would be expected from normal fragmentation which favors meson production.

Figures 5.11 and 5.14 show the near side associated yields for both trigger types with meson and baryon partners, respectively. The only significant difference between the baryon and meson triggers is the decrease in the meson partner yield in the most central collisions, greater than 300 participants. The difference between the baryon and meson triggered conditional yields at N_{part}=300 is 1.4σ and at N_{part}=351 it is 2.9σ. No similar decrease is seen for baryon partners, but the statistical errors are large. Figures 5.12 and 5.15 show the away side yields for both trigger types and meson and baryon partners, respectively. No centrality strong dependence is observed. Values from horizontal line fits to the away side yields as a function of N_{part} are shown in Table 5.3. The χ^2/dof is reasonable except for the baryon-baryon correlations. With the large statistical and systematic errors here, the lack of centrality dependence of the away side yields with identified partners is not inconsistent with the decrease in the away side yields with unidentified partners in Figure 5.9.

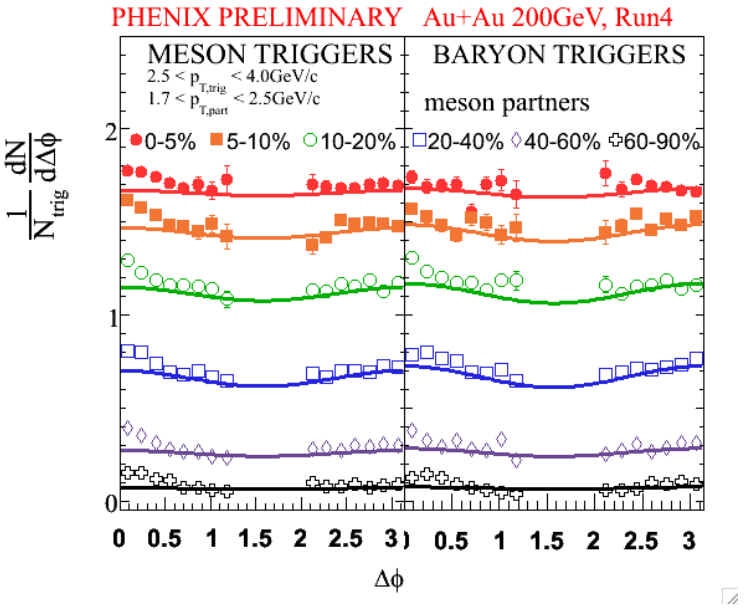

Figure 5.10: $\frac{1}{N_{trig}}\frac{dN}{d\Delta\phi}$ distributions for triggers with 2.5 $< p_T <$4.0GeV/c identified in the TOF as mesons (left panel) or baryons (right panel) and partners with 1.7$< p_T <$2.5GeV/c identified as mesons. The data points show six centralities: 0-5% (red), 5-10% (orange), 10-20% (green), 20-40% (blue), 40-60% (purple) and 60-90% (black). The solid lines show the combinatoric background level modulated by the v_2 contribution. Corrections for efficiency, acceptance and multiplicity have been applied.

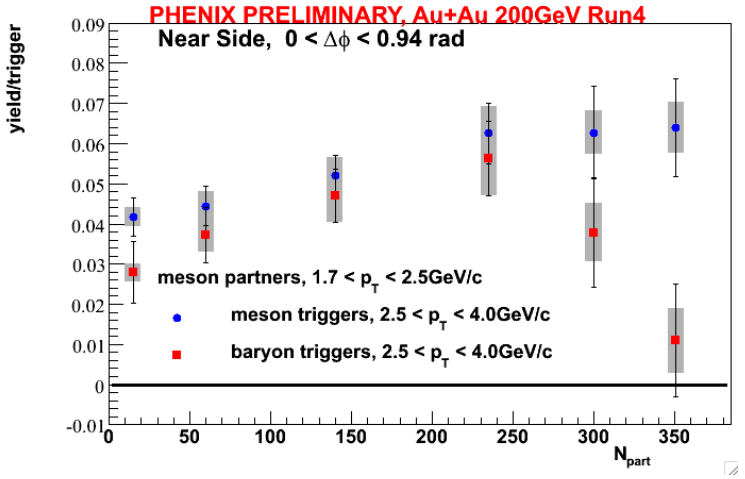

Figure 5.11: Integrated yields per trigger on the near side, 0< $\Delta\phi$ <0.94rad for triggers between 2.5< p_T <4.0GeV/c and partners between 1.7< p_T <2.5GeV/c identified as mesons as a function of N_{part}. Squares are for trigger baryons and circles are for trigger mesons.

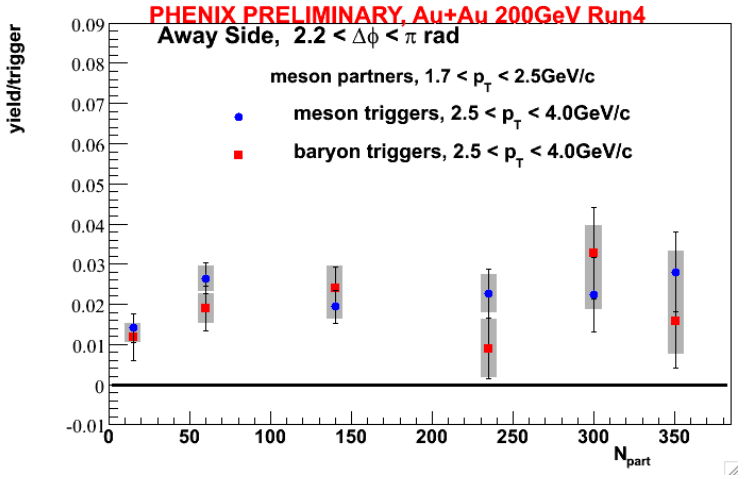

Figure 5.12: Integrated yields per trigger on the far side, 2.2< $\Delta\phi$ < πrad for triggers between 2.5< p_T <4.0GeV/c and partners between 1.7< p_T <2.5GeV/c identified as mesons as a function of N_{part}. Squares are for trigger baryons and circles are for trigger mesons.

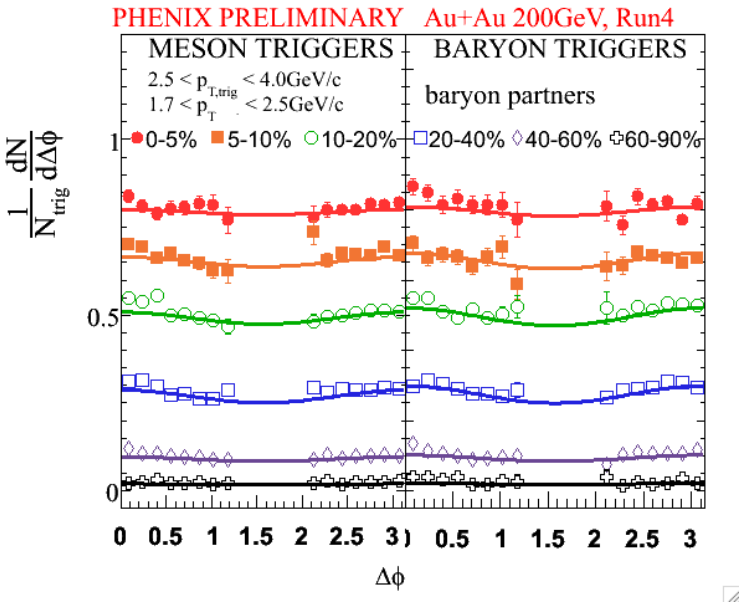

Figure 5.13: $\frac{1}{N_{trig}}\frac{dN}{d\Delta\phi}$ distributions for triggers with 2.5 $< p_T <$4.0GeV/c identified in the TOF as mesons (left panel) or baryons (right panel) and partners with 1.7$< p_T <$2.5GeV/c identified as baryons. The data points show six centralities: 0-5% (red), 5-10% (orange), 10-20% (green), 20-40% (blue), 40-60% (purple) and 60-90% (black). The solid lines show the combinatoric background level modulated by the v_2 contribution. Corrections for efficiency, acceptance and multiplicity have been applied.

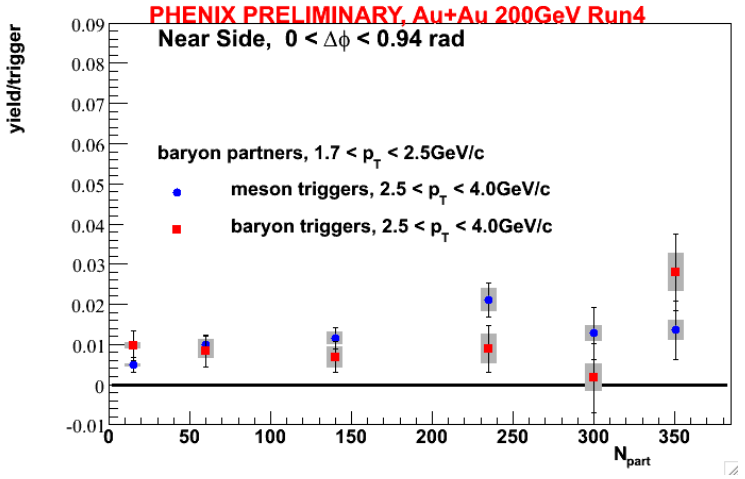

Figure 5.14: Integrated yields per trigger on the near side, 0< $\Delta\phi$ <0.94rad for triggers between 2.5< p_T <4.0GeV/c and partners between 1.7< p_T <2.5GeV/c identified as baryons as a function of N_{part}. Squares are for trigger baryons and circles are for trigger mesons.

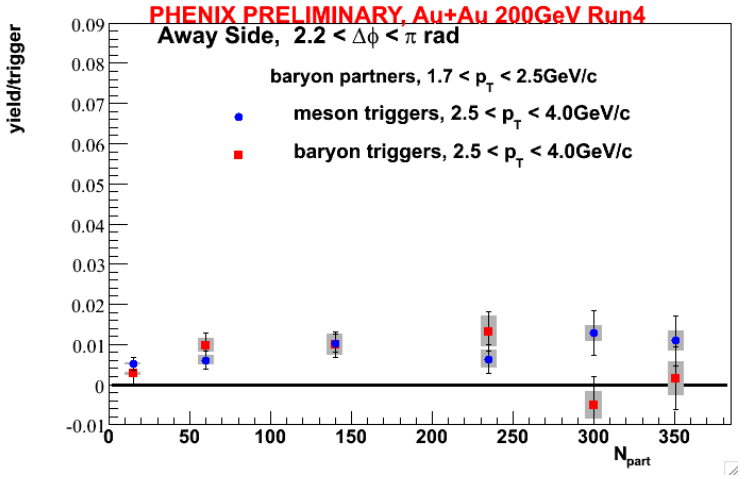

Figure 5.15: Integrated yields per trigger on the far side, 2.2< $\Delta\phi$ < πrad for triggers between 2.5< p_T <4.0GeV/c and partners between 1.7< p_T <2.5GeV/c identified as baryons as a function of N_{part}. Squares are for trigger baryons and circles are for trigger mesons.

trigger	partner	fit value	χ^2/dof
meson	meson	0.020±0.002	6.4/5
baryon	meson	0.018±0.003	5.5/5
meson	baryon	0.007±0.001	5.2/5
baryon	baryon	0.007±0.002	8.8/5

Table 5.3: Fit values for horizontal line fits to the away side yields as a function of N_{part} shown in Figures 5.12 and 5.15.

5.4 Baryon and Anti-Baryon Correlations

Correlations between identified protons and anti-protons further explore the modified fragmentation process in Au+Au collisions. Here, the protons and anti-protons have been identified with the TOF (trigger and partner) and the EMCal (partner particles) and the particle charge. These include protons and anti-protons which come from the decay of Λ and $\bar{\Lambda}$. Figures 5.16 and 5.17 show the angular difference distributions for partner protons and anti-protons, respectively for triggers identified as protons and anti-protons. For both partner types a strong near side jet peak is seen for opposite sign pairs (trigger protons with partner anti-protons with trigger anti-protons and partner protons) while no significant near jet peak is seen for same sign pairs (trigger protons with partner protons and trigger anti-protons with partner anti-protons). Figure 5.18 shows the near and away side conditional yields for these correlations. On the near side the conditional yields are consistent with zero at all centralities for correlations between the same sign particles (p-p and $\bar{p}$-$\bar{p}$). There are non-zero conditional yields for combinations between opposite charge particles on the near side. Interestingly, the $\bar{p}$-p correlations are systematically higher than p-$\bar{p}$ correlations at all centralities. A fit to a horizontal line for $\bar{p} - p$ correlations as a function of N_{part} gives 0.012±0.002 and for $p - \bar{p}$ correlations the value is 0.008±0.001. On the away side, the yields are independent of the trigger type and the charges of the particles, within the statistical errors.

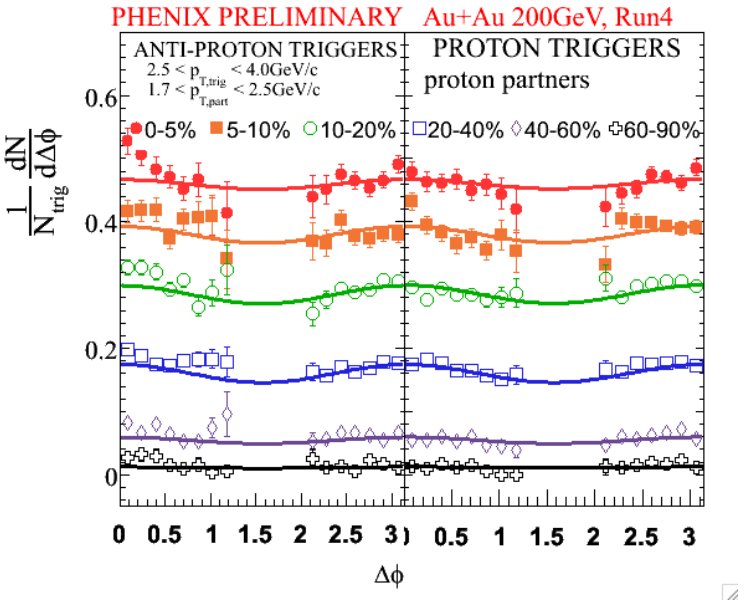

Figure 5.16: $\frac{1}{N_{trig}}\frac{dN}{d\Delta\phi}$ distributions for triggers with 2.5 < p_T <4.0GeV/c identified in the TOF as anti-protons (left panel) or protons (right panel) and proton partners with 1.7< p_T <2.5GeV/c . The data points show six centralities: 0-5% (red), 5-10% (orange), 10-20% (green), 20-40% (blue), 40-60% (purple) and 60-90% (black). The solid lines show the combinatoric background level modulated by the v_2 contribution. Corrections for efficiency, acceptance and multiplicity have been applied.

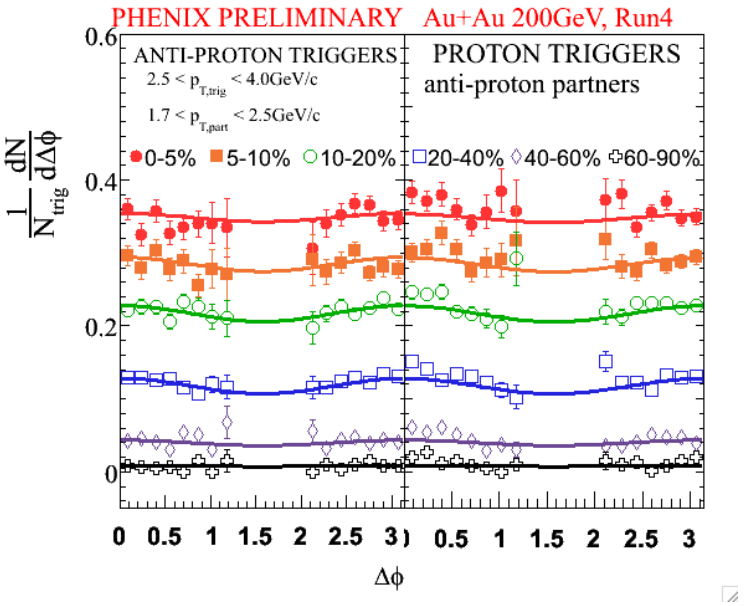

Figure 5.17: $\frac{1}{N_{trig}}\frac{dN}{d\Delta\phi}$ distributions for triggers with 2.5 < p_T <4.0GeV/c identified in the TOF as anti-protons (left panel) or protons (right panel) and anti-proton partners with 1.7< p_T <2.5GeV/c . The data points show six centralities: 0-5% (red), 5-10% (orange), 10-20% (green), 20-40% (blue), 40-60% (purple) and 60-90% (black). The solid lines show the combinatoric background level modulated by the v_2 contribution. Corrections for efficiency, acceptance and multiplicity have been applied.

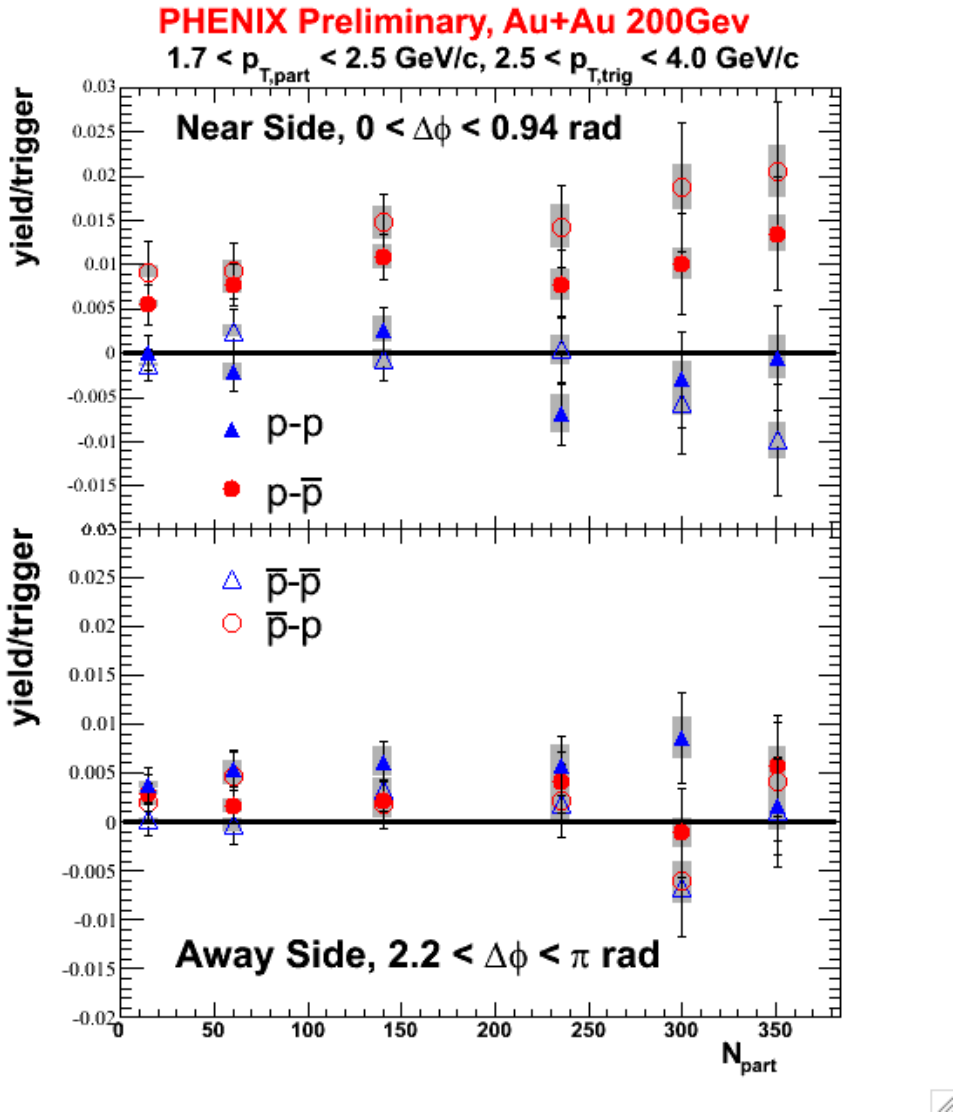

Figure 5.18: Near and away side conditional yields for p-p (solid blue triangles), p-$\bar{p}$ (solid red circles), $\bar{p}$-$\bar{p}$ (hollow blue triangles) and $\bar{p}$-p correlations. In all cases the trigger particles are from 2.5< p_T <4.0GeV/c and the associated particles are from 1.7< p_T <2.5GeV/c .

Chapter 6

Discussion

6.1 Thermal Recombination

The purely thermal recombination model in [32] predicts that a large fraction of the trigger particles come from non-jet sources (see Figure 1.14). If additional baryons and mesons are being formed by recombination, the jet yield per trigger should be diluted by the addition of non-jet triggers. Figure 6.1 shows the near side conditional yields as in Figure 5.2. The two lines show what the near side conditional yields should be, based on the recombination fraction in Figure 1.14, normalized to no triggers from recombination in the p+p conditional yields (both baryon and meson triggers are normalized to the same unidentified trigger p+p measurement; normalizing to the identified trigger d+Au measurements would slightly lower each curve); all trigger production from recombination dilutes the conditional yield from the p+p level. The dot-dashed line (blue) is the thermal recombination expectation for meson triggers and the dashed line (red) is the expectation for trigger baryons.

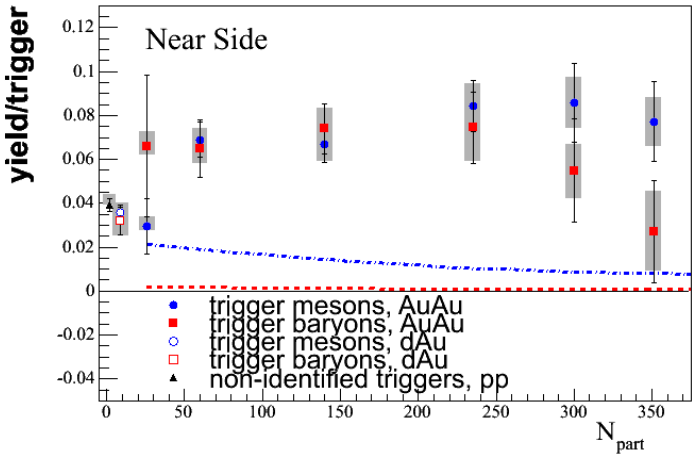

Figure 6.1: Conditional yield on the near side (the data are the same as in Figure 5.2. The curves are the expectation of purely thermal recombination based on the fraction of particles from recombination in Figure 1.14 [32]. Dot-dashed line (blue) is for trigger mesons and dashed line (red) is for trigger baryons.

Clearly, both curves are excluded by the data. Additionally, the centrality dependence of the curves is different than the data; no normalization constant would bring the curves into agreement with the data.

6.2 Beyond Thermal Recombination

Purely thermal recombination does not agree with the data, but this simple picture ignores all correlations except for elliptic flow and has no mechanism to explain the intersection of hard and soft physics at intermediate p_T . Several hybrid recombination and jet models have been proposed [34, 33, 57] which apply recombination to more realistic scenarios. The simplest of these "hard-soft" recombination models is [34] where a hard scattered quark or anti-quark either fragments normally or recombines with quark and anti-quarks from the

thermal part of the event to form final state hadrons. The next extension of this idea is Shower Parton recombination [33] where the quarks and anti-quarks from the fragmentation of a hard scattered parton are allowed to recombine with each other or with quarks and anti-quarks from the thermal medium. In the limit that the thermal source vanishes normal fragmentation, as in $e^+ + e^-$ collisions is recovered. In the final model [57] jet partons interacting with the medium create a localized hot spot which recombines, but the particles are correlated.

6.2.1 Shower Parton Recombination

While the idea of a large thermal source does not apply to peripheral Au+Au, d+Au, and p+p collisions, a blend of recombination and fragmentation has been proposed which is applicable to all three systems [33, 58]. Basically, as a parton fragments it creates quark/anti-quark pairs which then recombine to form final state hadrons. All quarks are available for recombination, those from the thermal source (if present) and those from the fragmentation of jets. In this way traditional fragmentation can be explained in terms of recombination of quarks and gluons from the radiated gluons. This type of fragmentation is very similar to that in the Herwig [59] event generator.

In the shower parton recombination model quarks and anti-quarks are classified as either "thermal", those which come from the thermal source and "shower", those which are associated with a hard scattering. Mesons produced in this model are either "thermal-thermal", those coming from the recombination of two thermal quarks and anti-quarks, "shower-shower" those coming

from quarks and anti-quarks associated with a hard scattering, and "thermal-shower", where one quark or anti-quark is from the thermal source and the other is associated with a hard scattering. Thermal-thermal mesons are the same as in purely thermal recombination. Shower-shower mesons come in two types: those where the quark and anti-quark are associated with the same jet (1-jet) and those where the quark and anti-quark are associated with different jets (2-jet). The 1-jet shower-shower mesons are the same as in normal fragmentation. 2-jet mesons are rare at RHIC energies, but would become important if the jet multiplicity were sufficiently high.

Figure 6.2 from [58] shows the π^0 spectrum as calculated in the shower parton recombination model (solid line) compared with the PHENIX data from [60] for central Au+Au collisions. The other lines show the contribution to the total from the various recombination types. At low p_T ($<$3GeV/c) thermal-thermal recombination dominates. Thermal-shower recombination dominates from 3$<$ p_T $<$8GeV/c . For p_T $>$8GeV/c shower-shower production from a single jet, normal fragmentation, dominates. Shower-shower production from two jets is not expected to be important at all. The calculation agrees reasonably well with the data.

Baryon production in the shower parton recombination model again occurs between shower and thermal quarks or anti-quarks. There are more different combinations than in meson production. Figure 6.3 from [58] shows a calculation of the proton spectra in central Au+Au collisions compared to the PHENIX data [26] with the various contributions to the proton yield shown with the different lines. Recombination of three thermal quarks (dashed line) is expected to dominate until p_T $<$5GeV/c . At higher p_T , correlations be-

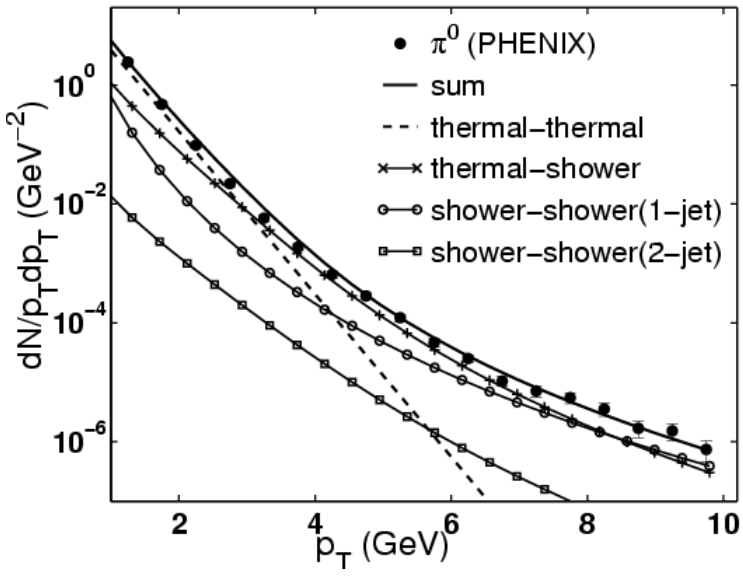

Figure 6.2: Expected contributions to the pi^0 spectrum in central Au+Au collisions from [58]. The dominant contributions are the recombination of two quarks from the thermal source (dashed line) and one thermal quark with one quark from a hard scattering (crosses). The data points are from [60].

come important. Recombination of one thermal quark with two shower quarks from a single jet (dot-dashed line) dominates for 5< p_T <9GeV/c . At higher p_T , normal fragmentation (solid line with square points) dominates.

The shower recombination model has also been applied to d+Au collisions. "Thermal" quarks and anti-quarks, from soft scattering, are still expected to play an important role in particle production at intermediate p_T . In central d+Au collisions the majority of both pions and protons are expected to contain at least one thermal quark for p_T < 3.0GeV/c [37, 38] as can be seen in Figures 6.4 and 6.5. In peripheral d+Au collisions, where the average number of binary collisions is ≈3, the protons are dominated by recombination out to ≈2.5GeV/c, suggesting recombination plays only a slightly less significant role than in central d+Au collisions.

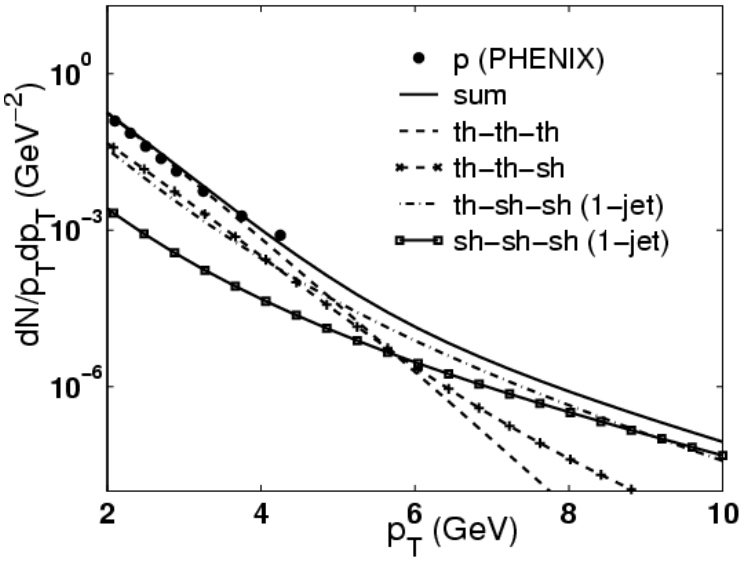

Figure 6.3: Expected contributions to the proton spectrum in central Au+Au collisions from [58]. The dominant contributions are the recombination of three quarks from the thermal source (dashed line) at low p_T and at least one thermal quark with one or two quarks from a single hard scattering (crosses and dot-dashed respectively). The data points are from [26].

The Cronin effect [61] is the enhancement of the particle yields beyond binary scaling in p (or d)-nucleus collisions. At RHIC energies the Cronin enhancement is found to be greater for protons and anti-protons than pions [62, 40]. The agreement between the data and the calculations in Figures 6.4 and 6.5 provides a possible explanation for this. Two particle correlation measurements are needed to further understand if recombination models are applicable in d+Au collisions.

Conditional yields at intermediate p_T have not been calculated for Au+Au or d+Au and provide a much more sensitive test of the possible modifications to fragmentation suggested by shower parton recombination. Comparisons with the data are essential to understanding the validity of this model.

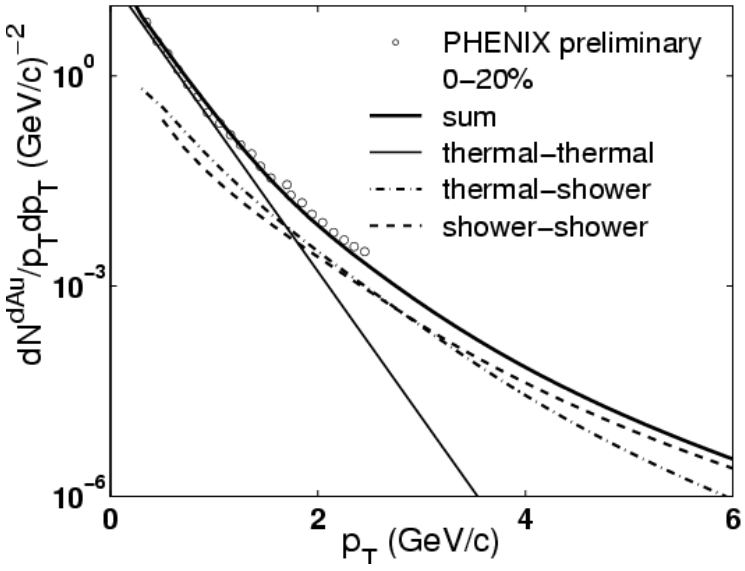

Figure 6.4: Expected contributions to the pion spectrum in central d+Au collisions from [37]. The thin solid line indicates the contribution only from the thermal source, the dot dashed lines show the contribution from thermal-shower mixture and the dashed lines the protons from only shower quarks. The data are from [28].

6.2.2 Recombination from a Correlated Thermal Source

An enhancement to the traditional recombination models that has been recently proposed is the inclusion of correlations in the thermal source beyond elliptic flow [57]. A possible mechanism for creating these correlations is energy loss of a hard parton via medium induced gluon radiation. The radiated gluons create a region of increased temperature and gluon density along the jet path. These extra gluons eventually become extra final state hadrons. The spatial correlation among these hadrons is amplified according to the valence quark number in the same manner elliptic flow correlations are; baryon-baryon correlations are the most amplified and meson-meson correlations are the least amplified. An initial calculation of correlated source recombination found

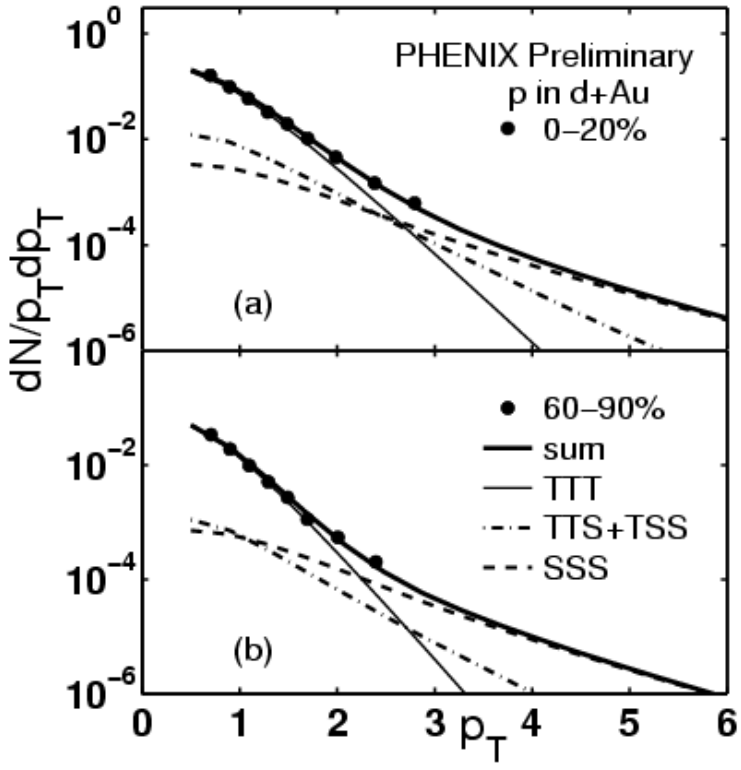

Figure 6.5: Expected contributions to the proton spectrum in central (top panel) and peripheral (bottom panel) d+Au collisions from [38]. The thin solid lines indicate the contribution only from the thermal source, the dot dashed lines show the contribution from thermal-shower mixture and the dashed lines the protons from only shower quarks. The data are from [28].

that both the correlations due to recombination and those due to fragmentation were important in understanding hadron formation at intermediate p_T in Au+Au collisions [57].

Figure 6.6(b) shows the yield of additional lower p_T particles which accompany each $2.5 < p_T < 4.0 \mathrm{GeV}/c$ baryon or meson (Y_{AB}) as a function of N_{part}. The squares show the yield from pure fragmentation and the black diamonds show the yield from recombination of the correlated thermal source. Meson triggers have some correlations from the thermal source ($Y_{AB} \approx 0.3$),

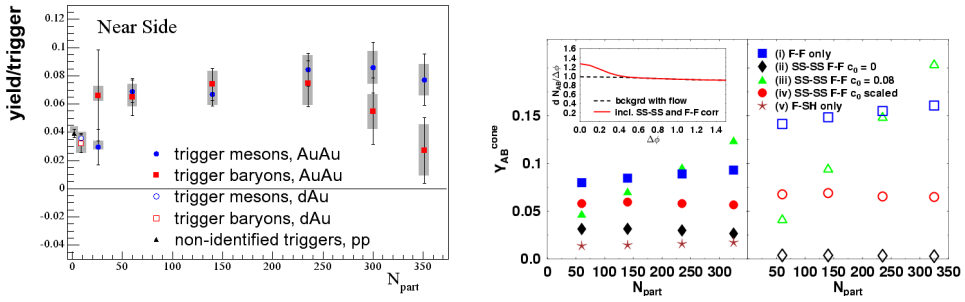

(a) data from Figure 5.2 (b) calculation from [57]

Figure 6.6: (a) Top panel of Figure 5.2 showing the near side conditional yields as a function of N_{part} for the Run 2 and 3 analysis in p+p, d+Au and Au+Au collisions. (b) Y_{AB} (see text) for charged hadrons with 1.7< p_T <2.5GeV/c associated with mesons (left panel) and baryons (right panel) with 2.5< p_T <4.0GeV/c. Blue squares show the contribution from pure fragmentation and the black diamonds show the contribution from recombination from the soft correlated source. Red circles indicate the authors best calculation for the combined observable Y_{AB} value. For the other points see [57].

but baryon triggers have essentially no correlations from the thermal source. This is strange because correlations involving a baryon should be higher than correlations involving a meson due to the quark number scaling. All of the correlations from baryon triggers then must come from fragmentation.

The red circles in Figure 6.6(b) are directly comparable to Figures 5.2 (top panel, which is reproduced as Figure 6.6(a)) and Figure 5.8. The calculation agrees well with the data, except for the decrease in baryon triggered yields in the most central collisions. The fragmentation estimation (blue squares) seems quite high in comparison with the p+p and d+Au data in 5.2 where thermal sources should be less important than in Au+Au. The approach is interesting, but without calculations for p+p and d+Au which also reproduce the data it is unconvincing.

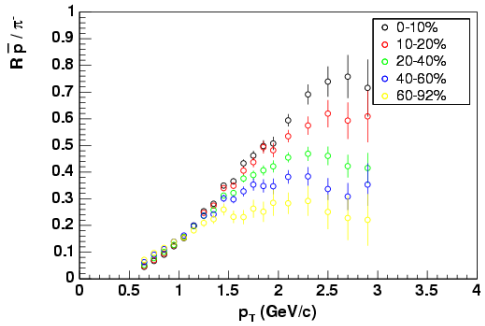

Figure 6.7: $\bar{p}/\pi^-$ ratio as a function of p_T in Au+Au collisions in five centralities. The data are taken from [26].

6.3 Upper Limit to Thermal Baryon Production

A simple data based toy model can be used to understand the sensitivity of associated yield measurements to changes in the jet structure of the baryon excess. If the source of the baryon excess is purely thermal (non-jet) source it is possible to predict the yield of associated particles per trigger based on the observed change in the $\bar{p}/\pi^-$ ratio with centrality (the $\bar{p}/\pi^-$ ratio is used because all $\bar{p}$ are produced in the collision). A change in the $\bar{p}/\pi^-$ ratio from the normal fragmentation value observed in p+p collisions would indicate additional baryon and anti-baryon production by a thermal source and would dilute the yield of associated particle per trigger. The $\bar{p}/\pi^-$ ratio for various centralities is shown in Figure 6.7 [26].

The dilution of baryons from fragmentation by those from a thermal source is described by:

$$\frac{\bar{p}}{\pi} = \frac{f_b + r_b}{f_\pi}$$

where f_b and f_π are constant and $\frac{f_b}{f_\pi}$ is the $\bar{p}/\pi \approx 0.25$ ratio in peripheral Au+Au collisions where the assumption is that all $\bar{p}$ come from fragmentation. The $\bar{p}/\pi^-$ ratio in peripheral Au+Au collisions is actually slightly higher than in p+p collisions, but this does not change the conclusions drawn here. r_b is the additional $\bar{p}$ which come from the thermal source.

Realistic recombination type models assume that mesons, as well as baryons, are formed by thermal processes. This model, by allowing no thermal meson production, keeps the baryon and anti-baryon production by thermal processes at a minimum and thus represents a lower limit on the dilution of the jet associated yield per baryon and anti-baryon trigger.

Table 6.1 shows the fraction of baryons and anti-baryons from fragmentation as a function of N_{part} under the assumptions of this model. All other baryons and anti-baryons are assumed to be from some thermal source.

N_{part}	$\frac{f_p}{f_p+r_p}$
325	0.34
234	0.41
140	0.54
60	0.76
22	1.00

Table 6.1: Fraction of baryons and anti-baryons from fragmentation as a function of N_{part} under the toy model assumption.

In order to compare the assumptions in this model to the data we need to normalize to the normal fragmentation yield of associated particle per baryon trigger. Because the peripheral Au+Au data points for both trigger types have large statistical errors we have normalized to the p+p yield in Figure 5.2 (the top panel of which is reproduced as Figure 6.8). The absolute values of the

model curve differs from the results at all centralities except the most central. It is also clear that even if the normalization was determined differently, the centrality dependence of the model curve is incompatible with the data. The Run 4 analysis (Figure 5.8) confirms the conclusion of the Run 2 analysis. Thus, the source of baryons and anti-baryons must be a mechanism which yields partners per trigger, a jet-like mechanism.

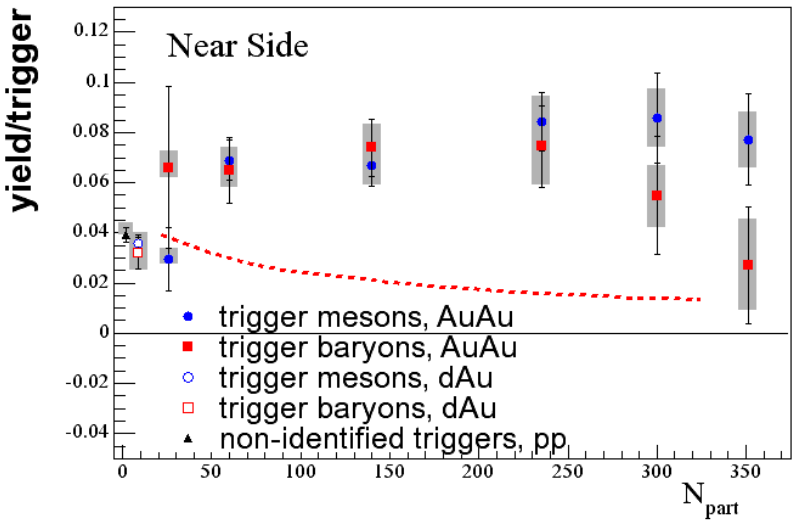

Figure 6.8: Near side associated yields for trigger baryons and mesons as a function of N_{part} from the Run 2 analysis with the toy model calculation described in the text (dashed red line). Data is the same as the top panel of Figure 5.2.

Centrality	χ^2/DOF meson triggers	χ^2/DOF baryon triggers
0-5%	0.89	1.10
5-10%	0.84	0.66
10-20%	2.00	2.51
20-40%	1.17	1.19
40-60%	0.56	2.24
60-70%	1.10	0.79

Table 6.2: χ^2 per degree of freedom between the curves and data points in Figure 6.9. In all cases there are six degrees of freedom. Table is from [63].

6.4 Jet Widths in Au+Au Collisions

The widths of the near side jets observed in Au+Au collisions in this analysis are consistent, within errors, with what is predicted based on the measured j_T from p+p collisions (see Section 5.1.3). Figure 6.9 [63] shows the $\frac{1}{N_{trig}}\frac{dN}{d\Delta\phi}$ distributions from Figure 5.1 with near side jet shape calculated from the conditional yield and assuming that j_T remains constant in Au+Au collisions with centrality. The χ^2/DOF values for the comparison between the calculation and the data points is shown in Table 6.2. The χ^2/DOF values are reasonable, ruling out a strong modification of the near side jet shape in this p_T range. Additionally, there is no strong difference between the baryon and meson triggered jet shapes.

6.5 Comparison to PYTHIA

Right now we do not have p+p conditional yield results for any correlations where either particle is identified. We use PYTHIA [10] generated p+p events at $\sqrt{s}$=200GeV as a baseline instead. For this study approximately 57M hard scattering PYTHIA collisions were created. The same p_T ranges for trigger

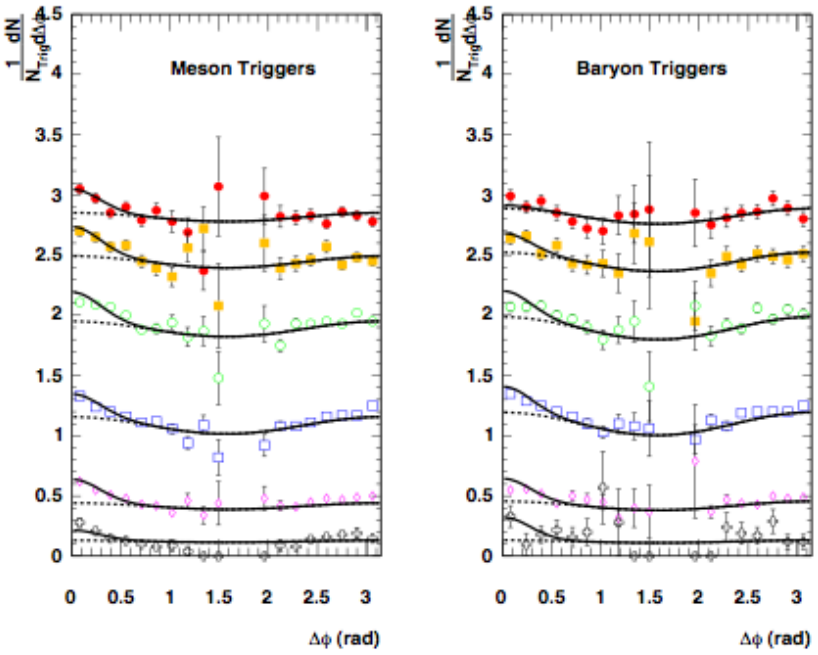

Figure 6.9: Data points are the same as in Figure 5.1. Solid lines are the combinatoric level modulated by v_2 plus the near side jet shape calculated from the jet width from the constant j_T assumption and the near side conditional yields in 5.2. The level of agreement between the curves and the data points is shown in Table 6.2. Figure is from [63].

and partner particles were used as in the analysis of the real data. Particles used were required to be charged hadrons ($\pi^{\pm}$, $K^{\pm}$, p and $\bar{p}$) and within the PHENIX η acceptance ($|\eta|$ <0.35). The PHENIX azimuthal acceptance was not imposed because the final data analysis corrects for it. The analysis procedure was the same as for the real analysis and the combinatoric background level was calculated by the $\langle triggers \rangle \langle partners \rangle$ normalization. The $\frac{1}{N_{trig}} \frac{dN}{d\Delta\phi}$ distributions are shown in Figures 6.10 (charged hadron partners), 6.11 (identified baryon or meson partners) and 6.12 (identified proton/anti-proton triggers and partners). In all figures the combinatoric background level (dashed line)

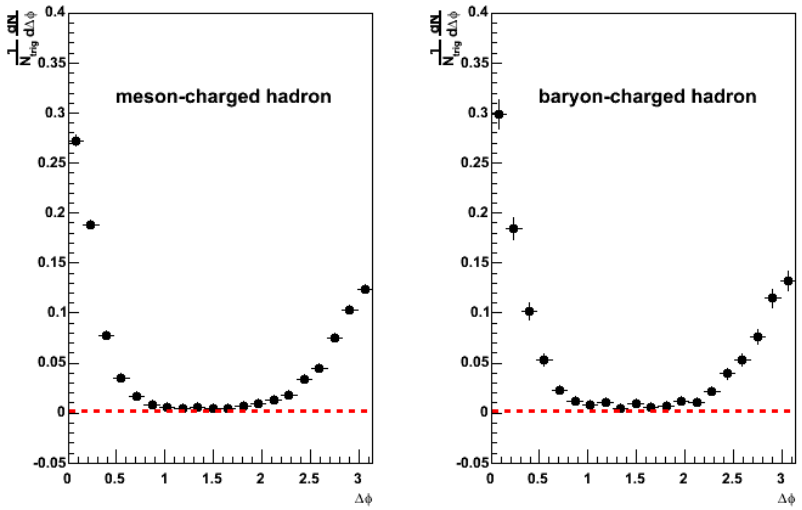

Figure 6.10: Unsubtracted $\frac{1}{N_{trig}}\frac{dN}{d\Delta\phi}$ distribution from PYTHIA p+p events. Triggers are from 2.5< p_T <4.0GeV/c and partners are from 1.7< p_T <2.5GeV/c . The dashed lines show the calculated combinatoric background levels. Conditional yields are shown in Tables 6.3 (near side) and 6.4 away side.

is very small compared to the signal.

Tables 6.3, 6.4, 6.5, 6.6, 6.7 and 6.8 show the conditional yields for the PYTHIA analysis integrated over the same angular range as the data, 0< $\Delta\phi$ <0.94rad for the near side and 2.2< $\Delta\phi$ < πrad for the away side. Also in the Tables are the peripheral (60-90%) Au+Au conditional yields from the Run 4 analysis for the corresponding particle type combinations and the difference between the data and PYTHIA in terms of the statistical σ on the data.

The quantitative disagreement between the data and PYTHIA is not especially worrisome. PYTHIA has not been tuned to the correlations data at this energy. Here we are concerned with whether the qualitative features of the particle type dependence of the near side correlations are the same in PYTHIA

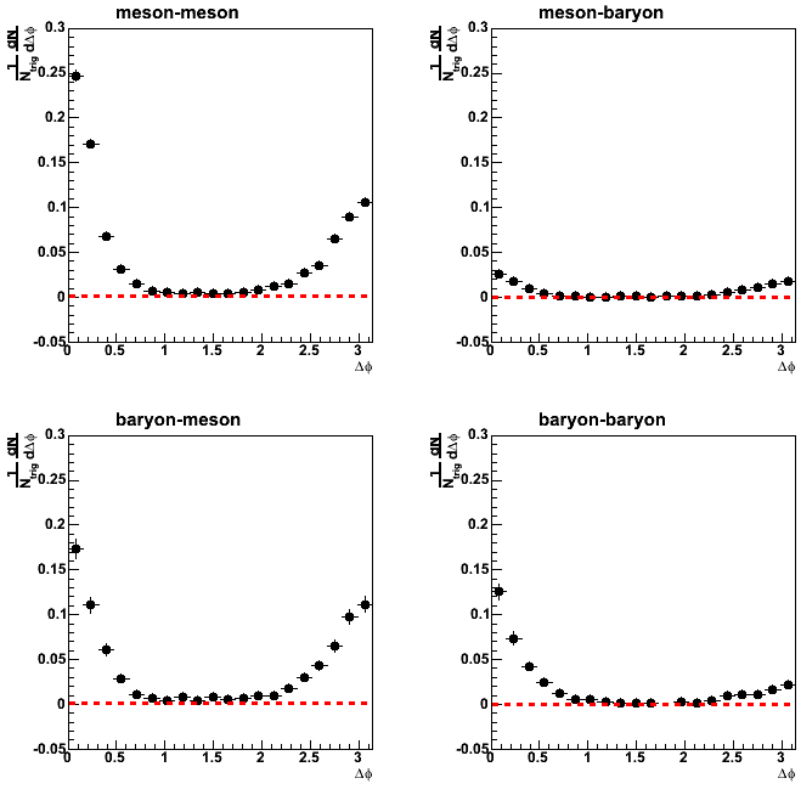

Figure 6.11: Unsubtracted $\frac{1}{N_{trig}}\frac{dN}{d\Delta\phi}$ distribution from PYTHIA p+p events. Triggers are from 2.5< p_T <4.0GeV/c and partners are from 1.7< p_T <2.5GeV/c . The dashed lines show the calculated combinatoric background levels. Conditional yields are shown in Tables 6.3 (near side) and 6.4 away side.

Trigger Type	Partner Type	DATA Conditional Yield	PYTHIA Conditional Yield	Difference σ
meson	charged hadron	0.054 ± 0.002	0.0921 ± 0.0003	19
baryon	charged hadron	0.050 ± 0.002	0.1039 ± 0.0008	27

Table 6.3: Near side conditional yield measurements from 60-90% centrality Au+Au data and PYTHIA for trigger particles from 2.5< p_T <4.0GeV/c and partner particles from 1.7< p_T <2.5GeV/c .

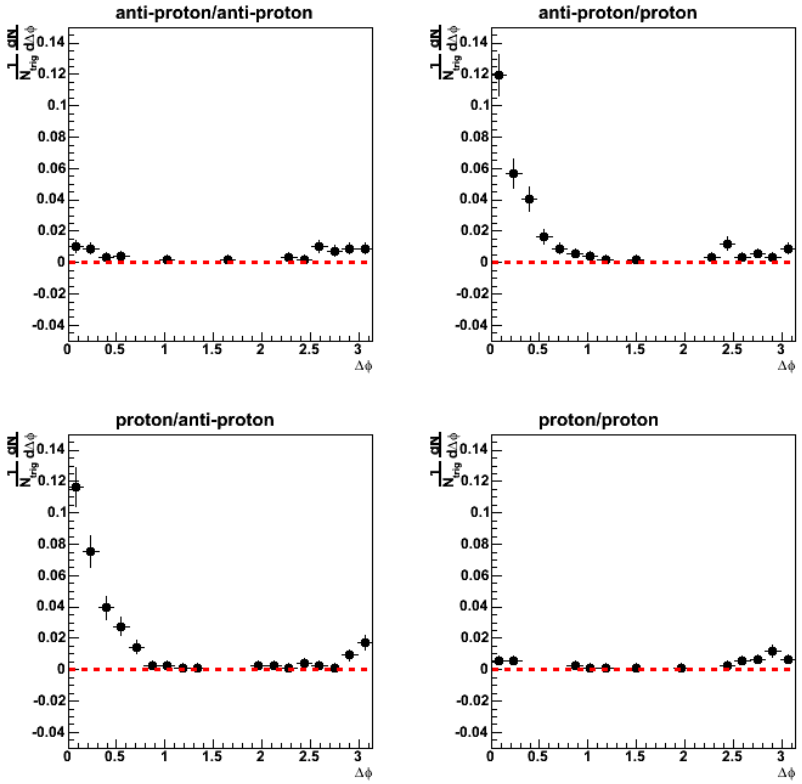

Figure 6.12: Unsubtracted $\frac{1}{N_{trig}}\frac{dN}{d\Delta\phi}$ distribution from PYTHIA p+p events. Triggers are from 2.5< p_T <4.0GeV/c and partners are from 1.7< p_T <2.5GeV/c . The dashed lines show the calculated combinatoric background levels. Conditional yields are shown in Tables 6.3 (near side) and 6.4 away side.

and the Au+Au data. For this comparison the ratio of the data to PYTHIA should be sufficient.

Figure 6.13 shows the near side ratio of partner baryon to mesons for both the data and PYTHIA for meson and baryon triggers. Only statistical errors are shown on the data. The data show no significant centrality or trigger dependence. PYTHIA jets have a much higher baryon to meson ratio for baryon triggered jets than. The origin of this discrepancy is not understood. It is puzzling that the jets at intermediate p_T in mid-central and central Au+Au collisions have a greatly increased probability to have a baryon trigger, but the partner composition is not significantly changed from the meson triggered jets.

Figure 6.14 shows the away side baryon to meson ratio as a function of centrality for trigger baryons, trigger mesons and PYTHIA. The error bars on the data are large, and there is no significant difference between the data and PYTHIA.

Values of the ratio of the data to PYTHIA for p and $\bar{p}$ correlations are shown in Table 6.9. Within the large statistical errors, which are dominated by the statistical errors on the data, the ratio of the data to PYTHIA is consistent for all four trigger and partner combinations. Thus, in peripheral Au+Au collisions the data is in agreement with fragmentation via string breaking. Baryon and anti-baryon pairs are likely to be found on the same side jet in both PYTHIA and Au+Au collisions, rather than baryon number conservation in the di-jet pair. The lack of centrality dependence in the data for these correlations (see Figure 5.18) implies that the baryon fragmentation on the near side is not significantly modified even in central Au+Au collisions from

p+p collisions.

Trigger Type	Partner Type	DATA Conditional Yield	PYTHIA Conditional Yield	Difference σ
meson	charged hadron	0.035 ± 0.002	0.060 ± 0.001	12
baryon	charged hadron	0.050 ± 0.004	0.067 ± 0.003	4.3

Table 6.4: Far side conditional yield measurements from 60-90% centrality Au+Au data and PYTHIA for trigger particles from 2.5< p_T <4.0GeV/c and partner particles from 1.7< p_T <2.5GeV/c .

Trigger Type	Partner Type	DATA Conditional Yield	PYTHIA Conditional Yield	Difference σ
meson	meson	0.042 ± 0.005	0.083 ± 0.001	8.2
baryon	meson	0.014 ± 0.004	0.060 ± 0.003	12
meson	baryon	0.005 ± 0.002	0.0090 ± 0.0004	2.0
baryon	baryon	0.010 ± 0.004	0.044 ± 0.002	8.5

Table 6.5: Near side conditional yield measurements from 60-90% centrality Au+Au data and PYTHIA for trigger particles from 2.5< p_T <4.0GeV/c and partner particles from 1.7< p_T <2.5GeV/c .

Trigger Type	Partner Type	DATA Conditional Yield	PYTHIA Conditional Yield	Difference σ
meson	meson	0.014 ± 0.004	0.051 ± 0.001	9.3
baryon	meson	0.012 ± 0.006	0.056 ± 0.003	7.3
meson	baryon	0.005 ± 0.002	0.0090 ± 0.0004	2.0
baryon	baryon	0.003 ± 0.003	0.011 ± 0.001	2.7

Table 6.6: Far side conditional yield measurements from 60-90% centrality Au+Au data and PYTHIA for trigger particles from 2.5< p_T <4.0GeV/c and partner particles from 1.7< p_T <2.5GeV/c .

Trigger Type	Partner Type	DATA Conditional Yield	PYTHIA Conditional Yield	Difference σ
$\bar{p}$	$\bar{p}$	-0.001 ± 0.002	0.004 ± 0.001	2.5
$\bar{p}$	p	0.009 ± 0.004	0.039 ± 0.003	7.5
p	$\bar{p}$	0.006 ± 0.002	0.043 ± 0.003	19
p	p	0.000 ± 0.002	0.0019 ± 0.0007	0.95

Table 6.7: Near side conditional yield measurements from 60-90% centrality Au+Au data and PYTHIA for trigger particles from 2.5< p_T <4.0GeV/c and partner particles from 1.7< p_T <2.5GeV/c .

Trigger Type	Partner Type	DATA Conditional Yield	PYTHIA Conditional Yield	Difference σ
$\bar{p}$	$\bar{p}$	0.0003 ± 0.002	0.006 ± 0.001	2.9
$\bar{p}$	p	0.002 ± 0.002	0.005 ± 0.001	1.5
p	$\bar{p}$	0.003 ± 0.002	0.005 ± 0.001	1.0
p	p	0.004 ± 0.002	0.005 ± 0.001	0.50

Table 6.8: Far side conditional yield measurements from 60-90% centrality Au+Au data and PYTHIA for trigger particles from 2.5< p_T <4.0GeV/c and partner particles from 1.7< p_T <2.5GeV/c .

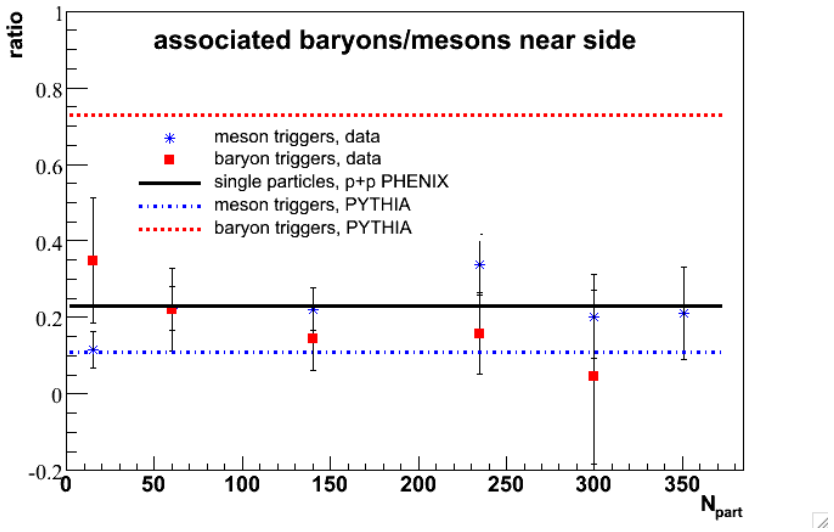

Figure 6.13: Associated baryon to meson ratio for near side correlations in Au+Au and PYTHIA. The Au+Au points come from Figures 5.11 and 5.14, errors are statistical only. The solid black line shows the baryon to meson ratio for single identified charge particles as measured in PHENIX [40]. No feed-down correction is applied.

Trigger Type	Partner Type	Ratio
$\bar{p}$	$\bar{p}$	-0.25 ± 0.50
$\bar{p}$	p	0.23 ± 0.10
p	$\bar{p}$	0.14 ± 0.05
p	p	0.00 ± 1.0

Table 6.9: Ratio of near side conditional yields in peripheral Au+Au data to PYTHIA from Table 6.7. Errors are statistical only.

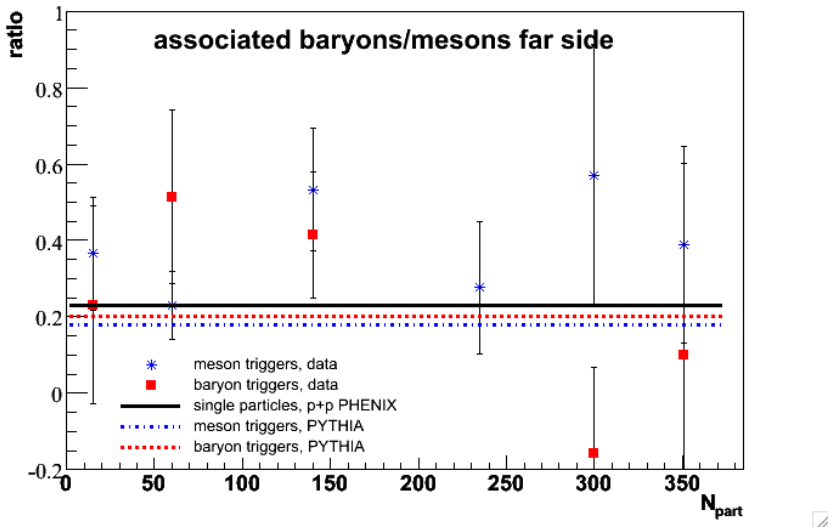

Figure 6.14: Associated baryon to meson ratio for far side correlations in Au+Au and PYTHIA. The Au+Au points come from Figures 5.12 and 5.15, errors are statistical only. The solid black line shows the baryon to meson ratio for single identified charge particles as measured in PHENIX [40]. No feed-down correction is applied.

Chapter 7

Conclusions

In the analyses presented here we have attempted to understand the source of the baryon excess in central Au+Au collisions using two- particle azimuthal correlations in Au+Au, d+Au and p+p collisions. We have studied the conditional yields of partners per trigger as a function of the trigger and partner type and the collision centrality in Au+Au. The results have been compared to recombination models and PYTHIA.

7.1 Baryons Come from Jets

The data presented show that the primary source of the baryon excess observed in Au+Au collisions is a jet like mechanism. The non-zero yield of associated particles per trigger shown in Figures 5.8 and 5.5 for baryon triggers means that whatever production mechanism creates the baryons also creates particles nearby in $\Delta\phi$ and around $\Delta\phi = \pi$ in a manner characteristic of jet fragmentation. Additionally, the similarity between the baryon and meson triggered

yields on both the near and away side suggests that whatever influence the medium in Au+Au collisions has on the jets does not depend on the trigger type except in the most central collisions. The rate of baryon triggered jets follows binary scaling, but the jets themselves interact with the medium in the same way meson triggered jets do. This is not surprising since the associated particles are the same in both cases and should fragment independently of the trigger hadron.

As was discussed in Section 6.3, some process lowers the associated yields for baryon triggered correlations in the most central 10% Au+Au collisions. But, because of the magnitude and the centrality dependence, it cannot account for the entire baryon excess. Additionally, in Figure 5.9 there is no significant difference between the baryon and meson triggered away side associated yields. This is consistent with a scenario where the near side fragmentation is modified to produce extra baryons and a reduced yield per trigger in the p_T ranges measured here, but where the underlying hard scattering, and thus the away side jet, is the same for both baryon and meson triggers. If that is the case, at some partner p_T range the baryon triggered associated yields must be greater than the meson triggered yields to include the missing p_T in the p_T range measured here. Higher statistics measurements over a broad partner p_T range are needed to address this question.

Figures 5.10, 5.11, 5.12, 5.13, 5.14 and 5.15 where both particles are identified as baryons or mesons further support the conclusion that the baryon excess arises from a jet-like source. The only significant difference between baryon and meson triggers is the decrease in the baryon triggered associated meson yields for the most central collisions, as is seen for charged hadron

partners (Figures 5.8 and 5.2). A strong dependence on the partner type is seen, as is expected from fragmentation. The near and away side yields for baryon partners are lower than the corresponding yields for meson partners, independent of whether the trigger is a baryon or a meson.

7.2 Jets in Au+Au Collisions are Modified Compared to p+p

The present results clearly show that jets at intermediate p_T in mid-central and central Au+Au collisions are strongly modified compared to jets in d+Au and p+p collisions. The conditional yield of particles per trigger in Au+Au collisions is nearly one and a half times the value in d+Au and p+p collisions (see Figure 5.2). The associated particle p_T slopes are similar for all centralities, perhaps decreasing somewhat for more central collisions. Thus, the total number of associated particles and the total amount of associated momentum per trigger particle is approximately one and a half times greater in Au+Au than in p+p and d+Au collisions. The simplest explanation for the origin of this excess is the trigger particle losing energy in the medium. There should be more associated particles because the total average jet energy is higher than for a similar p_T trigger in p+p collisions. Additionally, there should be extra particles created by the gluons radiated by the trigger particle losing energy. Unfortunately, quantitative calculations of these effects on conditional yield measurements and their particle type dependence at intermediate p_T have not been done.

The jet width in $\Delta\phi$ does not change significantly from p+p to central Au+Au collisions, as would be expected if the jet were escaping from the collision region without having interacted much with the medium, but the conditional yields do increase significantly and jet fragmentation produces many more baryons than is expected from normal fragmentation. Thus, there must be significant interaction of the jet particles with the medium.

It is not yet understood how exactly the jets are modified by the medium. Recombination models are an easy way to conceptualize the jet modification, but there is no clear and convincing recombination picture that quantitatively describes the data at this point. Recombination covers a broad enough range of physics that the flaws in the current calculations do not doom the entire concept. The v_2 scaling with constituent quark number [31] is strong evidence that recombination indeed occurs.

In order for a theoretical model to satisfactorily explain the origin of baryon excess it should be able to reproduce the data already measured in Au+Au collisions and be able to predict the data in Cu+Cu collisions for a variety of p_T selections and particle combinations.

7.3 Future Measurements

The analysis presented here demonstrates conclusively that the baryon excess observed in central Au+Au collisions at $\sqrt{s_{NN}}$=200GeV has a jet origin. It also demonstrates that recombination from an uncorrelated thermal source is not able to explain baryon or meson production at intermediate p_T . Further measurements are necessary to understand the evolution of jets with the colli-

sion system and centrality and to understand what, if any, role recombination scenarios play in particle production. There must be some manifestation of the baryon excess in two particle correlation observables since the baryons are being produced via a jet like mechanism.

The most obvious next analysis involves measuring the conditional yields for identified triggers as a function of trigger p_T . The p_T range used in the present analysis is where the baryon excess has reached its peak value (see Figure 1.11). Both higher and lower trigger p_T values would be useful. Higher p_T triggers are possible with a large enough dataset; the PHENIX TOF resolution does not allow K/p separation after $\approx$4.0GeV/c , but with an asymmetric cut allowing only higher mass protons and anti-protons it would be possible to look at identified baryon triggers with p_T out to $\approx$4.5-5.0GeV/c where the p/π ratio returns to its p+p value. It might be possible to use the PHENIX Aerogel to identify baryon triggers with a veto; kaons begin to fire the aerogel at p =3.3GeV/c and protons begin to fire at p =6.2GeV/c . It is as yet unclear whether a veto in the aerogel could give a clean enough trigger sample in a high multiplicity environment. Trigger mesons are possible at all p_T with the direct reconstruction of decayed π^0s in the EMCal. Lower p_T triggers, p_T $\approx$2.0GeV/c will contain a much greater soft component making the jet correlations harder to see, but with sufficient statistics a measurement should be possible.

Another extension which will be possible with an increase in statistics is lower partner p_T . Again, the jet signal would be diluted by the increased contribution of soft particles. Also, the measurement is complicated by contamination from resonance decays which can create non-jet trigger/partner

pairs. These problems can be overcome. The inclusion of lower p_T partner particles would offer a more complete view of the jet and could be more sensitive to interactions between the jet and the medium.

The system and energy dependence of the associated yields are also of interest; both Au+Au collisions at $\sqrt{s_{NN}}$=62.4GeV and Cu+Cu collisions at $\sqrt{s_{NN}}$=200GeV show increased $\frac{p}{\pi^+}$ and $\frac{\bar{p}}{\pi^-}$ ratios in the intermediate p_T region in central collisions compared to p+p and d+Au collisions (Figures 7.1 and 7.2). In these systems it would be useful to separate p triggers from $\bar{p}$ triggers because the higher $\frac{p}{\pi^+}$ ratio compared to $\frac{\bar{p}}{\pi^-}$ ratio in central collisions means that a large number of the protons are not produced in the collision, but come from the baryon number carried by the incoming nucleus. Two particle correlations of identified particles in these systems would help understand how the fragmentation is modified in heavy ion collisions.

Complete understanding of the hadronization process at intermediate p_T in heavy ion collisions will require both jet studies with comprehensive particle identification and p_T selections and a believable theoretical model in which the results can be interpreted. This work has shown that the fragmentation process is modified in heavy ion collisions in a manner that is not explicable in current models. In order to establish a solid baseline for these measurements the same studies must be done in a control system such as p+p collisions at the same energy. The p+p data taken in Run 5 should be sufficient for these studies. The PYTHIA comparisons made here are not a long term substitute for experimental data.

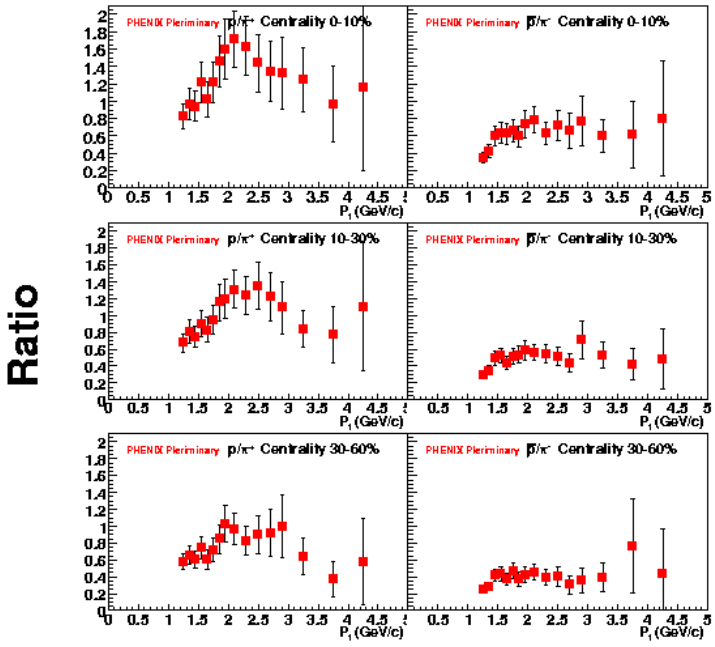

Figure 7.1: $\frac{p}{\pi^+}$ (left) and $\frac{\bar{p}}{\pi^-}$ (right) ratio in $\sqrt{s_{NN}}$=62.4GeV Au+Au collisions as a function of p_T . Errors are statistical. No feed down correction is applied. Figure is from [64].

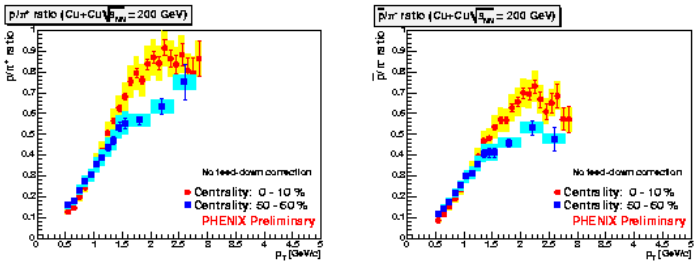

Figure 7.2: $\frac{p}{\pi^+}$ (left) and $\frac{\bar{p}}{\pi^-}$ (right) ratio in $\sqrt{s_{NN}}$=200GeV Cu+Cu collisions as a function of p_T . Central (red circles) and peripheral (blue squares) collisions are shown. No feed down correction is applied. Figure if from [64].

Bibliography

[1] F Karsch. Lattice Results on QCD Thermodynamics. *Nucl Phys*, A698:199–208, 2002.

[2] J D Bjorken. Highly Relativistic Nucleus-Nucleus Collisions: The Central Rapidity Region. *Phys. Rev.*, D27:140, 1983.

[3] K Adcox et al. Formation of dense partonic matter in relativistic nucleus-nucleus collisions at RHIC: Experimental evaluation by the PHENIX collaboration. *Nucl. Phys.*, A757:184–283, 2005, nucl-ex/0410003.

[4] S. S. Adler et al. Systematic studies of the centrality and $\sqrt{s_{NN}}$ dependence of the $dE_T/d\eta$ and $dN_{ch}/d\eta$ in heavy ion collisions at midrapidity. *Phys. Rev.*, C71:034908, 2005, nucl-ex/0409015.

[5] R Glauber and J. Nathiane. High Energy Scattering of Protons by Nuclei. *Nucl. Phys.*, B21:135, 1970.

[6] Klaus Reygers. Glauber Monte Carlo Calculations for Au+Au Collisions at $\sqrt{s_{NN}}$=200GeV.

[7] Gross D J and Wilczek F. Asymptotically free gauge theories 1. *Phys. Rev.*, D8:3633–3652, 1973.

[8] S. Eidelman et al. The Review of Particle Physics. *Phys. Lett.*, B592:1, 2004.

[9] G Sterman. Introduction to the Parton Model and Perturbative QCD, CTEQ Summer School 2004.

[10] T. Sjoestrand et al. High-Energy-Physics Event Generation with PYTHIA 6.1. *Comp. Phys. Comm.*, 135:238, 2001.

[11] H Aihara et al. Baryon Production in $e^+ + e^-$ Annihilation at $\sqrt{s}$=29GeV: Clusters or Diquarks? *Phys. Rev. Lett.*, 55:1047, 1985.

[12] H Aihara et al. Study of Baryon Correlations in $e^+ + e^-$ Annihilation at 29GeV.

[13] Abreu P et al. Rapidity Rank Structure of p and $\bar{p}$ Pairs in Hadronic Z^0 Decays. *Phys. Lett.*, B490:61, 2000.

[14] Hanson G et al. Evidence for Jet Structure in Hadron Production by $e^+ + e^-$ Annihilation. *Phys. Rev. Lett.*, 35:1609–1612, 1975.

[15] A.L.S Angelis et al. A Measurement of the Transverse Momenta of Partons, and of Jet Fragmentation as a Function of $\sqrt{s}$ in p+p Collisions. *Phys. Lett.*, B97:163, 1980.

[16] F Abe et al. Topology of three-et events in p-$\bar{p}$ collisions at $\sqrt{s}$=1.8TeV. *Phys. Rev.*, D45:1448–1458, 1992.

[17] R Akers et al. QCD Studies Using a Cone Based Jet Finding Algorithm for $e^+ + e^-$ Collisions at LEP. *Z. Phys.*, 63:197–212, 1994.

[18] S Catani et al. New Clustering Algorithm for Multi-Jet Cross Sections in $e^+ + e^-$ Annihilation. *Phys. Lett.*, B269:432–438, 1991.

[19] OPAL Collaboration. A Model Independent Measurement of Quark and Gluon Jet Properties and Differences. *Z. Phys.*, 68:179–202, 1995.

[20] OPAL Collaboration. Experimental Properties of Gluon and Quark Jets from a Point Source. *Eur. Phys. J.*, C11:217, 1999.

[21] Brodsky S J and Gunion J F. Hadron Multiplicity in Color Gauge Theory Models. *Phys. Rev. Lett.*, 37:402, 1976.

[22] S. S. Adler et al. Midrapidity Neutral Pion Production in Proton-Proton Collisions at $\sqrt{s}$ =200GeV/c. *Phys. Rev. Lett.*, 91:241803, 2003, hep-ex/0304038.

[23] S. S. Adler et al. Centrality Dependence of Direct Photon Production in $\sqrt{s_{NN}}$=200GeV Au+Au Collisions. *Phys. Rev. Lett.*, 94:232301, 2005.

[24] X. N. Wang and M. Gyulassy. Gluon Shadowing and Jet Quenching in A + A collisions at $\sqrt{s}$=200GeV. *Phys. Rev. Lett.*, 68:1480–1483, 1992.

[25] S. S. Adler et al. High-p_T Charged Hadron Suppression in Au+Au Collisions at $\sqrt{s_{NN}}$ =200GeV/c. *Phys. Rev.*, C69:034910, 2004, nucl-ex/0308006.

[26] S. S. Adler et al. Scaling Properties of Proton and anti-Proton Production in Collisions at $\sqrt{s_{NN}}$ =200GeV Au+Au Collisions. *Phys. Rev. Lett*, 91:172301, 2003, nucl-ex/0305036.

[27] S. S. Adler et al. Identified Charged Particle Spectra and Yields in Au+Au Collisions at $\sqrt{s_{NN}}$ =200GeV/c. *Phys. Rev.*, C69:034909, 2004, nucl-ex/0307022.

[28] F Matathias et al. π/K/p Production and Cronin Effect From p+p, d+Au and Au+Au Collisions at $\sqrt{s_{NN}}$=200GeV. *J. Phys.*, G30:S1113–1116, 2004, nucl-ex/0403029.

[29] S. S. Adler et al. Production of Φ mesons at mid-rapidity in $\sqrt{s_{NN}}$=200GeV Au+Au collisions at RHIC. *Phys. Rev*, C72:014903, 2005, nucl-ex/0410012.

[30] K.P. Das and R Hwa. Quark and anti-quark Recombination in the Fragmentation Region. *Phys. Lett.*, B68:459, 1978.

[31] S. S. Adler et al. Elliptic Flow of Identified Hadrons in Au+Au Collisions at $\sqrt{s_{NN}}$ =200GeV/c. *Phys. Rev. Lett.*, 91:182301, 2003, nucl-ex/0305013.

[32] R. J. Fries et al. Hadron production in heavy ion collisions: Fragmentation and recombination from a dense parton phase. *Phys. Rev.*, C68:044902, 2003, nucl-th/0306027.

[33] R Hwa and C. B. Yang. Recombination of shower partons in fragmentation process. *Phys. Rev.*, C70:024904, 2004.

[34] Greco V et al. Parton Coalescence at RHIC. *Phys. Rev.*, C68:034904, 2003.

[35] R. J. Fries. Recombination Models. *J. Phys.*, G30:S853–S860, 2004, nucl-th/0403036.

[36] Berndt Muller. Hadronic Signals of Deconfinement at RHIC. nucl-th/0404015.

[37] R Hwa and C. B. Yang. Final-State Interaction as the Origin of the Cronin Effect. *Phys. Rev. Lett.*, 93:082302, 2004, nucl-th/0403001.

[38] R Hwa and C. B. Yang. Proton Production in d+Au Collisions and the Cronin Effect. *Phys. Rev.*, C70:037901, 2004, nucl-th/0404066.

[39] S. S. Adler et al. Absence of Suppression in Particle Production at Large Transverse Momentum in $\sqrt{s_{NN}}$ =200GeV/c d+Au Collisions. *Phys. Rev. Lett.*, 91:072303, 2003, nucl-ex/0306021.

[40] S. S. Adler et al. Centrality Dependence of Identified Particle Spectra $\sqrt{s_{NN}}$=200GeV Au+Au Collisions, to be published.

[41] M. Allen et al. PHENIX Inner Detectors. *NIM*, A499:549–559, 2003.

[42] C. Adler et al. The RHIC Zero-Degree Calorimeters. *NIM*, A499:433–436, 2003.

[43] K. Adcox et al. PHENIX Central Arm Tracking Detectors. *NIM*, A499:489–507, 2003.

[44] M. Aizawa et al. PHENIX Central Arm Particle I.D. Detectors. *NIM*, A499:508–520, 2003.

[45] L. Aphecetche et al. PHENIX calorimeter. *NIM*, A499:521–536, 2003.

[46] C. Adler et al. Disappearance of back to back high p_T hadron correlations in central Au+Au collisions at $\sqrt{s_{NN}}$=200GeV. *Phys. Rev. Lett.*, 90:082302, 2003.

[47] S. S. Adler et al. Jet Structure of Baryon Excess in Au+Au Collisions at $\sqrt{s_{NN}} = 200\text{GeV}/c$. *Phys. Rev*, C71:051902(R), 2005, nucl-ex/0408007.

[48] S. S. Adler et al. Modifications to Di-Jet Hadron Pair Correlations in Au+Au Collisions at $\sqrt{s_{NN}}$=200GeV. nucl-ex/0507004.

[49] C. Adler et al. Distributions of Charged Hadrons Associated with High Transverse Momentum Particles in p+p and Au+Au at $\sqrt{s_{NN}}$=200GeV. nucl-ex/0501016.

[50] S. S. Adler et al. Jet Structure from Di-Hadron Correlations in d+Au Collisions at $\sqrt{s_{NN}}$=200GeV, to be published.

[51] K Adcox et al. Transvers Mass Dependence of Two-pion Correlations in Au+Au collisions at $\sqrt{s_{NN}}$=130GeV.

[52] J. Jia. Correlations Meeting June 1, 2005.

[53] J. Jia. Correlations Meeting March 16, 2005.

[54] S Leckey et al. Cronin Effect in Cold Nuclear Matter at RHIC, talk given at American Physical Society Division of Nuclear Physics Meeting, Tucso Az, October 2003.

[55] S. S. Adler et al. Measurement of Jet Properties in p+p Collisions at $\sqrt{s}$=200GeV, to be published.

[56] N Armesto et al. Low p_T Collective Flow Induces High p_T Jet Quenching. hep-ph/0411341.

[57] R. J. Fries et al. Correlated Emission of Hadrons from Recombination of Correlated Partons. *Phys. Rev. Lett*, 94:122301, 2005, nucl-th/0407102.

[58] R Hwa and C. B. Yang. Recombination of Shower Partons at High p_T in Heavy-Ion Collisions. *Phys. Rev.*, C70:024905, 2004.

[59] G. Corcella et al. Herwig 6.5. *JHEP*, 0101:010, 2001.

[60] S. S. Adler et al. Suppressed π^0 Production at Large Transverse Momentum in Central Au+Au Collisions at $\sqrt{s_{NN}}$=200GeV. *Phys. Rev. Lett*, 91:072301, 2003, nucl-ex/0304022.

[61] J.W. Cronin et al. Production of Hadrons with Large Transverse Momentum at 200 GeV, 300 GeV, and 400 GeV. *Phys. Rev.*, D11:3105, 1975.

[62] C. Adler et al. Pion, Kaon, proton and anti-proton transverse momentum distributions from p+p and d+Au collisions at $\sqrt{s_{NN}}$=200GeV. *Phys. Lett.*, B616:8–16, 2005.

[63] Nathan Grau. Quantifying the Near Angle Structure of Leading Identified Conditional Yield Distributions PHENIX analysis note 309.

[64] M Konno. Systematic Study of Identified Particle Production in PHENIX, Quark Matter 2005 talk.

Appendix A

Fits to Single Particle Yields for ξ Values

A.0.1 Au+Au Fits

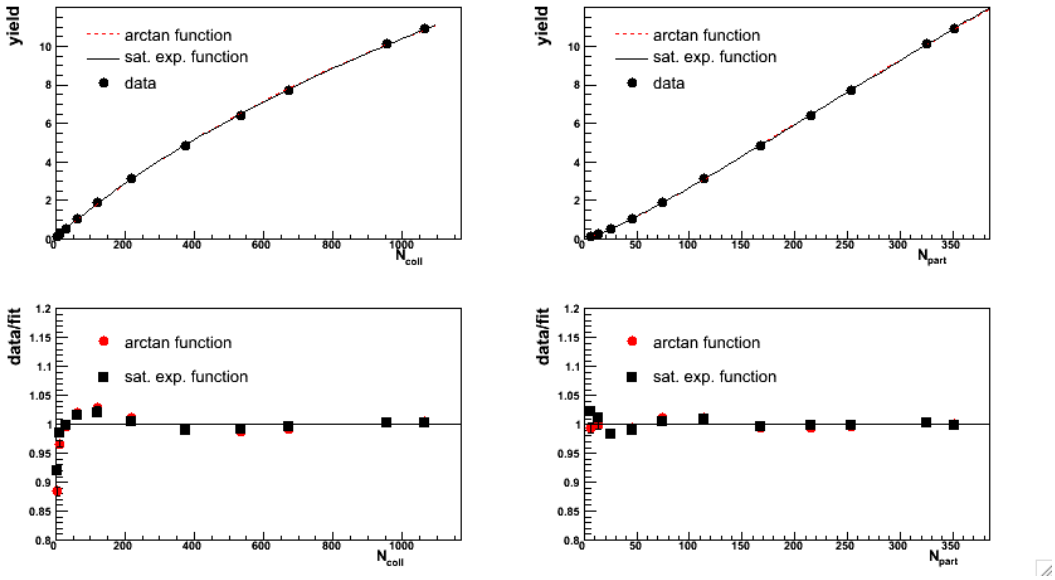

Figure A.1: Top panels show fits to the charge particle integrated yields from [25] as a function of N_{coll} (left) and N_{part} (right) for p_T =1.05GeV/c . Red dashed lines are fits to the arctan function and solid black lines are fits to the saturating exponential function. Bottom panels show the ratio of data to the fit as a function of N_{coll} (left) and N_{part} (right). Red circles are for the arctan fits and black squares are for the saturating exponential fits. Fit parameters are shown in Table A.1.

		A	B	α
N_{coll}	arctan	17.0098	0.00161608	0.879074
	sat. exp.	27.646	-0.000922618	0.903036
N_{part}	arctan	20.8404	0.000527143	1.19376
	sat. exp.	39.9932	-0.000257328	1.2152

Table A.1: Fit values for charged particle yields at p_T =1.05GeV/c from [25]. The fit equations are Equations. 4.6 and 4.7.

		A	B	α
N_{coll}	arctan	11.6601	0.00155262	0.893044
	sat. exp.	18.5279	-0.000901165	0.918737
N_{part}	arctan	13.9485	0.000509222	1.21353
	sat. exp.	25.5536	-0.000258043	1.2378

Table A.2: Fit values for charged particle yields at p_T =1.15GeV/c from [25]. The fit equations are Equations. 4.6 and 4.7.

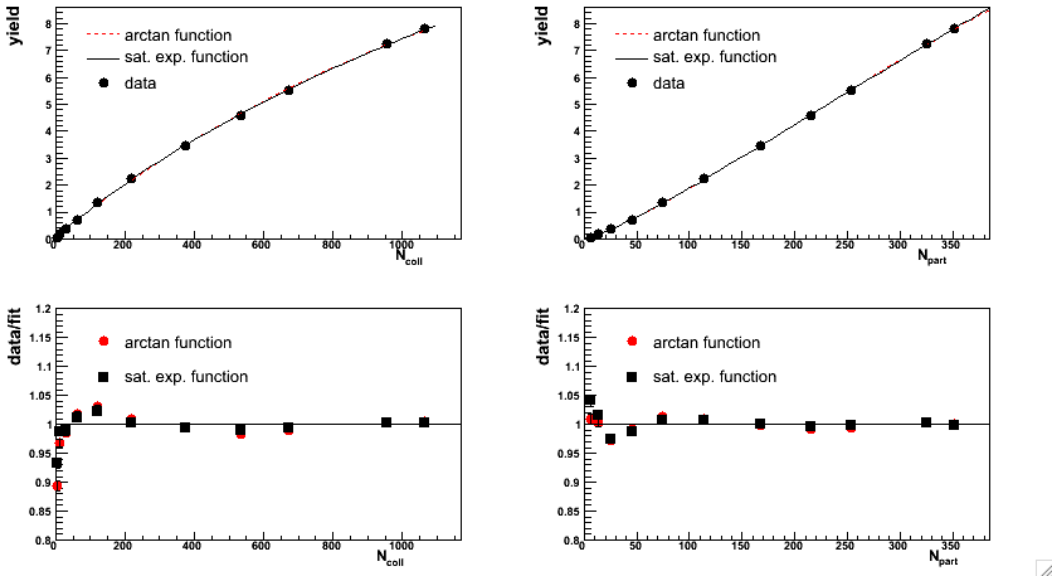

Figure A.2: Top panels show fits to the charge particle integrated yields from [25] as a function of N_{coll} (left) and N_{part} (right) for p_T =1.15GeV/c . Red dashed lines are fits to the arctan function and solid black lines are fits to the saturating exponential function. Bottom panels show the ratio of data to the fit as a function of N_{coll} (left) and N_{part} (right). Red circles are for the arctan fits and black squares are for the saturating exponential fits. Fit parameters are shown in Table A.2.

		A	B	α
N_{coll}	arctan	8.32717	0.00147625	0.903019
	sat. exp.	13.1093	-0.000861669	0.929607
N_{part}	arctan	9.89262	0.000481785	1.22743
	sat. exp.	17.7822	-0.000247469	1.25319

Table A.3: Fit values for charged particle yields at p_T =1.25GeV/c from [25]. The fit equations are Equations. 4.6 and 4.7.

		A	B	α
N_{coll}	arctan	5.99039	0.00141749	0.910745
	sat. exp.	9.4408	-0.000826981	0.937192
N_{part}	arctan	7.0615	0.000461376	1.23849
	sat. exp.	12.6751	-0.000237493	1.26414

Table A.4: Fit values for charged particle yields at p_T =1.35GeV/c from [25]. The fit equations are Equations. 4.6 and 4.7.

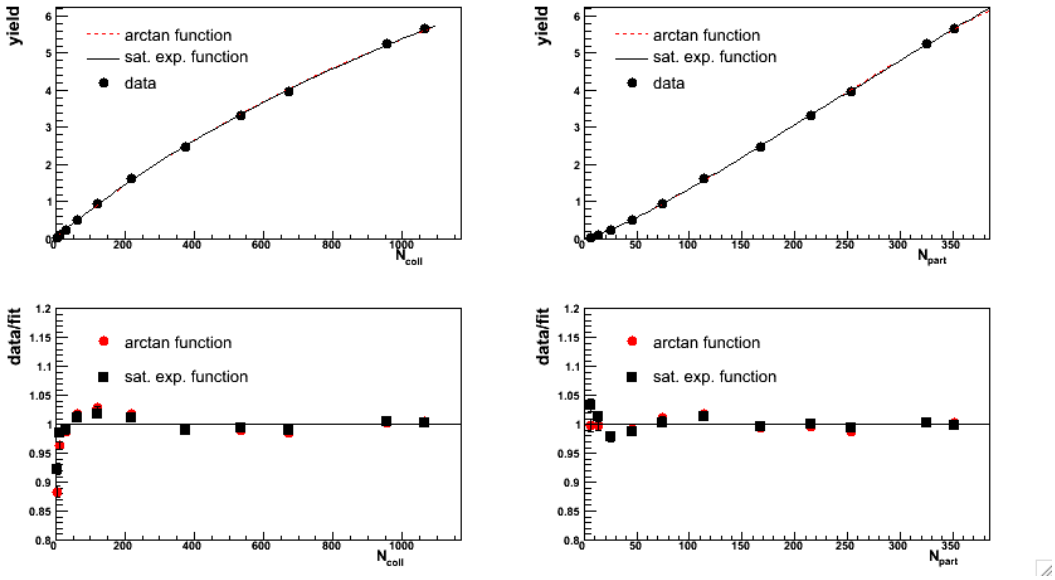

Figure A.3: Top panels show fits to the charge particle integrated yields from [25] as a function of N_{coll} (left) and N_{part} (right) for p_T =1.25GeV/c . Red dashed lines are fits to the arctan function and solid black lines are fits to the saturating exponential function. Bottom panels show the ratio of data to the fit as a function of N_{coll} (left) and N_{part} (right). Red circles are for the arctan fits and black squares are for the saturating exponential fits. Fit parameters are shown in Table A.3.

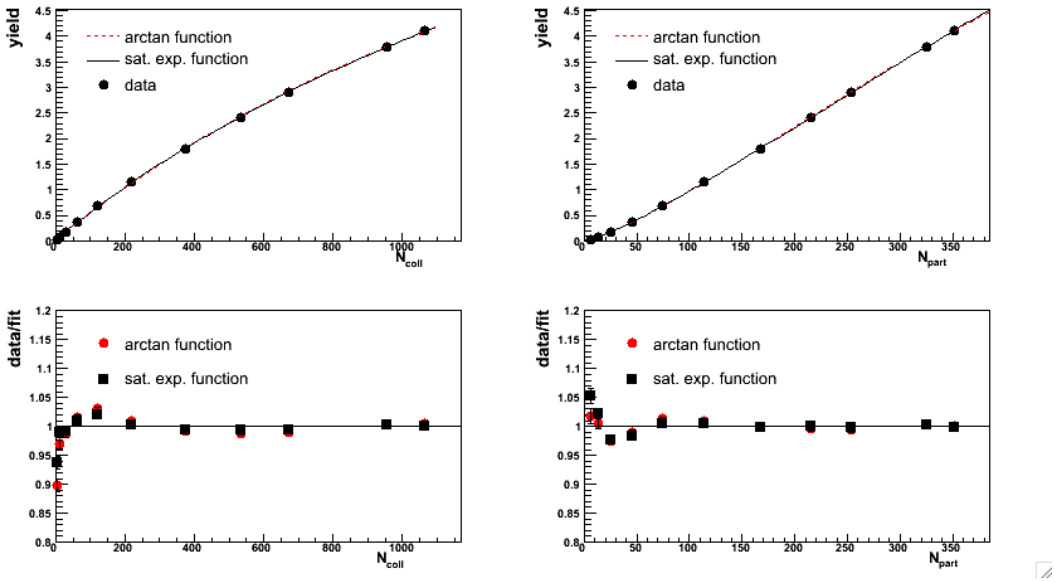

Figure A.4: Top panels show fits to the charge particle integrated yields from [25] as a function of N_{coll} (left) and N_{part} (right) for p_T =1.35GeV/c . Red dashed lines are fits to the arctan function and solid black lines are fits to the saturating exponential function. Bottom panels show the ratio of data to the fit as a function of N_{coll} (left) and N_{part} (right). Red circles are for the arctan fits and black squares are for the saturating exponential fits. Fit parameters are shown in Table A.4.

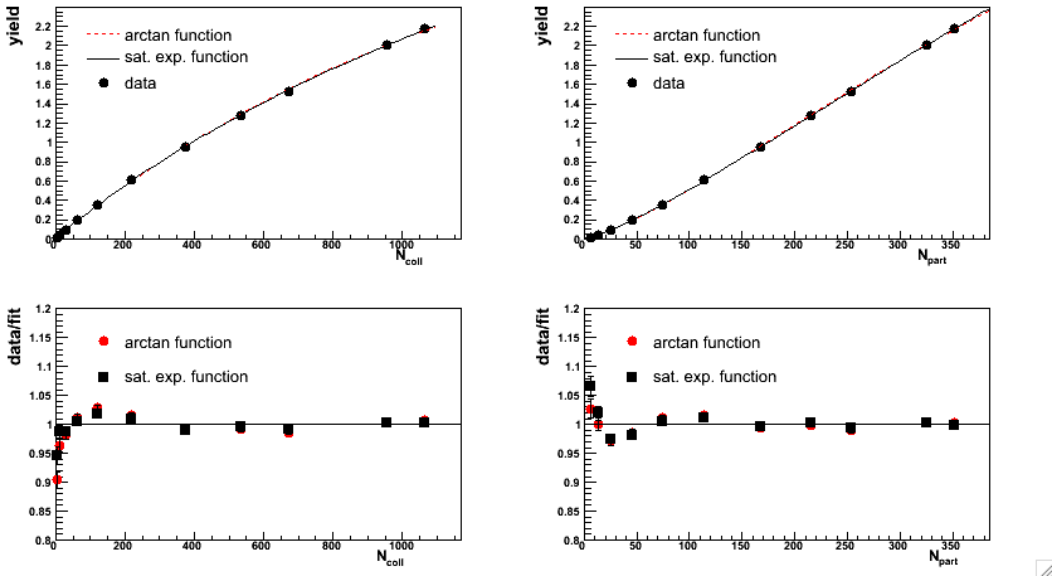

Figure A.5: Top panels show fits to the charge particle integrated yields from [25] as a function of N_{coll} (left) and N_{part} (right) for p_T =1.55GeV/c . Red dashed lines are fits to the arctan function and solid black lines are fits to the saturating exponential function. Bottom panels show the ratio of data to the fit as a function of N_{coll} (left) and N_{part} (right). Red circles are for the arctan fits and black squares are for the saturating exponential fits. Fit parameters are shown in Table A.5.

		A	B	α
N_{coll}	arctan	3.07339	0.00138509	0.920084
	sat. exp.	4.76149	-0.000817552	0.948025
N_{part}	arctan	3.5759	0.000451364	1.25159
	sat. exp.	6.21121	-0.000238056	1.27974

Table A.5: Fit values for charged particle yields at p_T =1.55GeV/c from [25]. The fit equations are Equations. 4.6 and 4.7.

		A	B	α
N_{coll}	arctan	0.787407	0.00142642	0.939932
	sat. exp.	1.15314	-0.000876653	0.972976
N_{part}	arctan	0.878761	0.000473407	1.27911
	sat. exp.	1.38322	-0.000268297	1.31579

Table A.6: Fit values for charged particle yields at p_T =1.95GeV/c from [25]. The fit equations are Equations. 4.6 and 4.7.

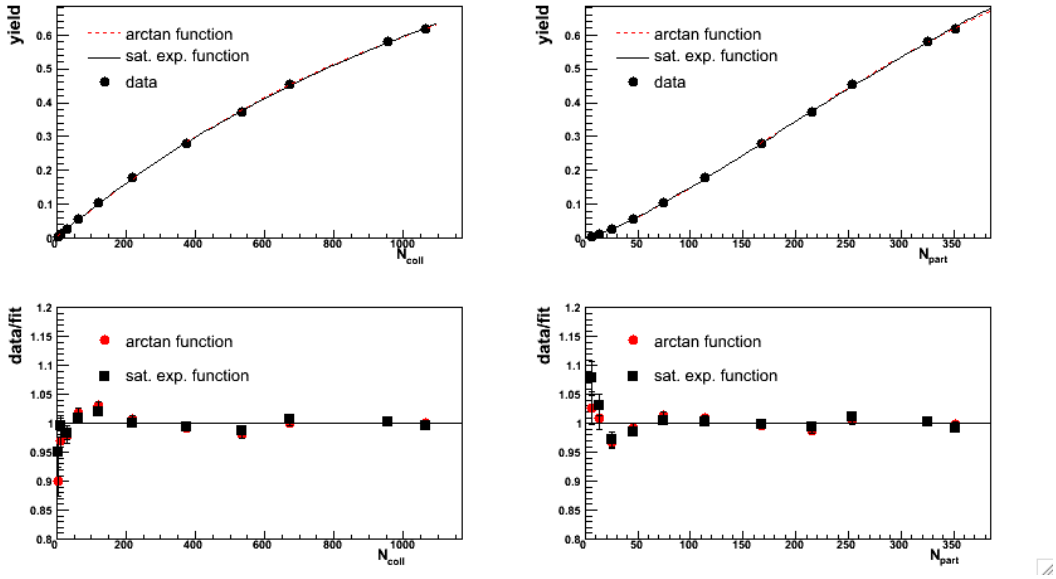

Figure A.6: Top panels show fits to the charge particle integrated yields from [25] as a function of N_{coll} (left) and N_{part} (right) for p_T =1.95GeV/c . Red dashed lines are fits to the arctan function and solid black lines are fits to the saturating exponential function. Bottom panels show the ratio of data to the fit as a function of N_{coll} (left) and N_{part} (right). Red circles are for the arctan fits and black squares are for the saturating exponential fits. Fit parameters are shown in Table A.6.

		A	B	α
N_{coll}	arctan	0.619124	0.00147256	0.930078
	sat. exp.	0.914335	-0.000898531	0.962651
N_{part}	arctan	0.686705	0.000497328	1.26633
	sat. exp.	1.08525	-0.000280269	1.30332

Table A.7: Fit values for charged meson ($\pi^{\pm}$ and $K^{\pm}$ yields at p_T =1.95GeV/c from [27]. The fit equations are Equations. 4.6 and 4.7.

		A	B	α
N_{coll}	arctan	0.234321	0.000634797	1.04105
	sat. exp.	0.361394	-0.000369036	1.07213
N_{part}	arctan	0.2582	0.000185445	1.42524
	sat. exp.	0.427169	-9.93847e-05	1.46091

Table A.8: Fit values for charged baryon (p and $\bar{p}$ yields at p_T =1.95GeV/c from [27]. The fit equations are Equations. 4.6 and 4.7.

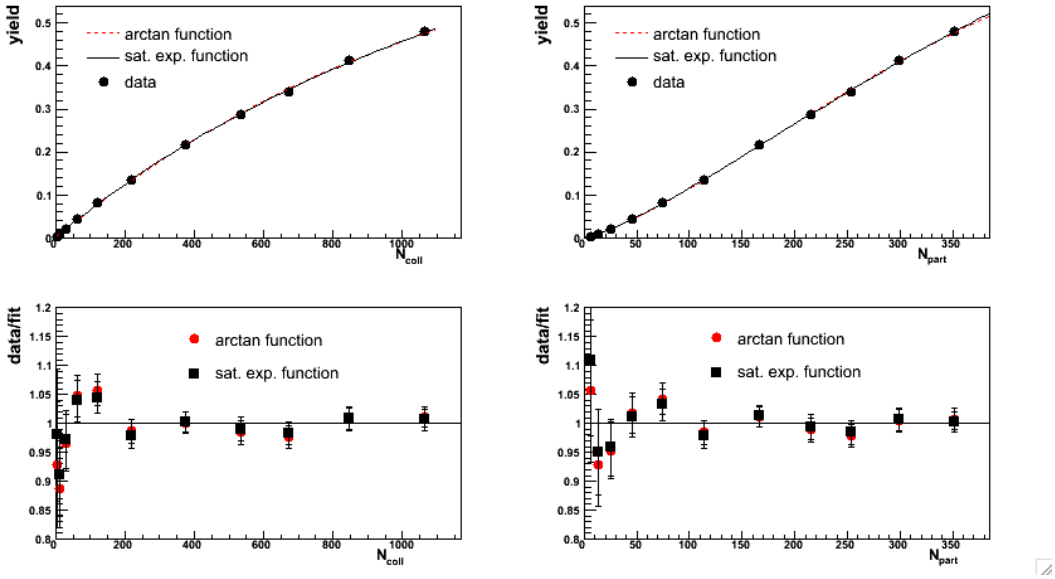

Figure A.7: Top panels show fits to the meson ($\pi^{\pm}$ and $K^{\pm}$) integrated yields from [27] as a function of N_{coll} (left) and N_{part} (right) for p_T =1.95GeV/c . Red dashed lines are fits to the arctan function and solid black lines are fits to the saturating exponential function. Bottom panels show the ratio of data to the fit as a function of N_{coll} (left) and N_{part} (right). Red circles are for the arctan fits and black squares are for the saturating exponential fits. Fit parameters are shown in Table A.7.

		A	B	α
N_{coll}	arctan	0.0143645	0.00380828	1.02562
	sat. exp.	0.0197924	-0.00272521	1.04988
N_{part}	arctan	0.0147037	0.00131608	1.38262
	sat. exp.	0.0200944	-0.000901298	1.42302

Table A.9: Fit values for π^0 yields at p_T =2.75GeV/c from [60]. The fit equations are Equations. 4.6 and 4.7.

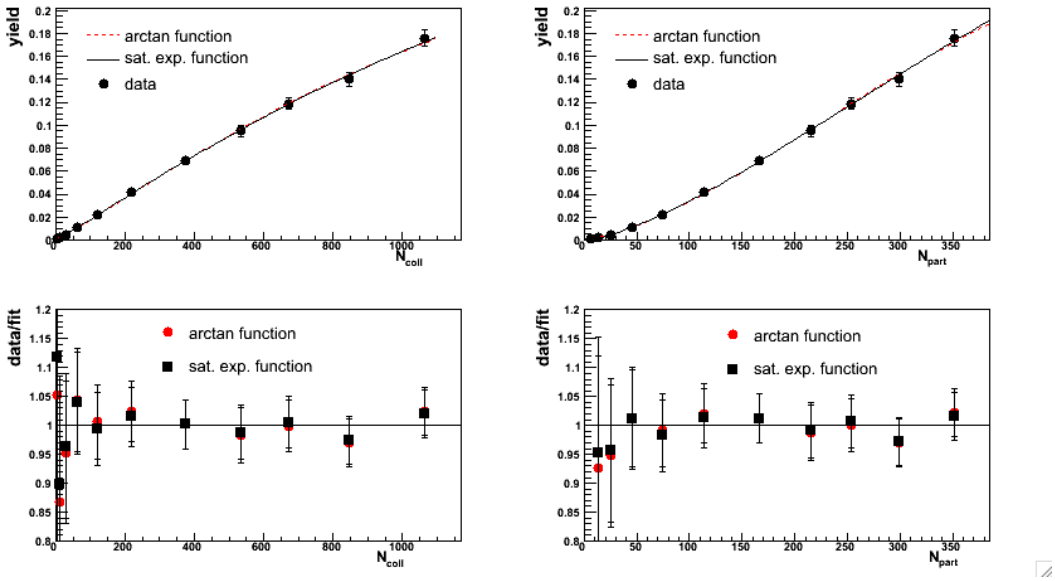

Figure A.8: Top panels show fits to the baryon (p and $\bar{p}$) integrated yields from [27] as a function of N_{coll} (left) and N_{part} (right) for p_T =1.95GeV/c . Red dashed lines are fits to the arctan function and solid black lines are fits to the saturating exponential function. Bottom panels show the ratio of data to the fit as a function of N_{coll} (left) and N_{part} (right). Red circles are for the arctan fits and black squares are for the saturating exponential fits. Fit parameters are shown in Table A.8.

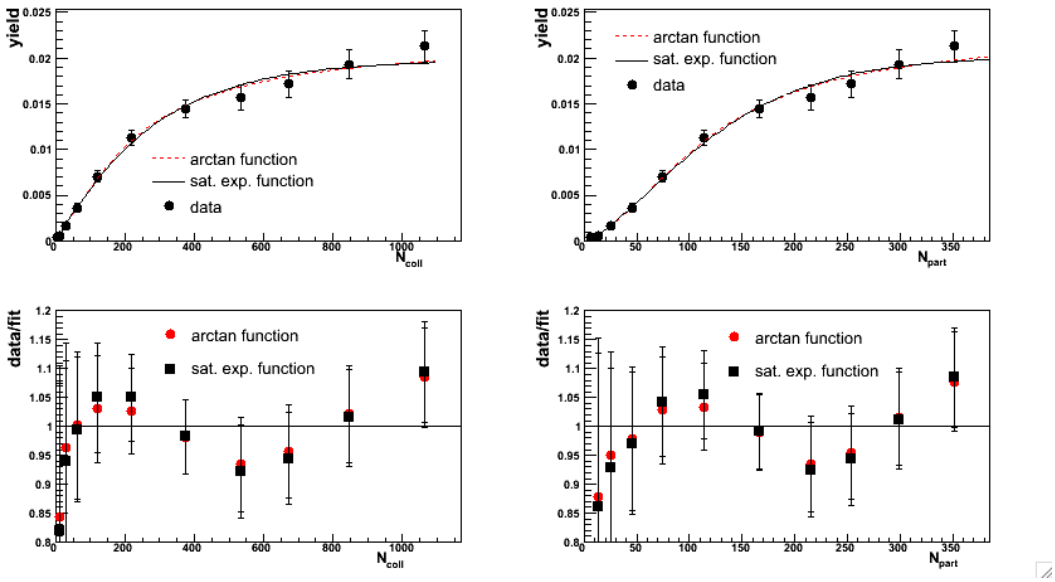

Figure A.9: Top panels show fits to the π^0 integrated yields from [60] as a function of N_{coll} (left) and N_{part} (right) for p_T =2.75GeV/c . Red dashed lines are fits to the arctan function and solid black lines are fits to the saturating exponential function. Bottom panels show the ratio of data to the fit as a function of N_{coll} (left) and N_{part} (right). Red circles are for the arctan fits and black squares are for the saturating exponential fits. Fit parameters are shown in Table A.9.

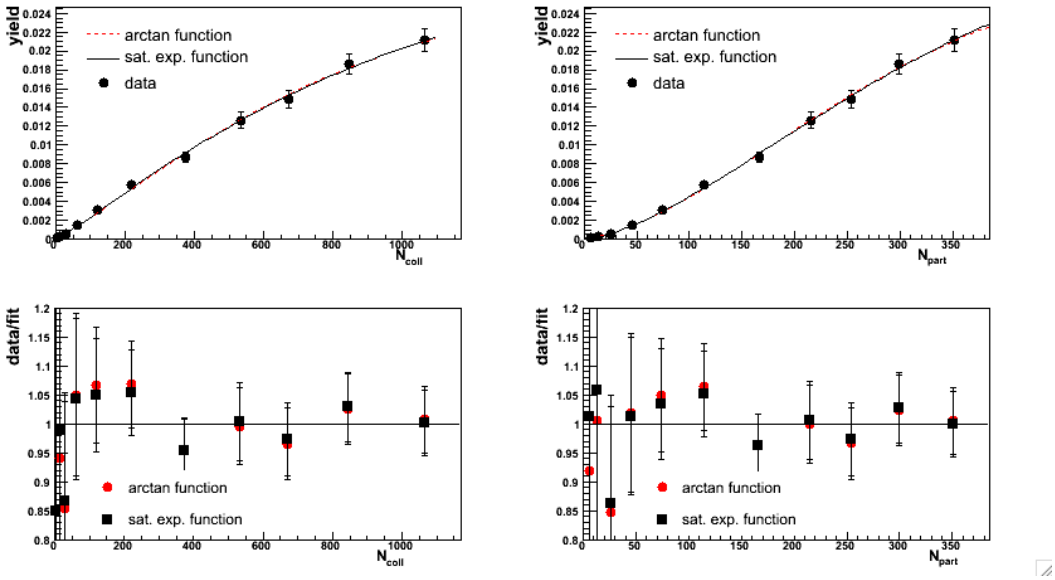

Figure A.10: Top panels show fits to the baryon (p and $\bar{p}$) integrated yields from [27] as a function of N_{coll} (left) and N_{part} (right) for p_T =2.70GeV/c . Red dashed lines are fits to the arctan function and solid black lines are fits to the saturating exponential function. Bottom panels show the ratio of data to the fit as a function of N_{coll} (left) and N_{part} (right). Red circles are for the arctan fits and black squares are for the saturating exponential fits. Fit parameters are shown in Table A.10.

		A	B	α
N_{coll}	arctan	0.0228036	0.000703435	1.08075
	sat. exp.	0.0311713	-0.000437324	1.12726
N_{part}	arctan	0.023975	0.000206535	1.47947
	sat. exp.	0.0333541	-0.00012066	1.54059

Table A.10: Fit values for charged baryon (p and $\bar{p}$ yields at p_T =2.70GeV/c from [27]. The fit equations are Equations. 4.6 and 4.7.

A.0.2 d+Au Fits

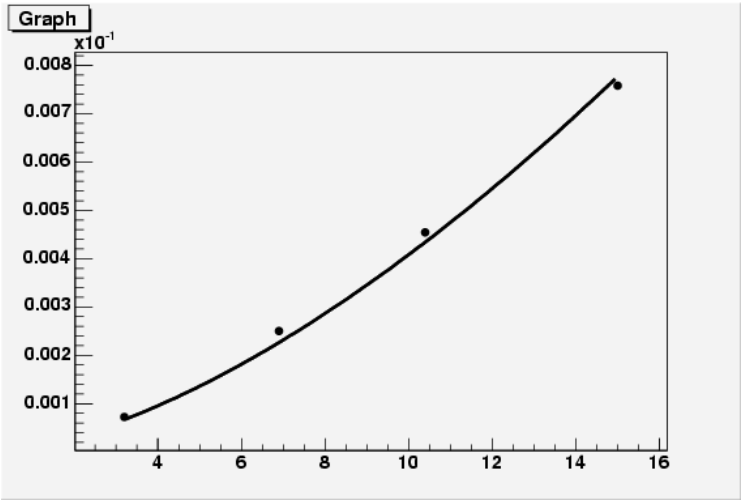

Figure A.11: Proton/anti-proton yield at 2.95GeV in d+Au as a function of N_{coll} from [40] with fit to an arctan

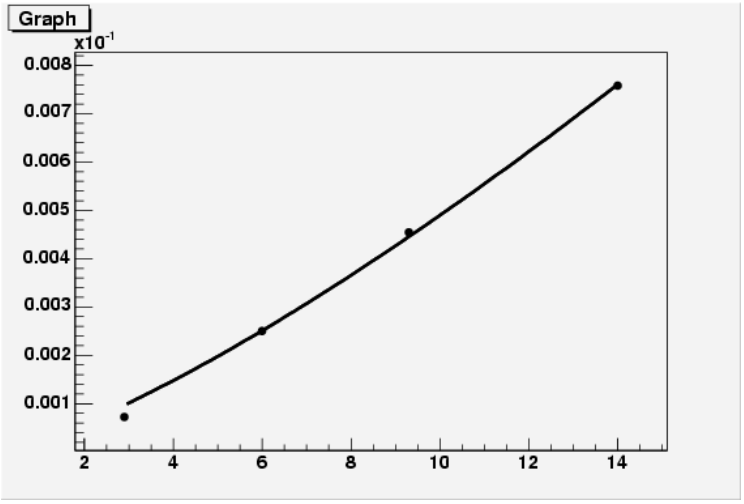

Figure A.12: Proton/anti-proton yield at 2.95GeV in d+Au as a function of N_{part} from [40] with fit to an arctan

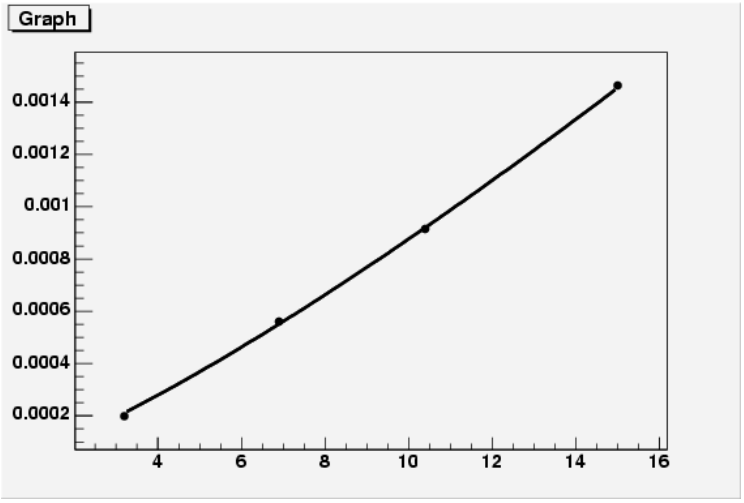

Figure A.13: Charged hadron yield at 2.9GeV in d+Au as a function of N_{coll} from [54] with fit to an arctan

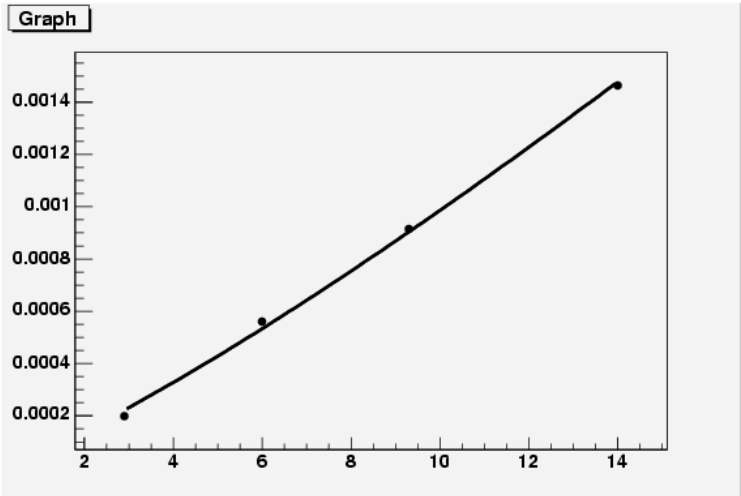

Figure A.14: Charged hadron yield at 2.9GeV in d+Au as a function of N_{part} from [54] with fit to an arctan

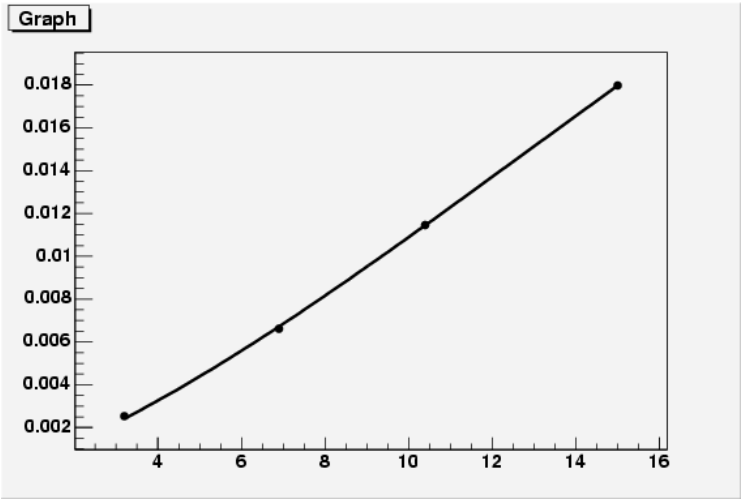

Figure A.15: Charged hadron yield at 1.95GeV in d+Au as a function of N_{coll} from [54] with fit to an arctan

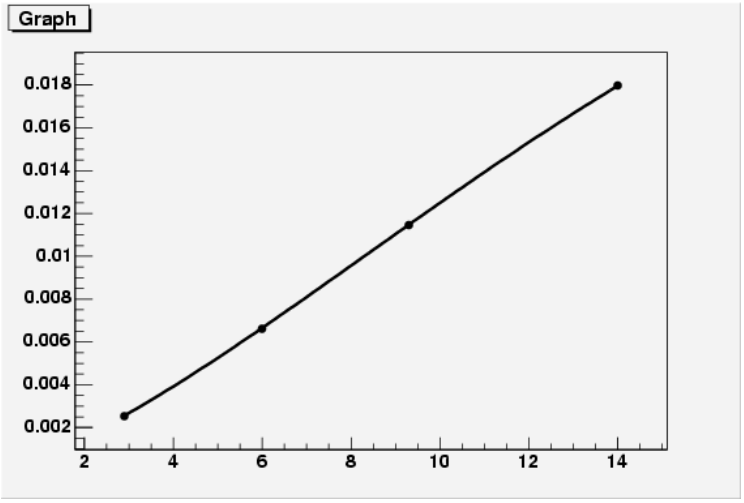

Figure A.16: Charged hadron yield at 1.95GeV in d+Au as a function of N_{part} from [54] with fit to an arctan

Type	N	Fit Function	A	B	α
protons at $< p_T >= 2.95GeV$	N_{coll}	arctan	0.037	0.000284	1.59
protons at $< p_T >= 2.95GeV$	N_{part}	arctan	0.0245	0.00098	1.31
ch. part. at $< p_T >= 2.9GeV$	N_{coll}	arctan	0.032	0.00148	1.266
ch. part. at $< p_T >= 2.9GeV$	N_{part}	arctan	0.039	0.00167	1.18
ch. part. at $< p_T >= 1.95GeV$	N_{coll}	arctan	0.0405	0.0125	1.34
ch. part. at $< p_T >= 1.95GeV$	N_{part}	arctan	0.027	0.0225	1.34

Table A.11: Fit parameters to the charged particle yields used to determine ξ in d+Au. See text for parameter definitions and the resulting ξ values.

Appendix B

ξ Values

B.0.3 Au+Au ξ Values in Run4

The following tables show the ξ values used in the Run 4 analysis for the different trigger and partner combinations.

Centrality	N_{coll} satexp.	N_{part} satexp.	N_{coll} arctan	N_{part} arctan
0	1.00081	1.0005	1.00083	1.00094
5	1.00283	1.00121	1.00134	1.00133
10	1.00344	1.00363	1.00202	1.0022
15	1.00559	1.00619	1.00323	1.00358
20	1.00852	1.01	1.00502	1.00552
25	1.01367	1.01382	1.00804	1.00864
30	1.01945	1.02088	1.01077	1.01126
35	1.02996	1.02788	1.01512	1.01467
40	1.04078	1.04037	1.0235	1.02263
45	1.05744	1.05644	1.03358	1.03264
50	1.07931	1.07509	1.05344	1.05233
55	1.11017	1.10761	1.0805	1.08468
60	1.15684	1.15216	1.12739	1.12551
65	1.23416	1.24113	1.21442	1.21394
70	1.2939	1.30751	1.31426	1.3223
75	1.38883	1.39925	1.41244	1.41966
80	1.45485	1.4945	1.48932	1.51535
85	1.59569	1.65636	1.63501	1.67991

Table B.1: ξ values used for meson triggers from 2.5$<$ p_T $<$4.0 GeV/c and unidentified partners from 1.7$<$ p_T $<$2.5GeV/c . Centrality values listed are the low edge of the 5% centrality bins used.

Centrality	N_{coll} satexp.	N_{part} satexp.	N_{coll} arctan	N_{part} arctan
0	1.00359	1.00285	1.00177	1.00205
5	1.0061	1.00686	1.00401	1.00449
10	1.01065	1.0106	1.00604	1.00638
15	1.01443	1.01331	1.00814	1.0077
20	1.02019	1.02038	1.01155	1.0092
25	1.0262	1.02518	1.01365	1.01319
30	1.03421	1.03237	1.01962	1.01859
35	1.04092	1.04086	1.02294	1.02252
40	1.05202	1.04999	1.03056	1.02763
45	1.06838	1.07246	1.04056	1.03783
50	1.0903	1.0908	1.06137	1.06426
55	1.11826	1.1248	1.08755	1.10042
60	1.16733	1.17897	1.13088	1.14559
65	1.25128	1.27127	1.22891	1.22944
70	1.31984	1.35639	1.32807	1.36997
75	1.41166	1.42923	1.47026	1.45922
80	1.47123	1.45981	1.53015	1.5849
85	1.66908	1.637	1.68661	1.74399

Table B.2: ξ values used for baryon triggers from 2.5$<$ p_T $<$4.0 GeV/c and unidentified partners from 1.7$<$ p_T $<$2.5GeV/c . Centrality bins listed are the low edge of the 5% centrality bins used.

Centrality	N_{coll} satexp.	N_{part} satexp.	N_{coll} arctan	N_{part} arctan
0	1.00122	1.0003	1.00046	0.999304
5	1.00157	1.00107	1.00162	1.00148
10	1.00292	1.00316	1.00262	1.00159
15	1.00543	1.00498	1.00238	1.00292
20	1.00855	1.00857	1.00493	1.00443
25	1.01291	1.014	1.00654	1.00775
30	1.01831	1.01889	1.00993	1.01123
35	1.02761	1.02821	1.01443	1.01422
40	1.04089	1.03694	1.02301	1.02182
45	1.05288	1.0537	1.03228	1.03103
50	1.07584	1.07329	1.05077	1.05263
55	1.10337	1.10309	1.07849	1.07898
60	1.15078	1.15	1.12771	1.12738
65	1.21853	1.23025	1.20265	1.2169
70	1.29442	1.30462	1.28963	1.31661
75	1.37374	1.39652	1.37624	1.44431
80	1.42393	1.47866	1.48281	1.49594
85	1.58466	1.61018	1.60338	1.62899

Table B.3: ξ values used for meson triggers from 2.5$<$ p_T $<$4.0 GeV/c and meson partners from 1.7$<$ p_T $<$2.5GeV/c . Centrality bins listed are the low edge of the 5% centrality bins used.

Centrality	N_{coll} satexp.	N_{part} satexp.	N_{coll} arctan	N_{part} arctan
0	1.00087	1.00037	1.00103	0.999791
5	1.00207	1.00124	1.00138	1.0012
10	1.00325	1.00291	1.00324	1.00202
15	1.00618	1.00518	1.0031	1.00335
20	1.00988	1.00998	1.00511	1.00594
25	1.01436	1.01579	1.00743	1.00865
30	1.02022	1.0221	1.01162	1.01224
35	1.03176	1.03193	1.01641	1.01621
40	1.04336	1.04298	1.0259	1.02479
45	1.05921	1.05626	1.03712	1.03228
50	1.08244	1.08577	1.05656	1.0582
55	1.11612	1.113	1.08978	1.10277
60	1.16523	1.16359	1.14119	1.14556
65	1.24972	1.2657	1.22996	1.24257
70	1.33457	1.34496	1.34485	1.35881
75	1.4181	1.42986	1.44481	1.48069
80	1.49926	1.50908	1.52958	1.56928
85	1.64953	1.67852	1.69874	1.76383

Table B.4: ξ values used for meson triggers from 2.5$<p_T<$4.0 GeV/c and baryon partners from 1.7$<p_T<$2.5GeV/c . Centrality bins listed are the low edge of the 5% centrality bins used.

Centrality	N_{coll} satexp.	N_{part} satexp.	N_{coll} arctan	N_{part} arctan
0	1.00388	1.00427	1.00202	1.00302
5	1.00591	1.00746	1.00412	1.00446
10	1.01006	1.01052	1.00616	1.0061
15	1.01412	1.01454	1.00769	1.00728
20	1.01895	1.01848	1.01098	1.01088
25	1.02616	1.02418	1.01399	1.01349
30	1.03345	1.03282	1.01911	1.01694
35	1.04037	1.04093	1.02575	1.019
40	1.05409	1.055	1.02976	1.03213
45	1.06661	1.06429	1.04119	1.03941
50	1.08508	1.09558	1.06323	1.06331
55	1.11592	1.12381	1.09233	1.08671
60	1.16845	1.17295	1.13932	1.14732
65	1.24298	1.2588	1.22172	1.2445
70	1.32946	1.34715	1.32769	1.37184
75	1.42348	1.44896	1.42322	1.48188
80	1.48735	1.51944	1.50623	1.54778
85	1.63681	1.65941	1.70831	1.74254

Table B.5: ξ values used for baryon triggers from 2.5$<$ p_T $<$4.0 GeV/c and meson partners from 1.7$<$ p_T $<$2.5GeV/c . Centrality bins listed are the low edge of the 5% centrality bins used.

Centrality	N_{coll} satexp.	N_{part} satexp.	N_{coll} arctan	N_{part} arctan
0	1.00385	1.00447	1.00202	1.00304
5	1.00709	1.00836	1.00484	1.0037
10	1.01058	1.01221	1.0063	1.0067
15	1.01605	1.01575	1.00961	1.00913
20	1.02128	1.02344	1.0128	1.01167
25	1.0296	1.02806	1.0158	1.01514
30	1.03943	1.03399	1.02037	1.01701
35	1.04416	1.04591	1.02173	1.02434
40	1.05892	1.05632	1.03377	1.03327
45	1.07384	1.08141	1.04627	1.04306
50	1.09437	1.10727	1.06978	1.06675
55	1.13225	1.14297	1.10489	1.10767
60	1.17687	1.18506	1.15116	1.16907
65	1.27709	1.29976	1.26423	1.27839
70	1.36365	1.37966	1.37577	1.41137
75	1.40029	1.48235	1.491	1.54412
80	1.56742	1.58654	1.60198	1.61124
85	1.7	1.80037	1.75047	1.68611

Table B.6: ξ values used for baryon triggers from 2.5$<p_T<$4.0 GeV/c and baryon partners from 1.7$<p_T<$2.5GeV/c . These ξ values are also used when the trigger is identified as either p or $\bar{p}$ and the partner is also identified as a p or $\bar{p}$. Centrality bins listed are the low edge of the 5% centrality bins used.

B.0.4 Au+Au ξ Values in Run 2

The following tables are the ξ values calculated for the Run 2 analysis for the different trigger and p_T combinations.

Centrality	ξ			
	N_{coll} sat.exp.	N_{part} sat. exp.	N_{coll} arctan	N_{part} arctan
Leading Mesons				
0-5	1.00264	1.00177	1.00217	1.00191
5-10	1.00464	1.00296	1.00395	1.00325
10-15	1.00699	1.00434	1.00667	1.0043
15-20	1.00967	1.00581	1.00883	1.0057
20-25	1.01382	1.00823	1.01412	1.00765
25-30	1.01801	1.00968	1.01853	1.01106
30-35	1.02345	1.01287	1.02387	1.01303
35-40	1.03093	1.01612	1.03135	1.01611
40-45	1.03875	1.0228	1.0402	1.02236
45-50	1.05237	1.02958	1.05621	1.03541
50-55	1.06878	1.0459	1.07021	1.04723
55-60	1.09877	1.07281	1.09653	1.07126
60-65	1.13965	1.11512	1.13105	1.10877
65-70	1.21383	1.19491	1.19767	1.18441
70-75	1.2904	1.27995	1.26118	1.2588
75-80	1.36413	1.36171	1.32677	1.33657
80-85	1.40724	1.42396	1.43908	1.38492
85-90	1.54686	1.56954	1.51006	1.62737
	N_{coll} sat.exp.	N_{part} sat. exp.	N_{coll} arctan	N_{part} arctan
Leading Baryons				
0-5	1.00421	1.0043	1.00266	1.00424
5-10	1.00409	1.00722	1.00616	1.00406
10-15	1.01041	1.00884	1.01052	1.00766
15-20	1.01109	1.01039	1.01339	1.00838
20-25	1.01817	1.00772	1.01616	1.0101
25-30	1.02216	1.01049	1.01956	1.00924
30-35	1.03041	1.01878	1.02845	1.01638
35-40	1.03351	1.01935	1.03733	1.01906
40-45	1.04293	1.03923	1.04349	1.0222
45-50	1.06037	1.03008	1.05692	1.03458
50-55	1.08168	1.05351	1.07361	1.05154
55-60	1.11422	1.10093	1.11122	1.06764
60-65	1.13492	1.13766	1.15083	1.12584
65-70	1.28475	1.21939	1.21826	1.17594
70-75	1.30362	1.31309	1.33225	1.29803
75-80	1.30632	1.38047	1.39424	1.41303
80-85	1.36329	1.57176	1.38906	1.45594
85-90	1.70709	1.65096	1.48836	1.68689

Table B.7: Values of ξ used for each centrality bin mixed in Au+Au for triggers with $2.5< p_T <4.0$GeV/c and partners with $1.7< p_T <2.5$GeV/c .

Centrality	ξ			
	N_coll sat. exp	N_{part} sat. exp.	N_{coll} arctan	N_{part} arctan
Leading Mesons				
0-5	1.00228	1.00196	1.00234	1.00181
5-10	1.00454	1.0033	1.00437	1.00315
10-15	1.00697	1.00464	1.00691	1.00467
15-20	1.01034	1.0057	1.01049	1.00597
20-25	1.01387	1.00801	1.01343	1.00804
25-30	1.01743	1.00971	1.0183	1.01031
30-35	1.0225	1.01254	1.02396	1.01314
35-40	1.0306	1.01624	1.03043	1.01641
40-45	1.03968	1.02175	1.04038	1.02228
45-50	1.05091	1.0291	1.04995	1.0302
50-55	1.06863	1.04615	1.06673	1.04542
55-60	1.09532	1.07049	1.09025	1.0689
60-65	1.13773	1.10764	1.12286	1.1078
65-70	1.2009	1.18607	1.19443	1.17716
70-75	1.276	1.27495	1.24864	1.25831
75-80	1.31276	1.36233	1.35909	1.33421
80-85	1.40133	1.42125	1.3619	1.39207
85-90	1.55147	1.54882	1.49827	1.51934
Leading Baryons				
0-5	1.00425	1.00306	1.00421	1.00276
5-10	1.00725	1.00456	1.00679	1.00486
10-15	1.01002	1.00615	1.01018	1.00696
15-20	1.01316	1.00815	1.01398	1.00735
20-25	1.01763	1.01044	1.01856	1.01047
25-30	1.0222	1.01255	1.02299	1.01282
30-35	1.02917	1.01616	1.02899	1.01577
35-40	1.03648	1.02167	1.03655	1.01863
40-45	1.04503	1.0285	1.04608	1.02525
45-50	1.05781	1.03288	1.05923	1.03531
50-55	1.07806	1.0601	1.07714	1.04964
55-60	1.10786	1.08592	1.10321	1.08047
60-65	1.15349	1.12889	1.13833	1.11866
65-70	1.22651	1.22487	1.21395	1.19309
70-75	1.31032	1.29469	1.28573	1.28605
75-80	1.39744	1.42439	1.35421	1.38269
80-85	1.4521	1.41006	1.41489	1.42771
85-90	1.61028	1.69501	1.53395	1.56453

Table B.8: ξ values for each centrality bin in Au+Au for partner $1.45 < p_T 1.7 GeV/c$

Centrality	ξ			
	N_coll sat. exp	N_{part} sat. exp.	N_{coll} arctan	N_{part} arctan
Leading Mesons				
0-5	1.00277	1.00196	1.00253	1.00183
5-10	1.00429	1.00305	1.00459	1.00317
10-15	1.00763	1.00514	1.0067	1.0046
15-20	1.00958	1.00589	1.00826	1.00581
20-25	1.01345	1.00814	1.01378	1.00799
25-30	1.0179	1.01034	1.01847	1.0102
30-35	1.02283	1.01275	1.02472	1.0129
35-40	1.03041	1.01565	1.03163	1.01613
40-45	1.03792	1.02177	1.03992	1.02203
45-50	1.05263	1.02957	1.0487	1.02969
50-55	1.06855	1.0458	1.0658	1.04462
55-60	1.09375	1.07021	1.0922	1.06815
60-65	1.1329	1.11057	1.13278	1.10609
65-70	1.20035	1.18337	1.18869	1.17432
70-75	1.27342	1.26292	1.25112	1.25356
75-80	1.34241	1.35899	1.31181	1.33034
80-85	1.39642	1.41767	1.35039	1.38575
85-90	1.52832	1.54436	1.49051	1.5098
Leading Baryons				
0-5	1.00469	1.00283	1.00409	1.00316
5-10	1.00681	1.00444	1.00732	1.00505
10-15	1.01033	1.00662	1.00946	1.00647
15-20	1.01346	1.00796	1.01386	1.00801
20-25	1.01776	1.00947	1.01797	1.01035
25-30	1.02257	1.01315	1.02158	1.01289
30-35	1.02849	1.01837	1.03016	1.01623
35-40	1.03686	1.02038	1.03483	1.01831
40-45	1.0413	1.02662	1.04425	1.02532
45-50	1.06095	1.03682	1.05806	1.03451
50-55	1.07632	1.04951	1.07307	1.05092
55-60	1.10134	1.06809	1.11075	1.07476
60-65	1.155	1.12687	1.14263	1.11341
65-70	1.21862	1.21549	1.22186	1.19417
70-75	1.28699	1.30877	1.27693	1.26631
75-80	1.40652	1.43366	1.37951	1.34913
80-85	1.44185	1.55523	1.40746	1.43001
85-90	1.64051	1.66456	1.60201	1.57258

Table B.9: ξ values for each centrality bin in Au+Au for partner $1.3 < p_T 1.45 GeV/c$

Centrality	ξ			
	N_coll sat. exp	N_{part} sat. exp.	N_{coll} arctan	N_{part} arctan
Leading Mesons				
0-5	1.00274	1.00146	1.00246	1.00178
5-10	1.00456	1.00254	1.00434	1.00307
10-15	1.00702	1.00465	1.00696	1.00456
15-20	1.00972	1.00547	1.00988	1.00592
20-25	1.01352	1.00743	1.01373	1.00792
25-30	1.01789	1.01072	1.01829	1.01012
30-35	1.02355	1.01218	1.02394	1.01289
35-40	1.02873	1.01598	1.03074	1.01609
40-45	1.03922	1.02139	1.03883	1.02182
45-50	1.05125	1.02922	1.0498	1.02947
50-55	1.0691	1.04672	1.06527	1.04433
55-60	1.09431	1.06824	1.08926	1.06856
60-65	1.13138	1.1095	1.1246	1.10635
65-70	1.19999	1.18295	1.18707	1.17352
70-75	1.27198	1.27528	1.24761	1.25341
75-80	1.34518	1.35472	1.31457	1.33029
80-85	1.39898	1.412	1.36021	1.3849
85-90	1.52798	1.54927	1.48858	1.5094
Leading Baryons				
0-5	1.00419	1.00285	1.00401	1.00284
5-10	1.00673	1.00443	1.00645	1.00487
10-15	1.00972	1.00677	1.01002	1.00639
15-20	1.01337	1.00766	1.01343	1.00793
20-25	1.01723	1.01032	1.01814	1.0103
25-30	1.02174	1.01354	1.02277	1.01245
30-35	1.02863	1.01581	1.02869	1.01541
35-40	1.03574	1.01945	1.03619	1.01884
40-45	1.04568	1.02681	1.04414	1.02524
45-50	1.05845	1.03599	1.05751	1.03311
50-55	1.07735	1.05458	1.07545	1.04965
55-60	1.10667	1.08284	1.10018	1.07561
60-65	1.14918	1.12982	1.13816	1.11663
65-70	1.2232	1.21101	1.21149	1.19353
70-75	1.29622	1.30646	1.27912	1.27816
75-80	1.37906	1.40776	1.35239	1.36576
80-85	1.43914	1.47594	1.40562	1.42546
85-90	1.57869	1.65396	1.53251	1.56437

Table B.10: ξ values for each centrality bin in Au+Au for partner $1.2 < p_T 1.3 GeV/c$

Centrality	ξ			
	N_coll sat. exp	N_{part} sat. exp.	N_{coll} arctan	N_{part} arctan
Leading Mesons				
0-5	1.00276	1.00189	1.00241	1.00179
5-10	1.00524	1.00286	1.00424	1.0031
10-15	1.00767	1.00454	1.00695	1.00455
15-20	1.01063	1.0057	1.00991	1.00587
20-25	1.0141	1.00765	1.01343	1.00786
25-30	1.0186	1.01047	1.01793	1.00998
30-35	1.02337	1.01207	1.02373	1.01275
35-40	1.02922	1.01623	1.03194	1.01585
40-45	1.03799	1.02211	1.04174	1.02149
45-50	1.04668	1.02969	1.04792	1.02904
50-55	1.06363	1.04641	1.0646	1.04397
55-60	1.0936	1.07319	1.09096	1.06693
60-65	1.12624	1.10872	1.11133	1.10398
65-70	1.19722	1.18197	1.1784	1.17107
70-75	1.26024	1.2668	1.2383	1.24966
75-80	1.33468	1.34945	1.33286	1.32438
80-85	1.36902	1.40507	1.36817	1.38016
85-90	1.53924	1.51154	1.51548	1.50124
Leading Baryons				
0-5	1.00428	1.0028	1.00396	1.00302
5-10	1.00676	1.00371	1.00688	1.00502
10-15	1.01029	1.00591	1.00974	1.00652
15-20	1.01324	1.00703	1.01317	1.00786
20-25	1.01707	1.01139	1.01782	1.0099
25-30	1.02214	1.01207	1.02293	1.01285
30-35	1.02814	1.01671	1.02787	1.01509
35-40	1.03681	1.02018	1.03518	1.01832
40-45	1.04563	1.02715	1.04191	1.02461
45-50	1.05785	1.03287	1.05234	1.03226
50-55	1.07547	1.05851	1.06778	1.04654
55-60	1.10788	1.0804	1.09639	1.07321
60-65	1.14874	1.1295	1.14495	1.11836
65-70	1.22137	1.20834	1.20427	1.18726
70-75	1.30207	1.31143	1.24968	1.27785
75-80	1.37388	1.41653	1.34848	1.33743
80-85	1.47889	1.48709	1.39902	1.41828
85-90	1.57085	1.51632	1.56211	1.54936

Table B.11: ξ values for each centrality bin in Au+Au for partner $1.07 < p_T 1.2 GeV/c$

Centrality	ξ			
	N_coll sat. exp	N_{part} sat. exp.	N_{coll} arctan	N_{part} arctan
Leading Mesons				
0-5	1.0027	1.0019	1.00242	1.00181
5-10	1.00435	1.00335	1.00435	1.00306
10-15	1.00684	1.00441	1.00687	1.00448
15-20	1.00956	1.00527	1.00974	1.0058
20-25	1.01321	1.00715	1.01337	1.0077
25-30	1.01654	1.00968	1.01775	1.00984
30-35	1.02284	1.01241	1.02376	1.01255
35-40	1.02739	1.01551	1.03014	1.01564
40-45	1.03744	1.02099	1.03666	1.02124
45-50	1.04806	1.02866	1.04941	1.02853
50-55	1.0651	1.04411	1.0637	1.04308
55-60	1.09128	1.06853	1.08737	1.06596
60-65	1.12967	1.10918	1.11881	1.10309
65-70	1.19653	1.17882	1.18778	1.16914
70-75	1.26557	1.26509	1.24657	1.24611
75-80	1.33474	1.33978	1.31369	1.31908
80-85	1.37105	1.38775	1.38716	1.37241
85-90	1.54342	1.53293	1.47059	1.4931
Leading Baryons				
0-5	1.0044	1.00281	1.00371	1.00285
5-10	1.00678	1.00428	1.007	1.00463
10-15	1.01001	1.00604	1.01017	1.00656
15-20	1.01311	1.00786	1.01347	1.00765
20-25	1.01728	1.00958	1.01764	1.00914
25-30	1.02173	1.01215	1.02265	1.01182
30-35	1.02784	1.01378	1.02746	1.01321
35-40	1.03362	1.01966	1.03523	1.01714
40-45	1.04353	1.02601	1.04155	1.02601
45-50	1.05537	1.03672	1.05606	1.03074
50-55	1.0745	1.05475	1.07205	1.04732
55-60	1.10359	1.07842	1.09816	1.07099
60-65	1.14505	1.12271	1.12829	1.11044
65-70	1.21841	1.19576	1.19046	1.19986
70-75	1.29296	1.30583	1.26312	1.26558
75-80	1.37735	1.39789	1.3509	1.36711
80-85	1.41438	1.45699	1.38291	1.42758
85-90	1.58289	1.59005	1.51571	1.54003

Table B.12: ξ values for each centrality bin in Au+Au for partner $1.0 < p_T 1.07 GeV/c$

B.0.5 d+Au ξ Values

p_T	ξ trigger mesons N_{coll} arctan	N_{part} arctan	N_{coll} arctan	trigger baryons N_{part} arctan
1.0-1.07	1.65838	1.41941	1.77103	1.45569
1.07-1.2	1.65948	1.42242	1.77304	1.45708
1.2-1.3	1.66826	1.44147	1.78505	1.47969
1.3-1.45	1.68897	1.44137	1.81196	1.47778
1.45-1.7	1.71107	1.45789	1.83464	1.49828
1.7-2.5	1.738	1.477	1.875	1.517

Table B.13: ξ values for each p_T bin in dAu